GAIN IMPROVEMENT OF ER-DOPED AMPLIFIERS FOR THE FEEDBACK FILTERS

A Dissertation

by

XIAOMIN SONG

Submitted to the Office of Graduate Studies of
Texas A&M University
in partial fulfillment of the requirements for the degree of

DOCTOR OF PHILOSOPHY

December 2011

Major Subject: Electrical Engineering

GAIN IMPROVEMENT OF ER-DOPED AMPLIFIERS FOR THE FEEDBACK FILTERS

A Dissertation

by

XIAOMIN SONG

Submitted to the Office of Graduate Studies of
Texas A&M University
in partial fulfillment of the requirements for the degree of

DOCTOR OF PHILOSOPHY

Approved by:

Chair of Committee,	Christi K. Madsen
Committee Members,	Ohannes Eknoyan
	Kai Chang
	Jairo Sinova
Head of Department,	Costas N. Georghiades

December 2011

Major Subject: Electrical Engineering

ABSTRACT

Gain Improvement of Er-doped Amplifiers for the Feedback Filters.

(December 2011)

Xiaomin Song, B.S., Tsinghua University;

M.S., Tsinghua University

Chair of Advisory Committee: Dr. Christi K. Madsen

The combination of the arsenic trisulfide (As_2S_3) waveguide and titanium diffused lithium niobate (Ti:$LiNbO_3$) waveguide provide us compact and versatile means for transmitting and processing optical signals, which benefits from the high index contrast between these two materials and the electro-optical properties of Ti: $LiNbO_3$. Furthermore, waveguide gain is introduced through selective surface erbium (Er) doping which yields high quality loss-compensated or even amplifying waveguides without disturbing the excellent electrooptical, acoustooptical and nonlinear properties of the waveguide substrate $LiNbO_3$. The integration of these waveguides allows the development of a whole class of new waveguide devices of higher functionality and complexity.

As one kind of the hybrid waveguide devices, a new configuration consisting of an As_2S_3 channel waveguide on top of an Er doped titanium diffused x-cut lithium niobate waveguide has been investigated by simultaneous analytical expressions, numerical simulations, and experimentation. Both simulation and experimental results have shown that this structure can enhance the optical gain, as predicted by the analytical expressions. An

As_2S_3 channel waveguide has been fabricated on top of a conventional Er:Ti:$LiNbO_3$ waveguide, where the higher refractive index As_2S_3 waveguide is used to pull the optical mode towards the substrate surface where the higher Er concentration yields an improved propagation gain. The relationship between the gain and As_2S_3 layer thickness has been evaluated, and the optimal As_2S_3 thickness was found by simulation and experimentation. Side integration was applied to reduce the extra propagation loss caused by the titanium diffusion bump. The propagation gain (dB/cm) has been improved from 1.1 to 2 dB/cm.

Another hybrid device which combines the As_2S_3 and $LiNbO_3$ is to make an As_2S_3 racetrack ring resonator on top of an x-cut y-propagation Er:Ti:$LiNbO_3$ waveguide, which is the potential structure for integrated lossless all-path filter. The ring was side-coupled with the Ti:$LiNbO_3$ waveguide, and the optical gain was achieved when the 5mm long coupling region where it has been diffused with Er in advance pumped by a 144mW pump laser. The free spectral range (FSR) of the measured ring response for TM mode is 0.0587nm (7.33GHz) at 1550nm. The roundtrip loss are 4.4dB (2.60dB/cm) when pump on and 5.8dB (3.44dB/cm) when pump off. The optical gain in the Er diffused area is 0.72dB/cm.

DEDICATION

To my family

ACKNOWLEDGEMENTS

I would like to thank my advisor and committee chair, Dr. Christi K. Madsen, for her expert guidance, encouragement and constant support during my dissertation work. I am also grateful to other committee members, Dr. Ohannes Eknoyan, Kai Chang, Jairo Sinova, for their time and effort in guiding and supporting me throughout the course of this research.

I appreciate very much the help and discussions from my friends and colleagues. They are Mehmet Solmaz, Renato Rabelo, Yongwook Shin, Donnie Adams, Alex (Xin) Xia, Weechong Tan, Jaewoo Suh, W. Tim Snider, Jacob Webb, Wonju Sung, Yifeng Zhou, Qi Chen, Jae Kim, Xin Wang and Dwayne Denton. Besides, I am grateful to the ISSE staff, Robert Atkins, Jim Gardner, Travis James and George Flores for their support and help.

Finally, I would like to thank my beloved wife Emma, my parents and my sister for their unconditional love and support.

TABLE OF CONTENTS

Page

CHAPTER Page

LIST OF FIGURES

FIGURE Page

FIGURE Page

FIGURE Page

FIGURE Page

FIGURE Page

LIST OF TABLES

TABLE Page

CHAPTER I

INTRODUCTION

1.1. Background and motivation

1.1.1. Background

The field of integrated optics has a significant development during the last two decades along with the explosive growth of the fiber telecommunication systems. These developments require a correspondingly large number of optical components no matter passive devices such as splitters, couplers, multiplexers, switches, filters, modulators etc, or active components like optical sources, detectors, and optical amplifiers. Most of these components have been realized in integrated-optic form.

The integrated active feedback filters possess intrinsic merits which are pursued by the researchers in the area of integrated optics: smaller size, lower cost, more powerful functionality and design flexibility. Resonators based reconfigurable optical devices with feedback paths including rings and Gires-Tournois interferometers (cavities) are attractive since they can work as switches, modulators, multiplexers and filters as well.

Among these applications based on resonators, the lossless all-pass filter (APF) can be one of the hotspots in this area. Such filters can generate large group delay and dispersion without any amplitude distortion, and have been used in tunable dispersion

---

This dissertation follows the style of *Journal of Lightwave Technology*.

compensation [1-4], dispersion slope compensation [5], optical delay lines [6] and as building blocks in tunable band-pass filters where multiple stages of all-pass filters are cascaded or latticed.

To achieve the “loss-less” capability which contradicts to the inherent characteristic of loss for every media, the optical gain is required to be introduced through the feedback path.

This work concentrates on the gain improvement of the amplifiers for compensating the loss throughout the feedback path in the all-pass filters which serve as the basic building block for integrated optical signal processing. The increase of the gain can be realized by several improvements on waveguide design, fabrication technique and equipment enhancement. The detailed inspected parameters include: material chosen, waveguide dimensions design (thickness, width and length), index profile, mode overlap calculation, gain modeling, coupling tip shape, photolithography recipe, etc. They will be discussed all through this dissertation.

1.1.2. Materials

This section will introduce three major materials used in the research. The integrated optical devices discussed above are fabricated by these materials.

As_2S_3 (Fig. 1) is one kind of amorphous chalcogenide glass which is a chemical compound consisting of at least one chalcogen ion and at least one more electropositive element. Although all group 16 elements of the periodic table are defined as chalcogens, the term is more commonly reserved for sulfides, selenides, and tellurides, rather than

oxides. As_2S_3 has very good optical properties. It is transparent between 620 nm and 11 μm with large refractive index around 2.4. And it also has large nonlinearity [7].

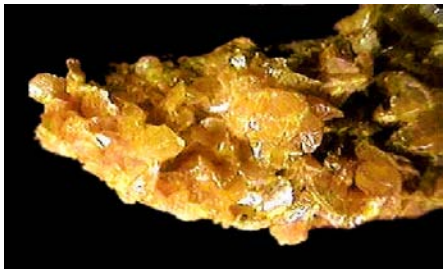

Fig. 1. As_2S_3 [8].

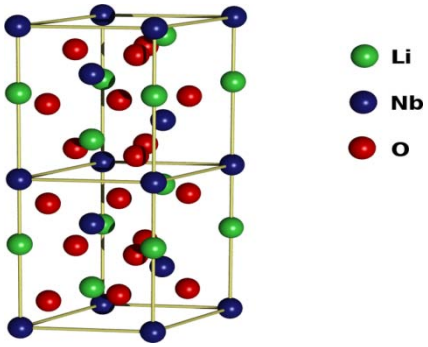

Fig. 2. Lithium niobate crystal structure [9].

Lithium niobate ($LiNbO_3$ or LN) is a birefringent crystal (Fig. 2) that has long been utilized as the substrate material for its strong tuning capability. It is a compound of niobium, lithium, and oxygen and its single crystals are an important material for optical waveguides, mobile phones, optical modulators and various other linear and non-linear optical applications [9].

$LiNbO_3$ has wide transmission range: 420 nm~5.2 μm. It has excellent electric-optical and non-linear properties. The $LiNbO_3$ wafers that have been used in the research work are x-cut, y-propagation, two inches in diameter and 1or 0.5mm thick.

Titanium diffused waveguides in lithium niobate substrate (Ti: $LiNbO_3$), as being well developed for thirty years, has excellent electro-optical properties, low propagation loss and low coupling loss to optical fiber [10, 11] which has been used as the foundation of our devices.

Erbium is a rare earth element in the lanthanide series, with the symbol Er and atomic number 68. It is a silvery-white solid metal when artificially isolated. Natural erbium is always found in chemical combination with other elements on Earth. Erbium's principal uses involve its pink-colored Er^{3+} ions, which have optical fluorescent properties particularly useful in certain laser applications [12]. Erbium-doped glasses or crystals can be used as optical amplification media, where Er^{3+} ions are optically pumped at around 980 nm or 1480 nm and then radiate light at 1530 nm in stimulated emission. This process results in an unusually mechanically simple laser optical amplifier for fiberoptically transmitted signals. The 1550 nm wavelength is especially important for optical communications because standard single mode optical fibers have minimal loss at this particular wavelength. The most common example is the Erbium Doped Fiber Amplifier (EDFA) (Fig. 3 from internet), where the core of a silica fiber is doped with trivalent Erbiumions and can be efficiently pumped with a laser at a wavelength of 980 nm or 1,480 nm, and exhibits gain in the 1,550 nm regions.

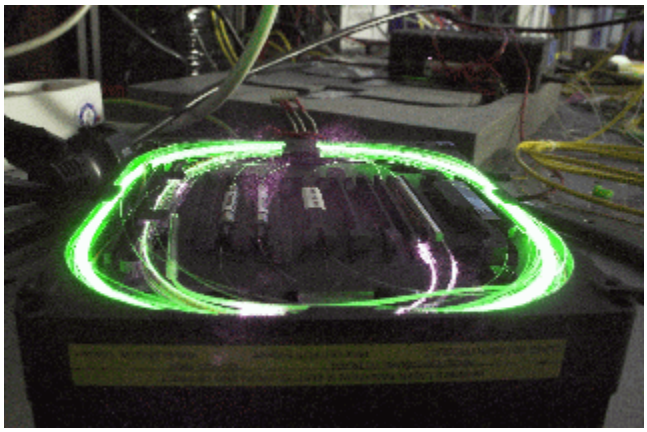

Fig. 3. Erbium Doped Fiber Amplifier (EDFA).

Erbium (Er) diffused titanium diffused lithium niobate (Ti:LiNbO3) waveguides have also been extensively investigated [13]. Positive gain has been achieved to overcome the propagation loss and even high enough to make lasers [14-16].

1.2. Previous work

The combination of the As_2S_3 waveguide and Ti:$LiNbO_3$ waveguide provide us compact and versatile approaches for transmitting and processing optical signals, which benefits from the high index contrast between these two materials and the electro-optical properties of Ti: $LiNbO_3$. Furthermore, waveguide gain can be introduced through selective surface erbium doping which yields high quality loss-compensated or even amplifying waveguides without disturbing the excellent electrooptical, acoustooptical and nonlinear properties of the waveguide substrate $LiNbO_3$. The integration of these waveguides allows the development of a whole class of new waveguide devices of higher functionality and complexity.

1.2.1. As_2S_3 assisted Er: Ti: $LiNbO_3$

Erbium doped Ti:$LiNbO_3$ waveguides have been widely explored [13]. The overlap between the optical fields and Er ions has been related to the optical gain [15] which has been achieved to overcome the propagation loss and even high enough to make lasers [14-16]. It is well-known that the propagation gain is proportional to the overlap between the optical mode and Er profile.

For the surface in-diffused Er profile, achieving a high overlap requires pulling the optical mode closer to the surface, where the Er concentration is higher. To achieve the mode pulling, a blanket-clad TiO_2 configuration has been reported with estimates on the gain improvement [17]. Arsenic trisulfide is a better choice for mode pulling owing to its high refractive index. Other benefits include a high nonlinear coefficient, low propagation loss, and low processing temperature. In this paper, we focus on the gain improvement by using a patterned As_2S_3 waveguide on top of a straight Er:Ti:LiNbO3 to elevate the mode. Utilizing a straight channel As_2S_3 waveguide instead of a blanket film not only improves the gain, but also reduces the propagation loss by side coupling. We have found that surface roughness from the Ti diffused bump will introduce excess losses if the As_2S_3 waveguide sits on top of the diffused waveguide. Hence, the As_2S_3 layer is patterned next to the titanium bump to utilize side coupling and avoid the losses associated with the non-planar bump surface. Furthermore, the patterned As_2S_3 waveguide enables vertically integrated structures, which combines the As_2S_3 waveguide above the substrate surface and the Er:Ti:LiNbO3 waveguide below the surface, such as Mach Zehnder Interferometers (MZI) and rings [18, 19].

We also investigated the range of As_2S_3 thicknesses that enhance the optical gain, and found the optimum As_2S_3 waveguide parameters through simulations and confirmed in experimentation.

1.2.2. As_2S_3 ring and cavity on Er: Ti: $LiNbO_3$

The integrated resonator based reconfigurable optical devices with feedback paths are attracting interests recently. They have various applications such as modulators [20], optical filters and multiplexers [21].

All-pass filters (APF's) are resonant devices that allow any desired phase correction or equalization without introducing any amplitude distortion [2], which means it can produce strong on-resonance phase variation while maintaining unity reflectance or transmission. The structural losslessness property induces its robust performance [22].

As the computationally efficient signal processing building blocks which are quite useful in many signal processing applications [22], such filters can generate large group delay and dispersion, and have been used in tunable dispersion compensation [1-4], dispersion slope compensation [5], optical delay lines [6] and as building blocks in tunable band pass filters where multiple stages of all-pass filters are cascaded or latticed. Furthermore, in contrast to other dispersion compensation devices, optical APF's can correct any order of dispersion [2].

Optical all-pass filters have been implemented using side-coupled ring resonators [23], optical thin-film filters [24], or Gires-Tournois interferometers [4, 6]. Recent

research has shown that As_2S_3 rings can be coupled with Ti:$LiNbO_3$ waveguides to implement filtering functions by top coupling [18] and side coupling [19].

As hybrid devices which combines the As_2S_3 and $LiNbO_3$, their ring structures can be improved by doping Er in the coupling region and pumped by 1480nm laser to bring optical gain to compensate the round trip propagation losses which makes the rings lossless and have further potential applications.

1.3. Organization of the dissertation

After the background introduction of Chapter I, Chapter II gives the theoretical knowledge used in the following chapters. The electromagnetic theory and three numerical solvers have been reviewed first. Then the modeling of the optical waveguides, the feed-back resonator theory, electro-optical effect, the multilayer and Bragg grating reflectors have been introduced respectively.

In Chapter III, the simulations of the optical devices have been discussed. These devices include: titanium diffused waveguides; As_2S_3 assisted Er:Ti:$LiNbO_3$ waveguides; As_2S_3 rings on top of the Ti: $LiNbO_3$ waveguides; electrical optical devices; multilayer and Bragg reflectors. The results of simulations guide us on the device structure design and fabrication parameter settings.

In Chapter IV, the fabrication processes of three optical devices are introduced: As_2S_3 waveguide assisted Er:Ti:$LiNbO_3$, As_2S_3 ring on Er:Ti:$LiNbO_3$ and Er:Ti:$LiNbO_3$ cavity. Several experimental skills and recipes are discussed.

In Chapter V, the experimental results on fabricated waveguides in Chapter IV have been presented. Details of the measurement setup are revealed. Then in Chapter V, the dissertation is concluded and the prospect of the future work.

CHAPTER II

THEORETICAL REVIEW

2.1. Electromagnetic theory and waveguide mode solving

2.1.1. Electromagnetic theory

Classical electrodynamics theory can describe the electromagnetic phenomena accurately when quantum and relativistic effects are negligible. The properties of the optical wave or any other electromagnetic waves, including their excitation, propagation and interaction with media are governed by Maxwell's equations. Maxwell's equations in differential form are shown in equation to (2.1)~(2.4) [25].

$$\nabla \cdot \boldsymbol{D} = \rho \tag{2.1}$$

$$\nabla \cdot \boldsymbol{B} = 0 \tag{2.2}$$

$$\nabla \times \boldsymbol{E} = -\frac{\partial \boldsymbol{B}}{\partial t} \tag{2.3}$$

$$\nabla \times \boldsymbol{H} = \boldsymbol{J} + \frac{\partial \boldsymbol{D}}{\partial t} \tag{2.4}$$

where $\boldsymbol{D}$ is the electric displacement (or electric flux density) vector, $\boldsymbol{B}$ is magnetic flux density (or magnetic displacement) vector. $\boldsymbol{E}$ and $\boldsymbol{H}$ are the electric and magnetic field vectors. ρ is the total free charge density. $\boldsymbol{J}$ is the total current density vector**.**

The equations (2.1) and (2.2) are Gauss's law for electrics and Gauss's law for magnetism. They describe the normal components of the fields emanate from charges. Equations (2.3) and (2.4), which are the Faraday's Law and Ampere's Law, describe how the tangential components of the fields emanate from the flux changes.

The constitutive relations that represent the interactions between the electric, magnetic fields and the media are in (2.5) and (2.6):

$$\boldsymbol{D} = \varepsilon_0 \boldsymbol{E} + \boldsymbol{P} = \varepsilon_0 \varepsilon_r \boldsymbol{E} = \varepsilon \boldsymbol{E} \tag{2.5}$$

$$\boldsymbol{B} = \mu_0 (\boldsymbol{H} + \boldsymbol{M}) = \mu_0 \mu_r \boldsymbol{H} = \mu \boldsymbol{H} \tag{2.6}$$

where ε_0 is the permittivity and μ_0 is the permeability of free space. ε is permittivity and μ is the permeability in the media. $\boldsymbol{P}$ and $\boldsymbol{M}$ are polarization and magnetization respectively. When the medium is anisotropic, ε_{r} becomes a tensor. If the coordinate system matches the orientation of the crystal principal axes,

$$\boldsymbol{D} = \varepsilon_0 \varepsilon_r \boldsymbol{E} = \varepsilon_0 \begin{bmatrix} \varepsilon_{r11} & & \\ & \varepsilon_{r22} & \\ & & \varepsilon_{r33} \end{bmatrix} \boldsymbol{E} \tag{2.7}$$

The propagation speed of the light in the medium is characterized by the refractive index n and the relative permittivity ε_r (μ_{r} is usually equals to 1).

$$n = \frac{c}{v} = \frac{\sqrt{\varepsilon\mu}}{\sqrt{\varepsilon_0 \mu_0}} = \sqrt{\varepsilon_r} \tag{2.8}$$

There is Ohm's law in conductive materials:

$$\boldsymbol{J} = \sigma \boldsymbol{E} \tag{2.9}$$

In vacuum or isotropic medium, where no free charges and no conductive currents exist, those equations will lead the Wave Equations.

Take the curl of (2.3), and use the vector identity $\nabla \times \nabla \times \boldsymbol{E} = \nabla(\nabla \cdot \boldsymbol{E}) - \nabla^2 \boldsymbol{E}$. Bring in (2.2) which yield $\nabla \cdot \boldsymbol{E} = \boldsymbol{0}$ then we have

$$-\nabla^2 \boldsymbol{E} = -\mu \frac{\partial}{\partial t} (\nabla \times \boldsymbol{H}) \tag{2.10}$$

Use (2.4) to substitute the $\nabla \times \boldsymbol{H}$ part above and we have

$$\nabla^2 \boldsymbol{E} - \frac{\varepsilon_r \mu_r}{c^2} \frac{\partial^2 \boldsymbol{E}}{\partial t^2} = 0 \tag{2.11}$$

where c is the speed of light in vacuum,

$$c = \frac{1}{\sqrt{\varepsilon_0 \mu_0}} = 2.99794 \times 10^8 \ m/s \tag{2.12}$$

Follow the simimar process, we can get

$$\nabla^2 \boldsymbol{H} - \frac{\varepsilon_r \mu_r}{c^2} \frac{\partial^2 \boldsymbol{H}}{\partial t^2} = 0 \tag{2.13}$$

The solutions of these wave equations (2.11) and (2.13) are all kinds of wave expressions. The planar wave is the widely used:

$$\boldsymbol{E} = \boldsymbol{A} \exp[i(\boldsymbol{k} \cdot \boldsymbol{r} - \omega t)] \tag{2.14}$$

where k is the wave number:

$$k = \frac{2\pi}{\lambda} \tag{2.15}$$

When light propagation from one medium to another, the boundary conditions must to be considered:

$$\begin{cases} n \cdot (\boldsymbol{D}_1 - \boldsymbol{D}_2) = 0 \\ n \cdot (\boldsymbol{B}_1 - \boldsymbol{B}_2) = 0 \\ n \times (\boldsymbol{E}_1 - \boldsymbol{E}_2) = 0 \\ n \times (\boldsymbol{H}_1 - \boldsymbol{H}_2) = 0 \end{cases} \tag{2.16}$$

They are directly derived from the integrated form of (2.1) ~ (2.4) by integration around the infinite small volume or area across the interface. Using the boundary conditions, the equations for refraction and reflection can be derived.

In Fig. 4, $\boldsymbol{E} = \boldsymbol{A}\exp[i(\boldsymbol{k}\cdot\boldsymbol{r} - \omega t)]$ is the incident wave, $\boldsymbol{E} = \boldsymbol{A}\exp[i(\boldsymbol{k}\cdot\boldsymbol{r} - \omega t)]$ is the reflected wave and $\boldsymbol{E} = \boldsymbol{A}\exp[i(\boldsymbol{k}\cdot\boldsymbol{r} - \omega t)]$ is the refracted wave.

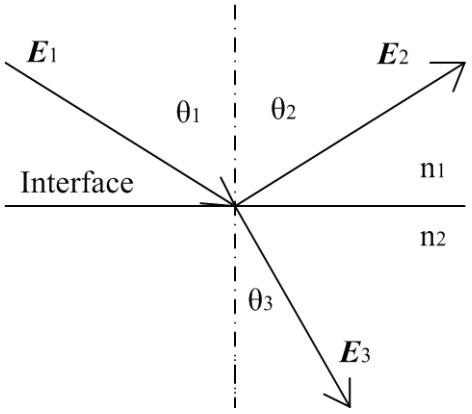

Fig. 4. Reflection and refraction.

By using the boundary condition $n\cdot(\boldsymbol{D}_1 - \boldsymbol{D}_2) = 0$, the following equations can be obtained:

$$\boldsymbol{k}_1\cdot\boldsymbol{r} = \boldsymbol{k}_2\cdot\boldsymbol{r} = \boldsymbol{k}_3\cdot\boldsymbol{r} \tag{2.17}$$

Considering the direction of $\boldsymbol{r}$ is normal to the interface, (2.17) can be transformed:

$$\theta_1 = \theta_2 \tag{2.18}$$

$$n_1\sin(\theta_1) = n_2\sin(\theta_3) \tag{2.19}$$

The reflected light has the same angle as incident light in (2.18), and the refracted light follows Snell's Law in (2.19).

From (2.19), if the light incident from higher index medium to the lower index medium ($n_1 > n_2$) and θ_1 is large enough ($\theta_1 > \theta_c = \sin^{-1}(\frac{n_2}{n_1})$, θ_c is called critical angle), θ_3 could be a complex number which means the light cannot enter medium two. It is called total internal reflection (Fig. 5) and it is the principle of light confinement properties of the dielectric waveguides.

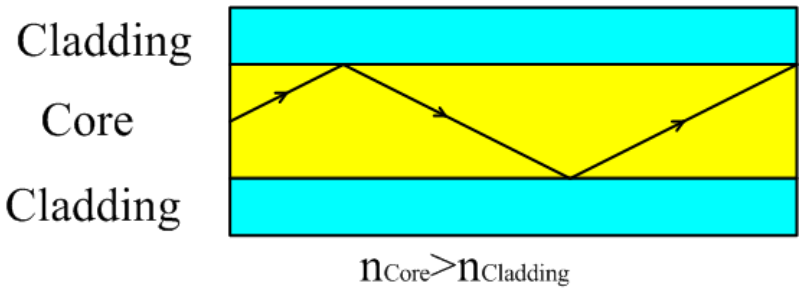

Fig. 5. Total internal reflection.

Integrated waveguides, serving as an optical interconnection, guide light by total internal reflection.

2.1.2. Numerical solvers

A comprehensively and accurately understanding of the characteristics of the propagating light inside the waveguides requires both analytical expressions and numerical simulations. The analytical expressions have been intensively investigated. The 2D waveguide which is composed of a higher index layer sandwiched by two low

index cladding layers has the analytical equations which can calculate the eigenvalue and then the effective index. The calculations for 3D waveguide calculation can be more difficult since the cross sections of them are more complicated. The major methods are Marcatilis's method for strong guided (high index contrast) rectangular waveguides such as channel waveguides and effective index method for weak guided such as diffused waveguides.

However, for waveguides with irregular cross sections or variational cross sections along the direction of propagation, these analytical expressions are helpless. Then the numerical solvers became attractive and powerful.

The numerical methods digitalize the index profile and mode profile on the cross section of the waveguide by dividing the whole waveguide into mesh grid points. All the data such as refractive index or amplitude densities are represented by the values on these discrete points. Then the solvers evolve the Maxwell's difference equation to difference equations based on their own simplification and assumptions. With the boundary conditions and initial conditions, the engenvalues or the effective index can be "guess out" by specific convergent algorithms. Not only the engenvalues, but also the mode profiles, beam widths, the dispersions, the confinement factors, etc. All the optical information about the waveguides can be calculated. The accuracy depends on the resolution of the mesh points. However, more points bring more calculation time. So the accuracy and calculation time can be a trade-off although several skills have been brought into the convergent algorithms to speed up the calculation.

Also, the numerical solvers can simulate the beam propagation through varying waveguides which makes them capable of simulating “two by two” coupler, Mach-Zehnder Interferometer, etc. Moreover, with add-in Electro-optic parameters, they can simulate the EO modulator. The Film Mode Matching (FMM) solver [26], Finite Different Mode (FDM) solver [27] and Finite Element method (FEM) solver are The most useful solvers.

2.2. Optical waveguides modeling

2.2.1. Modeling of the Ti: $LiNbO_3$

The simulation by computer software with numerical methods is becoming more and more powerful. Before setting up the simulation work chapter III, the modeling of the titanium diffused waveguides is discussed here. The lithium niobate substrate discussed in this chapter is x-cut, y-propagation.

The diffusion model includes two groups of parameters: diffusion coefficients and index change coefficients. The diffusion coefficients describe how deep the dopants can diffuse through the substrate in a specific time period. And the index change coefficients describe how large the index will change (usually increase) from to the concentration of the dopant.

The overall index is the sum of the bulk index n_o or n_e and the diffusion induced change index change Δn_i [28],

$$n_i(\lambda, x, y) = n_i(\lambda) + \Delta n_i(\lambda, x, y) \qquad i = o, e \tag{2.20}$$

The ordinary and extraordinary bulk indices (at $25^{\circ}C$) of congruent lithium niobate can be expressed by Sellmeier's dispersion equations (λ in μm)

$$n_o^2 = 4.9048 - \frac{0.11768}{0.0475 - \lambda^2} - 0.027169\lambda^2 \tag{2.21}$$

$$n_e^2 = 4.582 - \frac{0.099169}{0.044432 - \lambda^2} - 0.02195\lambda^2 \tag{2.22}$$

(2.21)and (2.22) originate from [29], and the parameters were updated in [30]. (2.21) and (2.22) give us: $n_o = 2.2112$, $n_e = 2.1381$ at λ=1550nm. Compare to more precise n_e from [31]: $n_e = 2.137880$.

The Relative error is (2.138064-2.137880)/2.137880*100%=0.0086% which can be neglected.

Then we can discuss the diffusion induced index change: Δn_i. The Δn_i comes from the in-diffused Ti^{4+}. The diffusion process must be done in wet O_2 or wet air ambient to suppress out-diffusion of Li_2O which will induce another Δn_e. Otherwise this additional Δn_e throughout the lithium niobate surface will make strip waveguide lose its light confinement in the direction perpendicular to the waveguide and more like be a planer waveguide and induce high order-TE mode [10].

From [28],

$$\Delta n_i(\lambda, x, y) = d_i(\lambda) h_i(x, y), \qquad i = o, e \tag{2.23}$$

$d_i(\lambda)$ is called dispersion factor and it describes the wavelength dependence.

$$d_o(\lambda) = \frac{0.67\lambda^2}{\lambda^2 - 0.13}, \quad d_e(\lambda) = \frac{0.839\lambda^2}{\lambda^2 - 0.0645} \tag{2.24}$$

$h_i(x, y)$ is Ti^{4+} concentration dependent function.

$$h_i(x, y) = [F_i c(x, y)]^{\gamma_i} \qquad i = o, e \tag{2.25}$$

where the distribution constants are $F_0 = 1.3\times10^{-25}\text{cm}^3$, $F_e = 1.2\times10^{-23}\text{cm}^3$. And the distribution power factors are $\gamma_o = 0.55$, $\gamma_e = 1.00$.

For titanium diffused waveguide, the typical diffusion temperature is at 1025 ℃, the titanium thickness is around 100 nm and the diffusion time is around 10 hours. The waveguide formed by this process can guide mode which matches best to the fiber mode and result in lowest coupling loss. From [32], $\Delta n_e \approx 0.015, \Delta n_o \approx 0.007$.

Now we have the relation between Ti^{4+} concentration and the index change, and still we need to know the Ti^{4+} concentration.

The diffused Ti^{4+} concentration Profile was created by two-steps high temperature diffusion process: predepositon and drive-in.

(a) Pre-deposition (t< t_e):

The depletion time t_e is the time when titanium strip totally diffuses into the substrate. From [33]:

$$t_e = \left(\frac{\rho N_A}{M_{rel}} \frac{\tau}{2c_0} \right)^2 \frac{\pi}{D_v} \tag{2.26}$$

where ρ is the density, N_A the Avogadro's numer, τ the initial Ti thickness and M_{rel} the relative mass of the Ti. D_v is the vertical diffusion coefficient. By choosing the values below, the titanium depletion time can be calculated in Table I. The normal titanium waveguide diffusion time is about two times larger than the depletion time. So

they are in the drive-in region. The values are listed: $\rho = 4.5g/cm^3$, $N_A = 6.022e23\ mol^{-1}$, $M_{rel} = 47.9$, $Dv = 1.45e^{-12}cm^2/s\ (at\ 1025^\circ C)$, $C_0 = 3.0e21\ cm^{-3}$

Table I. Titanium depletion time.

Ti Thickness(A)	600	700	800	900	1000	1100	1200	1300	1400	1500
Depletion Time(hr)	1.9	2.6	3.4	4.4	5.37	6.5	7.73	9.08	10.5	12.1

In the time regime of predeposition, the surface concentration is a constant limited by the solubility of Ti^{4+} in LiNbO3 (c_s =5.67e22 cm^-3), the profile is an error function [34].

TM mode will have great loss in this time range. So our diffusion time is usually longer than t_e to make the TM mode loss lower.

(b) Drive-in: (t> t_e)

In this part, all the Ti^{4+} ions have been diffused into the surface and the total amount of Ti4+ is a constant. The profile becomes a Gaussian function with a decreasing surface concentration.

TE, TM modes will have closer loss in this regime.

Although the relation between the technological procedure and the waveguide characteristics has not yet been established in a conclusive manner, the analytical expression (2.27) which separate x and y dependences has been widely accepted [28].

$$c(x,y) = c_0 f(y) g(x) \tag{2.27}$$

where

$$c_0 = c_m \tau / (\sqrt{\pi} D_v), c_m = (\rho / M_{atom}) N_A \tag{2.28}$$

$$f(y) = \exp(-\frac{y^2}{D_b^2}) \tag{2.29}$$

$$g(x) = \frac{erf[\frac{w}{2D_h}(1+\frac{2x}{w})] + erf[\frac{w}{2D_h}(1-\frac{2x}{w})]}{2} \tag{2.30}$$

where w and τ are the titanium strip width and thickness before diffusion. ρ is the bulk density of titanium, G is the atomic weight of titanium. D_v is vertical length and D_h the horizontal diffusion length.

The Arhenius relation from [33],

$$D_v = 2\sqrt{tD_v^0 exp(-E_v^0 / kT)} \tag{2.31}$$

$$D_h = 2\sqrt{tD_h^0 exp(-E_h^0 / kT)} \tag{2.32}$$

where t is the diffusion time, D_h^0 and D_v^0 are the horizontal and vertical diffusivities. E_v^0 and E_h^0 are the temperature dependence parameters (activation energy).k is the Boltzmann constant, and T is the temperature.

Some papers define $-E_{0b}/kT$ as $-T_0/T$. A lot of papers give their experimental data. [11] gives the diffusion values close to our experimental data at T=1025$^\circ C$:

After comparison with experiment results in Chapter III, the three basic parameters have been fitted:

$$\begin{cases} D_v^0 = 0.0199 cm^2/s, (Diffusivity\ on\ Ordinary\ axis) \\ D_h^0 = 0.0289 \times 10^{-12} cm^2/s,\ (Diffusivity\ on\ Extraordinary\ axis) \\ T_o = T_e = 3.03 \times 10^4 K \end{cases} \quad (2.33)$$

Also, $d_e(\lambda)$ and $d_o(\lambda)$ in (2.24) have been inserted in correction factors: 1.7 and 1.49 respectively.

$$d_e(\lambda) = \frac{0.839\lambda^2}{\lambda^2 - 0.0645} \times 1.7\,, d_o(\lambda = \frac{0.67\lambda^2}{\lambda^2 - 0.13} \times 1.49 \quad (2.34)$$

The parameters in (2.33) were fitted from the comparison between measured and simulated mode width data in section 3.1.1. The calculation can be performed by Matlab and the code is in APPENDIX A.

(c) Intermediate,($t \approx t_e$),

The diffusion profile is in a state between error function and Gaussian function. And the surface concentration is getting lower than solubility. But it is not the value as c_0 from (3.9).This still needs future discussion.

After discussing the model of titanium diffused waveguides, the simulation can be performed in Chapter III.

2.2.2. Modeling of the Er diffusion in $LiNbO_3$

The erbium diffusion in LiNbO3 is treated as planar in-diffusion.

$$c(y) = \hat{C}_0 \exp(\frac{-y^2}{4Dt}) \quad (2.35)$$

$$\hat{C}_0 = \tau C_0 / \sqrt{\pi Dt} \quad (2.36)$$

$\hat{C}_0$ is the surface concentration. D is the diffusion coefficient and t is the diffusion time. The Er profile is described by (2.35), only if the diffusion time larger than depletion time [35].

$$t_d = \left(\frac{\rho N_A}{M_{rel}} \frac{\tau}{2c_0} \right)^2 \frac{\pi}{Dv} \tag{2.37}$$

where ρ is the density, N_A the Avogadro's numer, M_{rel} the relative mass of the Er and τ the initial Er thickness. Dv is the vertical diffusion coefficient. The values are: $\rho = 9.066 g/cm^3$, $N_A = 6.022e23\ mol^{-1}$, $M_{rel} = 167.259 g/mol$ $Dv = 0.025 um^2/h = 2.5\times10^{-10} cm^2/h$ $(at\ 1100^\circ C)$ [35]. The values of C_0 are not consistent. In [35], figure number 4 gives $C_0^1 = 2e20\ cm^{-3}$ but figure number 2 gives $C_0^2 = 4e20\ cm^{-3}$.

Table II. Er depletion time: (1) is from C_0^1, (2) is from C_0^2.

Er Thickness(nm)	10	11	15	19	21	23	25
Depletion Time(hr)(1)	83.6	101	188	302	369	442	523
Depletion Time(hr)(2)	20.9	25.3	47.1	75.5	92	111	131

In the Table II, (2) is more close to the experiment in our laboratory.

The Er diffusion time should be larger than the depletion time to let the Er totally diffuse into the LN crystal.

The conversion between mol% to cm^{-3} is shown below. For example, 0.5 mol% of Er in LN was converted to density of Er in LN. The molar weight of Er and $LiNbO_3$ are $167.259 g/mol$ and 147.846 g/mol. Density of $LiNbO_3$ is 4.65 g/cm^3, then the density of Er in $LiNbO_3$ is $\frac{4.65}{147.846} \times 0.5\% \times N_A = 9.47 \times 10^{19} cm^{-3}$.

2.2.3. Modeling of the Er gain

The gain of the amplifier is a function of the overlap between the Er profile and optical mode. In the two-level model, the steady state propagation equation describing the signal power evolution in the optical amplifier is given by [36, 37],

$$\partial P_S(z)/\partial z = (\gamma_{21} - \gamma_{12}) P_S(z) - \alpha P_S(z) \tag{2.38}$$

$$\gamma_{21} = N_2(z) \iint_A \Psi_s(x,y) \sigma_s^e \rho Er(x,y) dxdy \tag{2.39}$$

$$\gamma_{12} = N_1(z) \iint_A \Psi_s(x,y) \sigma_s^a \rho Er(x,y) dxdy \tag{2.40}$$

$$\iint_A \Psi_s(x,y) dxdy = 1 \tag{2.41}$$

where P_s is the signal power, Ψ_s is the normalized mode distribution as shown in (2.41). γ_{21} and γ_{12} are expressed by (2.39) and (2.40). ρ is the density of Er atoms at the $LiNbO_3$ surface, $Er(x,y)$ is the normalized diffused Er profile, where the maximum of $Er(x,y) = 1$. σ_s^e and σ_s^a are the cross sections for stimulated emission and absorption at signal wavelength. $N_2(z)$ and $N_1(z)$ are the fraction of atoms per unit length in the excited state and ground state ($N_2(z) + N_1(z) = 1$, [37]) which are determined by the pump efficiency.

Here the amplified spontaneous emission (ASE) noise is ignored since the gain is small. We assumed that the pump power is high enough (>20dBm) to maximize the population inversion of the Er atoms so that the gain is uniform along the waveguide. Substituting (2.39)~(2.41) into (2.38) becomes:

$$\partial P_s(z)/\partial z / P_s(z) = \rho\Gamma[(\sigma_s^e + \sigma_s^a)N_2(z) - \sigma_s^a] - \alpha_s \tag{2.42}$$

$$\Gamma = \iint_A \Psi_s(x,y)Er(x,y)dxdy \tag{2.43}$$

where Γ expressed by (2.43) is the overlap between the normalized signal mode Ψ_s and the Er profile $Er(x,y)$, and α_s is the propagation loss.

The optical gain (dB per unit length) can be expressed by inserting the conversion factor $10\log(e)$ into (2.42) [37]. The propagation gain (gain per unit length) is defined as the gain relative to the non Er doped waveguide, which has loss α_s, as follows:

$$Gain(dB/l) = 10\log(e)\rho\Gamma[(\sigma_s^e + \sigma_s^a)N_2(z) - \sigma_s^a] \tag{2.44}$$

So the propagation gain is proportional to the overlap between the signal mode and Er profile.

2.3. Ring resonator theory

My research is focus on the gain improvement in the loop of the feedback filter. Our group already made device shown in Fig. 6(a) by integrating As_2S_3 ring on top of the Ti:$LiNbO_3$ [18, 19]. Measured amplitude is shown in Fig. 6(b).

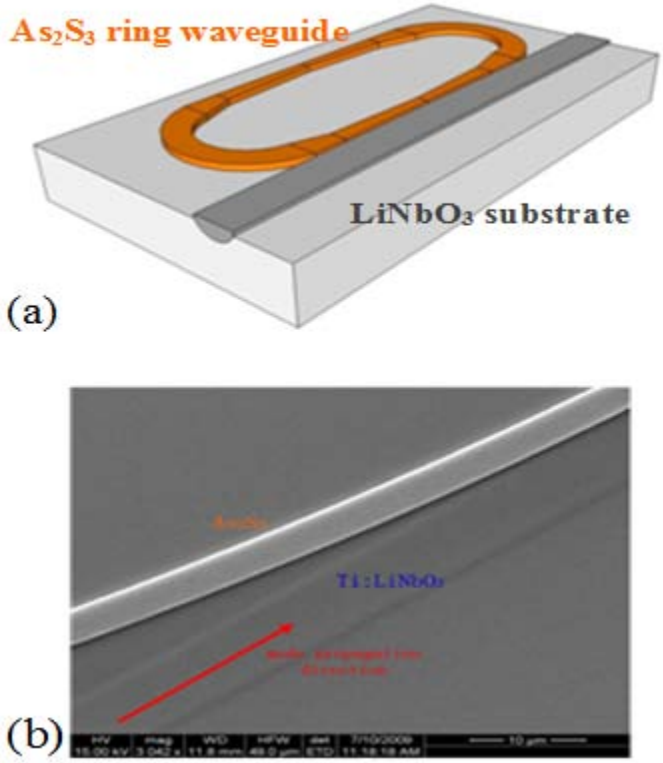

Fig. 6. As_2S_3 ring side coupled to Ti:$LiNbO_3$ waveguide: (a) Schematic structure; (b) SEM image of the fabricated ring device: side-coupling region.

The ring structure can be modeled by a simple 2by2 coupler and 1feed back loop in Fig. 7. The through port has coupling ratio $\rho = \sqrt{1-k}$ and the cross port has coupling ratio $-j\sqrt{k}$. The feedback loop's delay e^{-jwt} can be expressed by z^{-1} as the unit delay time. And the round trip loss is expressed by γ. So the whole system can be analysis by z-transform. The output of the ring can be expressed by $Y(z) = [\rho - k\gamma^{-1}z^{-1} - \rho k\gamma^{-2}z^{-2} - ...]X(z)$.

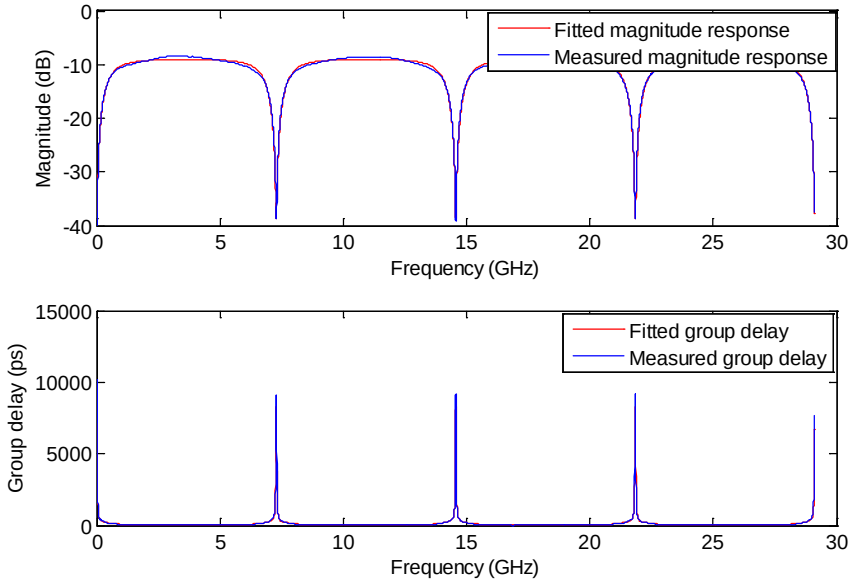

Fig. 7. Transmission and group delay response of the ring structure.

So the transfer function $H(z)=\dfrac{\rho-\gamma z^{-1}}{1-\rho z^{-1}}$.The amplitude is $20\log\left|\dfrac{\rho-\gamma z^{-1}}{1-\rho z^{-1}}\right|$ and the phase is $\arg(\dfrac{\rho-\gamma z^{-1}}{1-\rho z^{-1}})$.

The power transmission is

$$T=H^{*}H=\frac{c-\gamma e^{-j\omega t}}{1-c\gamma e^{-j\omega t}}\frac{c-\gamma e^{j\omega t}}{1-c\gamma e^{j\omega t}}=\frac{c^{2}-2\gamma c\cos(\omega t)+\gamma^{2}}{1-2\gamma c\cos(\omega t)+c^{2}\gamma^{2}},c=\rho \tag{2.45}$$

$$T_{\min}=\left(\frac{c-\gamma}{1-c\gamma}\right)^{2},\omega t=0,\text{on resonace} \tag{2.46}$$

$$T_{\max}=\left(\frac{c+\gamma}{1+c\gamma}\right)^{2},\omega t=\pi,off\ \text{resonace} \tag{2.47}$$

Extinction ratio of the ring response,

$$\frac{T_{\max}}{T_{\min}} = \left(\frac{c+\gamma}{1+c\gamma}\right)^2 \left(\frac{1-c\gamma}{c-\gamma}\right)^2 \tag{2.48}$$

When $c = \gamma$, from (2.19), we have $T_{\min} = 0$. This is the critical coupling.

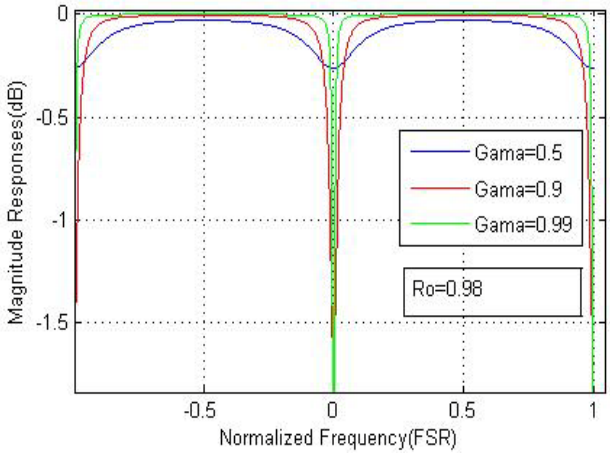

Fig. 8. Normalized amplitude response, $\rho = 0.98$.

Our goal is to make a filter with sharp amplitude response as shown in Fig. 8, γ is swept at 0.5, 0.9, 0.99 while $\rho = 0.98$. In Fig. 9, ρ is swept at 0, 0.5, 0.9 while $\gamma = 0.5dB$. The simulations show that the sharp response requires that both ρ and γ close to 1.

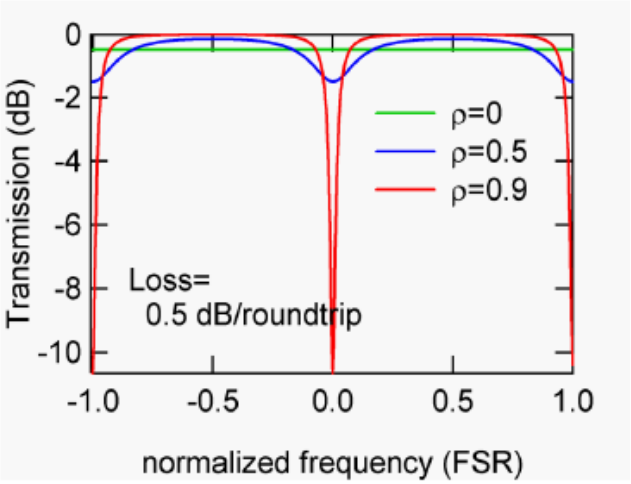

Fig. 9. Normalized amplitude response, $\gamma = 0.5dB$.

2.4. Electro-optical effect

The linear Electro-optic effect (or Pockels effect) produces refractive index change in certain types of crystals (such as $LiNbO_3$) induced by a constant or varying electric field. This index change is proportional to the field in Pockels effect whereas in Kerr effect it is quadratic in the field.

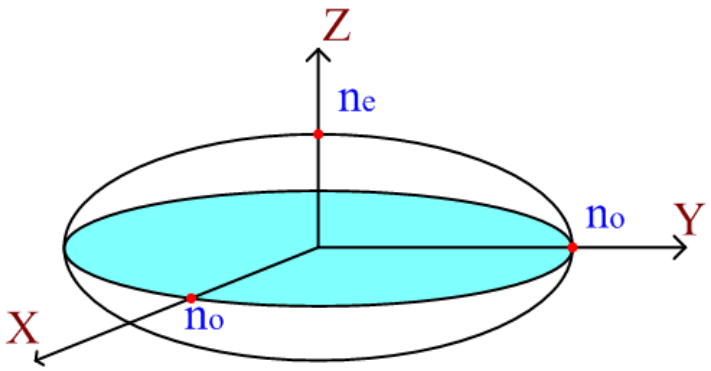

Fig. 10. Index ellipsoid of lithium niobate.

The index ellipsoid is used to describe the anisotropic property of these matericals (Fig. 10). And the The electro-optical properties are observed in ferroelectric crystals. In those crystals, the refractive index is dependent on crystal structure such that they exhibit optical anisotropy, i. e. the refractive index changes when varying the propagation direction. An index ellipsoid is introduced for such anisotropic material to determine the refractive index (Fig. 10). When the principal axes of the index ellipsoid coincide with x, y and z, the ellipsoid can be expressed by (2.49)

$$\frac{x^2}{n_x^2}+\frac{y^2}{n_y^2}+\frac{z^2}{n_z^2}=1 \tag{2.49}$$

or in terms of relative permittivity,

$$\frac{X^2}{\varepsilon_{11}}+\frac{Y^2}{\varepsilon_{22}}+\frac{Z^2}{\varepsilon_{33}}=1 \tag{2.50}$$

where $n_i^2 = \varepsilon_{jj}$. Re-arrange it by using the impermeability tensor:

$$B_{11}X^2 + B_{22}Y^2 + B_{33}Z^2 = 1 \tag{2.51}$$

where $B = \frac{1}{\varepsilon_r} = \frac{1}{n^2}$.

After the application of the electric field, the induced index ellipsoid is no longer aligned with the coordinate system and the off diagonal terms appears,

$$B'_{11}X^2 + B'_{22}Y^2 + B'_{33}Z^2 + 2B'_{23}YZ + 2B'_{31}ZX + 2B'_{12}XY = 1 \tag{2.52}$$

Renaming the coefficients for convenience,

$$B'_1X^2 + B'_2Y^2 + B'_3Z^2 + 2B'_4YZ + 2B'_5ZX + 2B'_6XY = 1 \tag{2.53}$$

The difference of the index ellipsoids with and without electric field,

$$\Delta B_i = B'_i - B_i \equiv \Delta\left(\frac{1}{n_i^2}\right) = \sum_{\substack{i=1,2,3 \\ j=1,2,\ldots 6}} r_{ij}E_j \tag{2.54}$$

Then rewrite it explicitly,

$$\begin{pmatrix} \Delta\left(\frac{1}{n_1^2}\right) \\ \Delta\left(\frac{1}{n_2^2}\right) \\ \Delta\left(\frac{1}{n_3^2}\right) \\ \Delta\left(\frac{1}{n_4^2}\right) \\ \Delta\left(\frac{1}{n_5^2}\right) \\ \Delta\left(\frac{1}{n_6^2}\right) \end{pmatrix} = \begin{pmatrix} r_{11} & r_{12} & r_{13} \\ r_{21} & r_{22} & r_{23} \\ r_{31} & r_{32} & r_{33} \\ r_{41} & r_{42} & r_{43} \\ r_{51} & r_{52} & r_{53} \\ r_{61} & r_{62} & r_{63} \end{pmatrix} \begin{pmatrix} E_1 \\ E_2 \\ E_3 \end{pmatrix} \tag{2.55}$$

The electro-optical tensor of $LiNbO_3$ (trigonal 3m crystal class) has the format

$$r_{ij} = \begin{pmatrix} 0 & -r_{22} & r_{13} \\ 0 & r_{22} & r_{13} \\ 0 & 0 & r_{33} \\ 0 & r_{51} & 0 \\ r_{51} & 0 & 0 \\ -r_{22} & 0 & 0 \end{pmatrix} \tag{2.56}$$

While the values at the wavelength of 632.8 nm are,

$$\begin{cases} r_{22} = 3.4 \times 10^{-12} m/V \\ r_{13} = 8.6 \times 10^{-12} m/V \\ r_{33} = 30.8 \times 10^{-12} m/V \\ r_{51} = 28 \times 10^{-12} m/V \end{cases} \tag{2.57}$$

By using the small argument binomial expansion, we can relate the Δn_i directly to electric field instead of the $\Delta\left(\frac{1}{n_i}\right)$,

$$\Delta n_i = -\frac{1}{2} n_i^3 \sum_{j=1}^{3} r_{ij} E_j \text{ for } i = 1, 2, ..., 6 \tag{2.58}$$

So the applied electric field component E_j changes the refractive indices linearly.

2.5. Multilayer and Bragg grating reflectors

2.5.1. Multilayer reflector

The multilayer dielectric films which consist of a stack of quarter-wave dielectric layers of alternate high and low index have large reflectivity and low loss. It is the best choice to be the nearly 100% mirrors of the cavities.

The following theory has two simple assumptions: (1) Normal incidence; (2) Negligible material absorption [38]. Several definitions are bought in first and then the derivations are performed to get the frequency response of the multilayer reflectors.

(a) Refractive index and admittance

$$N = n - ik = c / v = \sqrt{\varepsilon_r} \tag{2.59}$$

N is the complex refractive index, n is the real refractive index (or often simply refractive index), and k is the extinction coefficient. k is related with the absorption coefficient $\alpha = 4\pi k / \lambda$. The absorption is negligible for the dielectric materials As_2S_3 and SiO_2. c and v are the velocity of light in free space and in medium. ε_r is the relative dielectric permittivity.

The optical admittance is defined by the ratio of the magnetic and electric fields:

$$y = \eta = H / E = \sqrt{\varepsilon / \mu_0} \tag{2.60}$$

y is complex when the medium has absorption. In free space, y is real and is denoted by $y_0 = \sqrt{\varepsilon_0 / \mu_0} = 2.6544 \times 10^{-3} S$.

In medium,

$$y = N y_0 \tag{2.61}$$

The irradiance of the light is defined as the mean rate of the flow of the energy per unit area carried by the light wave. It is given by

$$I = \frac{1}{2} \mathrm{Re}(EH^*) = \frac{1}{2} n y_0 E E^* \tag{2.62}$$

(b) Reflection of a boundary

The incident beam is shooting from air (n_0) to substrate (n_1). And the continuities of the electric and magnetic tangential components are:

(1) Electric tangential component continuous across the boundary

$$\varepsilon_i + \varepsilon_r = \varepsilon_t \tag{2.63}$$

(2) Magnetic tangential component continuous across the boundary

$$y_0\varepsilon_i - y_0\varepsilon_r = y_1\varepsilon_t \tag{2.64}$$

Eliminating ε_t and ε_r, we obtain the amplitude coefficients:

$$\text{Reflection: } \rho = \frac{\varepsilon_r}{\varepsilon_i} = \frac{y_0 - y_1}{y_o + y_1} = \frac{n_0 - n_1}{n_0 + n_1} \tag{2.65}$$

$$\text{Transmission: } \tau = \frac{\varepsilon_t}{\varepsilon_i} = \frac{2y_0}{y_0 + y_1} = \frac{2n_0}{n_0 + n_1} \tag{2.66}$$

$$\text{Power reflection: } R = \rho^2 = \left(\frac{n_0 - n_1}{n_0 + n_1}\right)^2 \tag{2.67}$$

$$\text{Power transmission: } T = \frac{y_1}{y_0}\tau^2 = \frac{4n_0n_1}{\left(n_0 + n_1\right)^2} \tag{2.68}$$

(c) Reflection of a thin film and multilayer thin film

A single film has two interfaces, with air and with substrate. Use the same boundary conditions discussed above and combine all the multi-reflection beams with two positive-going and two negative-going waves in the film, four equations can relate the beams in the air and the beams in the substrate. A phase factor $\exp(i\delta)$ is introduced to relate the phase change between two interfaces to simplify the notations,

$$\delta = 2\pi N_1 d \cos(\vartheta_1)/\lambda \tag{2.69}$$

N_1 is the index of the film, d is the thickness of the film, ϑ_1 is the angle of the beam in the film(equals to zero in this discussion), λ is the wavelength.

Finally, a matrix can be derived to relate the amplitude of tangential components of E and H (subscript "a" is the 1st interface between air and the film and subscript "b" is the 2nd interface between film and substrate):

$$\begin{bmatrix} E_a \\ H_a \end{bmatrix} = \begin{bmatrix} \cos\delta & (i\sin\delta)/\eta_1 \\ i\eta_1 & \cos\delta \end{bmatrix} \begin{bmatrix} E_b \\ H_b \end{bmatrix} \tag{2.70}$$

Normalize it to E_b,

$$\begin{bmatrix} E_a/E_b \\ H_a/E_b \end{bmatrix} = \begin{bmatrix} B \\ C \end{bmatrix} = \begin{bmatrix} \cos\delta & (i\sin\delta)/\eta_1 \\ i\eta_1 & \cos\delta \end{bmatrix} \begin{bmatrix} 1 \\ \eta_2 \end{bmatrix} \tag{2.71}$$

This equation can calculate the admittance $y = \frac{H_a}{E_a} = \frac{C}{B}$ of the overall combination of the film and substrate and then the reflection:

$$\rho = \frac{\eta_0 - y}{\eta_0 + y} \tag{2.72}$$

$$R = \left(\frac{\eta_0 - y}{\eta_0 + y}\right)\left(\frac{\eta_0 - y}{\eta_0 + y}\right)^* \tag{2.73}$$

For multilayer films, the calculation can be simplified by similar matrix form:

$$\begin{bmatrix} B \\ C \end{bmatrix} = \left\{ \prod_{r=1}^{q} \begin{bmatrix} \cos\delta_r & (i\sin\delta_r)/\eta_r \\ i\eta_r & \cos\delta_r \end{bmatrix} \right\} \begin{bmatrix} 1 \\ \eta_{sub} \end{bmatrix} \tag{2.74}$$

where

$$\delta_r = \frac{2\pi N_r d_r \cos(\vartheta_r)}{\lambda} \xrightarrow{\text{our case}} \delta_r = \frac{2\pi n_r d_r}{\lambda} \tag{2.75}$$

Then the admittance is

$$y = \frac{C}{B} \tag{2.76}$$

Amplitude Reflection:

$$\rho = \frac{\eta_0 - y}{\eta_0 + y} \tag{2.77}$$

Intensity Reflection:

$$R = \left(\frac{\eta_0 - y}{\eta_0 + y}\right)\left(\frac{\eta_0 - y}{\eta_0 + y}\right)^* \tag{2.78}$$

Phase change:

$$Phase(\rho) = \arg\left(\frac{\eta_0 - y}{\eta_0 + y}\right) \tag{2.79}$$

(d) Quarter-wave dielectric layers

If the films have quarter-wave thickness, and the multilayer consists of an odd number of layers with high-index layers on the outside (p+1 layers of high index material and p layers of low index material), the equations in the previous section can be simplified by,

$$\delta_r = \lambda / 2 \tag{2.80}$$

The matrix becomes,

$$\pm\begin{bmatrix} 0 & i/\eta \\ i\eta & 0 \end{bmatrix} \tag{2.81}$$

$$y = \frac{n_H^{2P+2}}{n_L^{2P} n_{sub}} \tag{2.82}$$

Reflectance:

$$R = \left[\frac{1 - n_H^{2p+2} / (n_L^{2p} n_{sub})}{1 + n_H^{2p+2} / (n_L^{2p} n_{sub})} \right]^2 \approx 1 - 4 \frac{n_L^{2P} n_{sub}}{n_H^{2P+2}}, (when \frac{n_H^{2p+2}}{n_L^{2p} n_{sub}} > 1) \tag{2.83}$$

Reflection Loss:

When $R \approx 1$, $4 \frac{n_L^{2P} n_{sub}}{n_H^{2P+2}} = x \approx 0$,

$$L_{dB} = 10 \log(R) = 10 \log(1 - x) \approx 4.343 * (-x) = -4.343 * 4 \frac{n_L^{2P} n_{sub}}{n_H^{2P+2}} \tag{2.84}$$

Wavelength range:

$$\Delta g = \lambda_c \frac{2}{\pi} \arcsin(\frac{n_H - n_L}{n_H + n_L}) \tag{2.85}$$

2.5.2. Bragg grating reflector

The Bragg grating is a periodic perturbation of the refractive index along the length of the propagation. The first grating in fiber was demonstrated by Hill et al [39, 40] in 1978 by photo-induced refractivity.

Similar to the multilayer reflectors, the index of the Bragg grating through the propagation is a periodic structure, and the strongest interaction or mode-coupling occurs at the Bragg wavelength λ_B,

$$\lambda_B = 2 n_{eff} \Lambda \tag{2.86}$$

The n_{eff} is the modal index and the Λ is the grating period.

The grating filter characteristics can be modeled by several approaches [41-45]. The most important equations are listed since the detailed discussion is not necessary:

$$\Delta\lambda = \left[\frac{2\Delta n}{\pi}\right]\lambda_B \tag{2.87}$$

where Δn is the variation in the refractive index.

The peak reflection is approximately given by,

$$P_B(\lambda_B) \approx \tanh^2\left[\frac{N\Delta n}{n_{eff}}\right] \tag{2.88}$$

where N is the number of periodic variations.

CHAPTER III

SIMULATION*

3.1. Ti:$LiNbO_3$ waveguides

The simulation of the titanium (Ti) waveguides is mainly relied on the “mode solving” capability of the software. With the input refractive index profile at the cross sections of the waveguides, the computer software can solve the modes exist in the waveguides by numerical methods. We use the commercial software OptiBPM (from Optiwave) and FIMMWAVE (from Photo Design Ltd) to realize this work.

Before setting up the simulation, the modeling of the titanium diffused waveguides are discussed in Chapter II. In this chapter, we will use the model to simulate titanium diffused waveguides in lithium niobate.

3.1.1. Titanium diffusion parameters

In chapter 2.2.1, the model of titanium diffused waveguide in lithium niobate has been discussed. But the parameters still need to be extract from the results measured from our own fabricated samples.

In Table III, the experimental and simulated mode width data have been compared. The experiment mode data came from the mode profile measurements which will be discussed in chapter V. The waveguide mode has horizontal width and vertical width. They are expressed in full width at half maximum (FWHM) and they all have been measured and simulated. In bottom part of this table, the simulated widths have been compared with the measured data and the variations have been listed beside them.

Table III. Experimental and simulated mode width data comparison

Experimental Data							
Sample ID	Polarization	Ti thickness(A)	D time (h)	H_FWHM (μm)	V_FWHM (μm)	H/V	Mode Index
RC39	TE	920	9.5	5.3143	3.8674	1.37	
RC39	TM	920	9.5	8.1321	5.8542	1.38	
RC40	TE	950	9.5	5.8058	4.3579	1.33	
RC40	TM	950	9.5	7.8936	4.8422	1.63	ne=2.1381
RC58	TE	1290	13	5.6058	3.5968	1.57	no=2.2112
RC58	TM	1290	13	7.2035	3.9145	1.84	
				TE purple	TM: black		
OptiBPM							
Sample ID	Polarization	Ti thickness(A)	D time (h)	H FWHM (μm)	V FWHM (μm)	H/V	Mode Index
RC39	TE	920	9.5	5.5629 (+4.57%)	3.4437 (-11.6%)	1.62	2.139918
RC39	TM	920	9.5	7.5497 (-7.43%)	4.6358 (-23.2%)	1.63	2.212114
RC40	TE	950	9.5	5.5629 (-4.27%)	3.5762 (-19.7%)	1.56	2.140064
RC40	TM	950	9.5	7.5497 (-4.45%)	4.6358 (-4.35%)	1.63	2.212156
RC58	TE	1290	13	5.5629 (-1.70%)	3.5762 (-0.57%)	1.56	2.140934
RC58	TM	1290	13	7.5497 (+4.69%)	4.7682 (+19.7%)	1.58	2.212592

The diffusion parameters in (2.33) and (2.34) were fitted from Table III to minimize the variation between the measurements and simulations.

3.1.2. Basic Ti:$LiNbO_3$ waveguide simulations

The simulation was performed by OptiBPM [46].

(a) Refractive index distributions

The refractive index distributions have been generated by inputting the waveguide dimensions along with the diffusion parameters: diffusivities (at specific temperature), diffusion time, titanium strip thickness and width before diffusion. The refractive indices are plotted in Fig. 11.

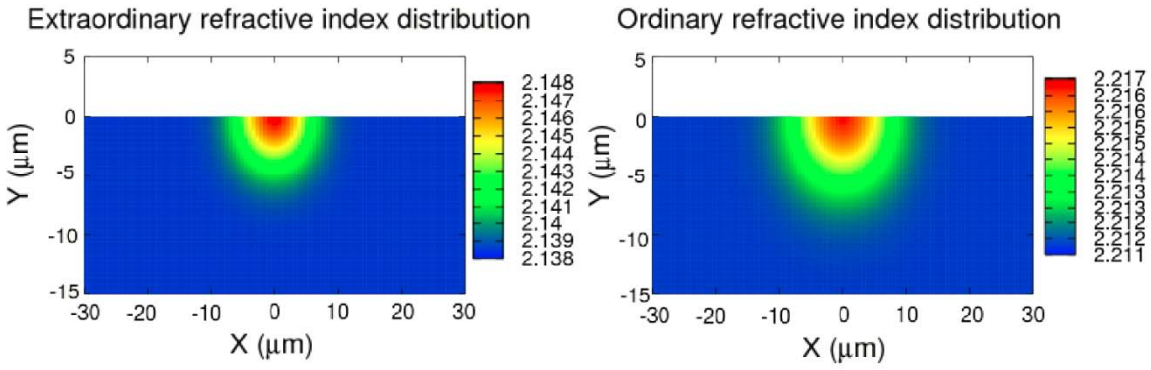

Fig. 11. Extraordinary (left) and ordinary (right) refractive index distributions calculated using optiBPM.

The substrate extraordinary refractive index was set to n_e = 2.138615 and n_o = 2.211868 for the ordinary both at 1531 nm. The diffused distributions show a maximum

index contrast of $\Delta n_e = 0.00857$ for the extraordinary index and $\Delta n_o = 0.00478$ for the ordinary.

(b) Optical modes profiles

Using the refractive index distributions shown in Fig. 11, the mode profiles for both TE and TM modes were calculated. The results are plotted in Fig. 12.

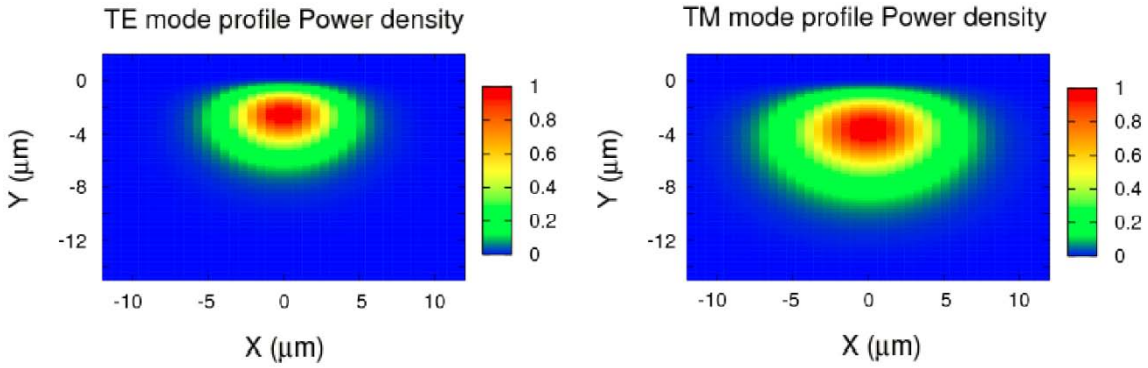

Fig. 12. Calculated power density distributions for the TE and TM fundamental optical modes. (Left is TE; Right is TM.)

In Fig. 13 are shown the calculated and measured horizontal profiles for the TE and TM modes. The calculated and measured vertical mode profiles for the TE and TM optical modes are plotted in Fig. 14.

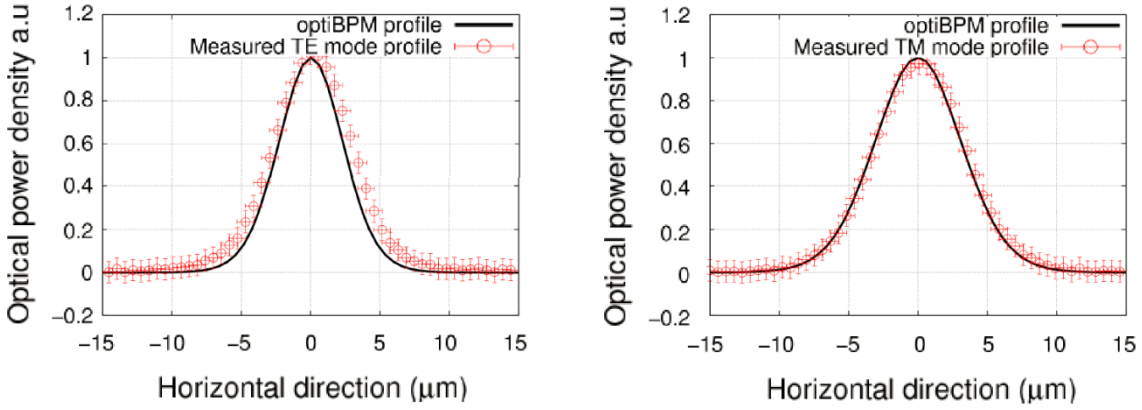

Fig. 13. Calculated and measured horizontal mode profiles for the TE and TM fundamental optical modes in 2D.

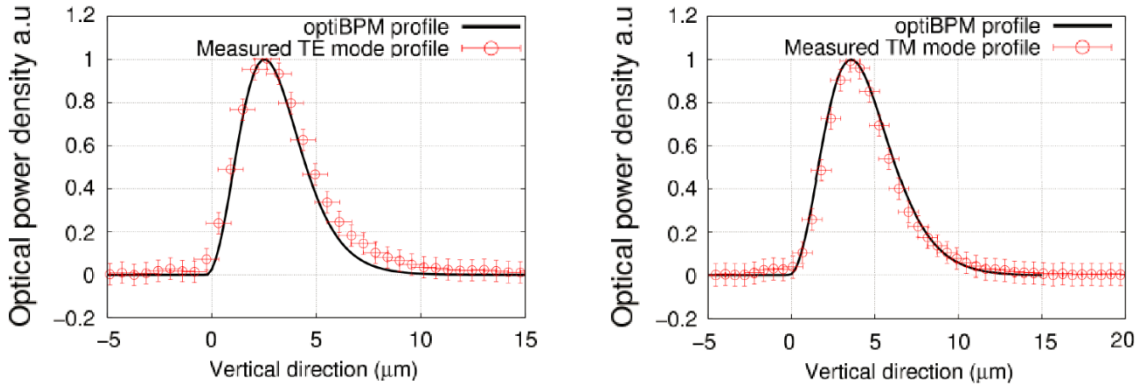

Fig. 14. Calculated and measured vertical mode profiles for the TE and TM fundamental optical modes in 2D.

For both optical modes at 1531nm, the horizontal profile fits to a Gaussian function while in the vertical fits to a Hermite-Gaussian function. For the optical TE mode at 1531nm, the measured horizontal size parameter is $w_s(TE) = 8.7 \pm 0.9$ µm and the vertical is $d_s(TE) = 3.4 \pm 0.5$ µm. The calculated mode sizes in both directions were

similar to the experimental data within the uncertainties. A better match was found for the optical TM mode. The measured mode size parameters are $w_s(TM) = 9.8 \pm 0.9$ μm and $d_s(TM) = 4.3 \pm 0.5$ μm.

The full-size of the optical input-fiber mode was also calculated and measured with a good agreement between them. The fiber mode size is $s_s = 7.4 \pm 0.5$ μm. From the calculated optical fiber and waveguide modes, we can compute the mismatch-mode losses using the 3D overlap integral tool for each mode. The mismatch-mode losses are $L_c(TE) = 0.5$ dB and $L_c(TM) = 0.7$ dB.

Similar deductions were carried out for the pump mode (1488nm). The horizontal size parameter of the optical mode is $w_p = 7.5 \pm 0.9$ μm. In vertical direction is $d_p = 3.8 \pm 0.5$ μm. The size of the optical fiber mode at 1488 nm is $s_p = 6.5 \pm 0.5$ μm leading to a mismatch-mode loss of $L_c(pump) = 0.4 \pm 0.1$ dB.

After the simulation, inspect the intensity profile. There will always showing high order modes. Only if their intensities decay to zero near the boundary, they truly exist. And the mode effective index must be high than the substrate refractive index. These are the criteria that help us to find when 2^{nd} mode comes out.

3.1.3. Coupling loss between Ti:$LiNbO_3$ modes and fiber modes

The Coupling loss between titanium diffused waveguide modes and fiber modes have been simulated. The titanium diffusion parameters have been swept.

(a) Simulation setup

The simulation was operated on OptiBPM. This simulation was trying to sweep two parameters: diffusion time and Ti thickness before diffusion and to find the best overlap between W/G and fiber modes (both TE and TM mode). The overlap represents the mode mismatch loss which is the major part of the coupling loss between the W/G and fiber. This part is very similar to part1. The difference is that we change the Er distribution to Fiber mode. The wavelength was set at 1531nm.

The fiber has the following parameters (Other parameters are set as default):

Core Radius: Rx=Ry=4.07μm.

Refractive Index: Core=1.45204; Cladding=1.44681.

The single straight waveguide has the following parameters (Other parameters are set as default):

Strip Ti width before diffusion: 7μm.

Temperature coefficient: 303000 K;

Diffusion Temperature: 1025 $^{\circ}C$.

Diffusion Constants:

$$D_{oV} = 0.0199 cm^2 / s$$
$$D_{oH} = 0.0289 cm^2 / s$$

(b) Results

The overlaps between W/G and fiber modes were calculated by Matlab.

$$coupling\ loss = \frac{\int \Psi_{fiber} \Psi_{WG} dS}{\sqrt{\int \Psi_{fiber}^2 dS \int \Psi_{WG}^2 dS}} \tag{3.1}$$

Overlaps for TE modes in Table IV, the best mode is at Diffusion time=11 hrs, Ti thick=600Å.

Table IV. Overlap between waveguide and fiber mode for TE mode.

Diffus	600	700	800	900	1000	1100	1200	1300	1400	1500
4	-0.733									
5	-0.598	-0.806								
6	-0.511	-0.663	-0.831							
7	-0.456	-0.565	-0.705	-0.828						
8	-0.423	-0.495	-0.606	-0.713	-0.818					
9	-0.406	-0.449	-0.531	-0.624	-0.712	-0.802				
10	-0.398	-0.42	-0.477	-0.557	-0.63	-0.707	-0.786			
11	-0.397	-0.404	-0.439	-0.502	-0.566	-0.631	-0.699	-0.767		
12	-0.404		-0.416		-0.516	-0.57	-0.628	-0.687	-0.749	
13	-0.413					-0.523	-0.572	-0.623	-0.676	-0.732
14	-0.425						-0.525	-0.571	-0.617	-0.665
15	-0.439							-0.527	-0.568	-0.61
16	-0.454								-0.528	-0.564
17	-0.47									-0.527

The x-axis is Titanium thickness before diffusion by angstrom, the y-axis is diffusion time by hour. The unit of data is dB.

Overlaps for TM modes in Table V, the best mode is at Diffusion time=15 hrs, Ti thick=1500A.

Table V. Overlap between waveguide and fiber mode for TM mode.

Diffus	600	700	800	900	1000	1100	1200	1300	1400	1500
4	-0.308									
5	-0.294	-0.295								
6	-0.287	-0.283	-0.288							
7	-0.285	-0.275	-0.276	-0.282						
8	-0.287	-0.273	-0.269	-0.27	-0.276					
9		-0.276	-0.267	-0.264	-0.266	-0.271				
10			-0.269	-0.262	-0.26	-0.261	0.2654			
11				-0.264	-0.259	-0.257	-0.258	-0.261		
12					-0.261	-0.256	-0.254	-0.255	-0.257	
13						-0.259	-0.255	-0.253	-0.252	-0.254
14							-0.258	-0.254	-0.251	-0.251
15								-0.257	-0.253	-0.25
16									-0.257	-0.253
17										-0.257

In this table, the x-axis is titanium thickness before diffusion (unit: angstrom), the y-axis is diffusion time by hour. The data is in unit of dB.

(c) Conclusions

(1).The best overlap for TE and TM mode are at different diffusion time and Ti Thickness.

(2).The average of the vertical and horizontal FWHM of the W/G mode is related to the overlap.

For the fiber, $V_{FWHM} = H_{FWHM} = 5.56u$. For Ti waveguide, If $\overline{FWHM} = \frac{V_{FWHM} + H_{FWHM}}{2}$ is close to 5.56 μm, then it will get best overlap. TM modes'

$\overline{FWHM}$ are closer to 5.56 μm. So TM modes have better overlap. They are shown as Fig. 15.

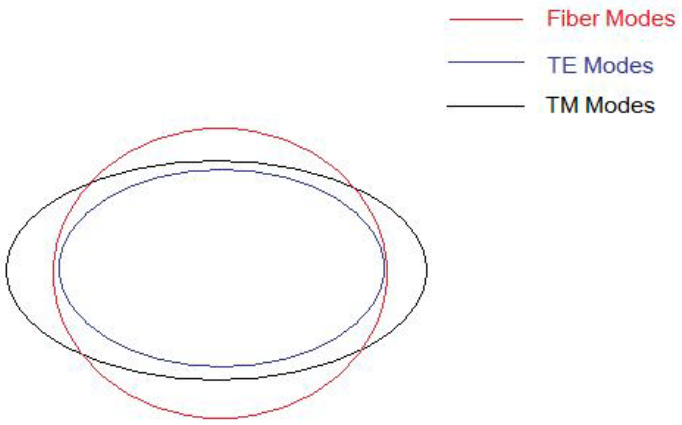

Fig. 15. Mode size comparison between TE, TM and fiber.

3.2. Hybrid waveguides

3.2.1. Er doped Ti:$LiNbO_3$ waveguides

For the erbium doped waveguide simulation, best gain is our goal. There are two means in our consideration: increase the gain and decrease the loss. To increase the gain, we got to let the optical mode overlap better with the Er distribution. To decrease the loss, except lowering the propagation loss by better fabrication skills, we got to lower the coupling loss which is proportional to the overlap between waveguide mode and

fiber mode. We did these by sweep fabrication parameters: Ti diffusion time, Ti thickness before diffusion, As_2S_3 width and thickness, Er profile depth.

The softwares are OptiBPM, Optisystem and FIMMWAVE.

i. The simulation of Er gain versus Ti diffusion variation by OptiBPM.

The simulation was trying to sweep two parameters: diffusion time and Ti thickness before diffusion and to find the best overlap between W/G modeds (both TE and TM modes) and Er profile. The overlap represents the mode gain [47].

(1). Ti:$LiNbO_3$ mode solving.

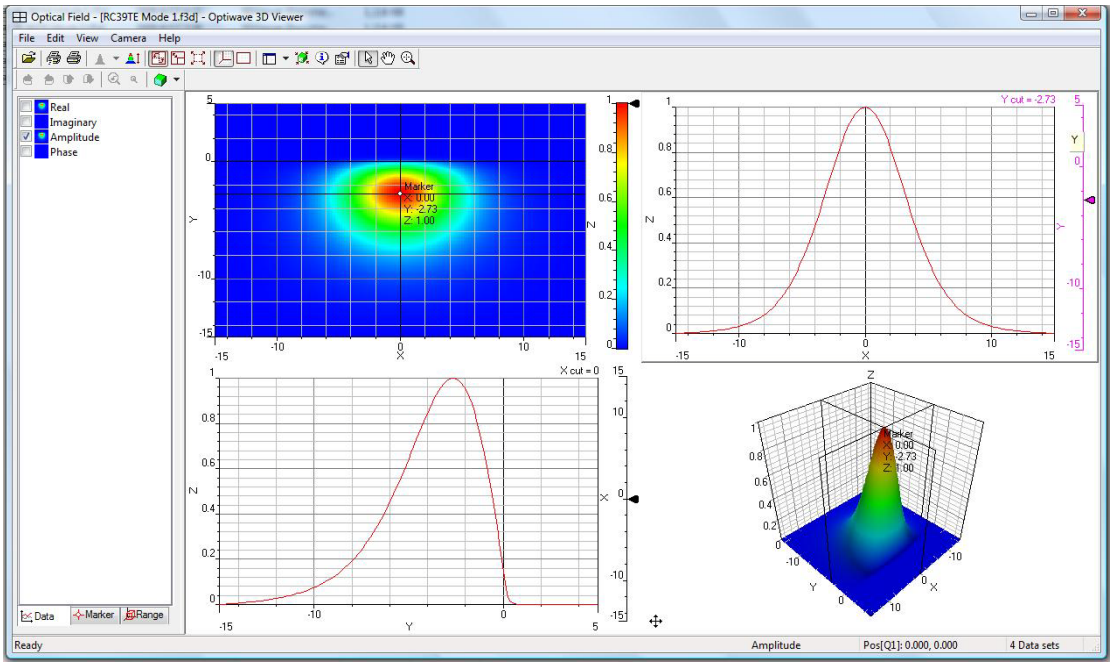

Fig. 16. Ti:$LiNbO_3$ waveguide mode solving.

Ti:$LiNbO_3$ waveguide was simulated by OptiBPM. The mode (amplitude or intensity distribution) was shown in Fig. 16. The single straight waveguide has the following parameters (Other parameters are set as default): Strip Ti width before diffusion: 7μm; Temperature coefficient:303000 K; Diffusion Temperature: 1025 $^{\circ}C$; Diffusion Constants: $D_{oV} = 0.0199cm^2/s, D_{oH} = 0.0289cm^2/s$

(2). Er Distribution

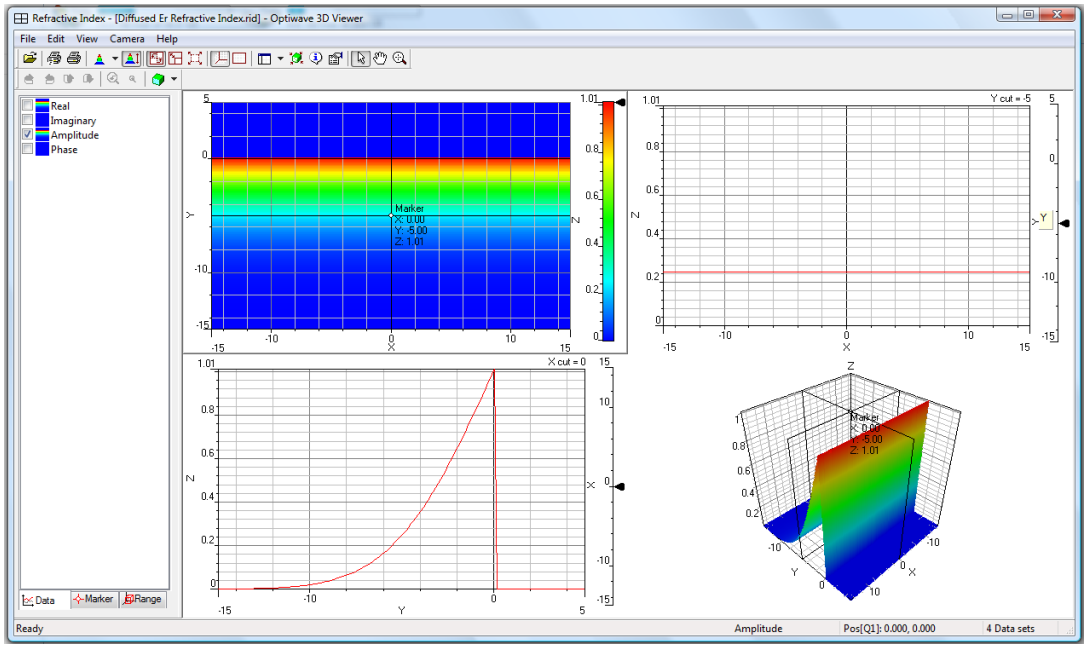

Fig. 17. Er density distribution.

The Er density distribution erfc(y) can be created by OptiBPM in Fig. 17 or by Matlab. We keep the diffusion depth at 6 μm to fit the experiment data.

(3). Calculate overlap between the waveguide mode and Er distribution.

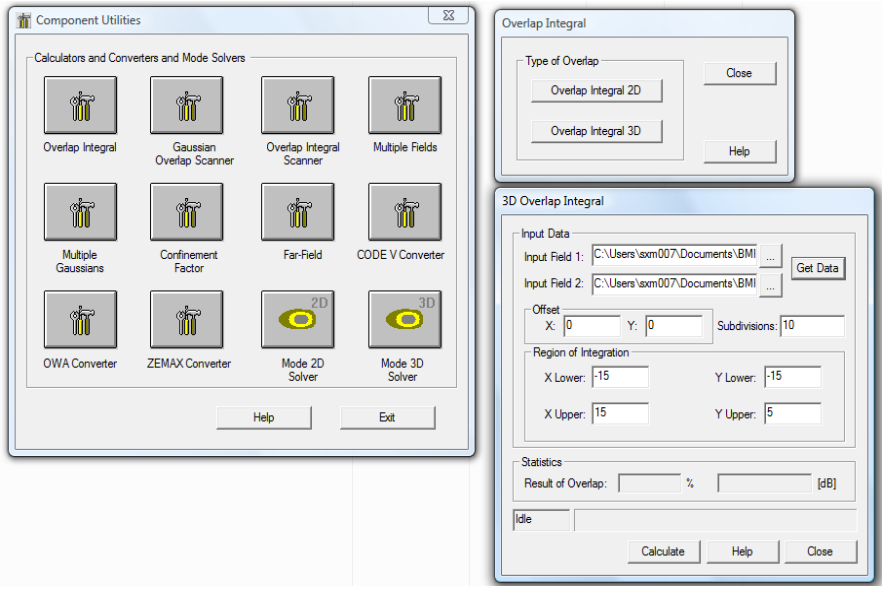

Fig. 18. The calculation of overlap between mode and Er distribution.

The overlap between mode and Er distribution can be done by tools in OptiBPM (Fig. 18) or by Matlab code. The modes has been normalized to make sure $\int E \bullet ds = 1$.It keeps the total power=1. The Er distribution has been normalized to make Peak concentration on the surface equal to one: $Max(I_{Er}) = 1$.

And the Overlap of gain can be expressed by, $Overlap = \int E^2 \bullet I_{Er} ds$

(a) Overlaps for TE modes (Table VI)

Table VI. Overlap versus Ti thickness and diffusion time for TE mode.

Diffus	600	700	800	900	1000	1100	1200	1300	1400	1500
4	-2.898									
5	-3.202	-2.832								
6	-3.479	-3.097	-2.833							
7	-3.726	-3.342	-3.057	-2.866						
8	-3.95	-3.571	-3.274	-3.065	-2.905					
9	-4.16	-3.783	-3.483	-3.256	-3.087	-2.948				
10	-4.35		-3.678	-3.435	-3.26	-3.114	-2.99			
11	-4.53			-3.612	-3.425	-3.275	-3.145	-3.034		
12	-4.695				-3.583	-3.429	-3.295	-3.179	-3.076	
13	-4.85					-3.574	-3.437	-3.318	-3.212	-3.117
14	-4.995						-3.576	-3.452	-3.343	-3.244
15	-5.132							-3.581	-3.47	-3.369
16	-5.26								-3.59	-3.488
17	-5.378									-3.603

The x-axis is Titanium thickness before diffusion by angstrom, the y-axis is diffusion time by hour. The data is in unit of dB.

(b) Overlaps for TM modes (Table VII)

Table VII. Overlap versus Ti thickness and diffusion time for TM mode.

Diffus	600	700	800	900	1000	1100	1200	1300	1400	1500
4	-4.594									
5	-4.698	-4.465								
6	-4.814	-4.599	-4.42							
7	-4.938	-4.736	-4.564	-4.418						
8	-5.064	-4.869	-4.706	-4.563	-4.441					
9		-5	-4.84	-4.701	-4.581	-4.474				
10			-4.968	-4.835	-4.716	-4.61	-4.514			
11				-4.957	-4.841	-4.735	-4.644	-4.56		
12					-4.962	-4.858	-4.767	-4.68	-4.604	
13						-4.974	-4.88	-4.797	-4.721	-4.651
14							-4.991	-4.909	-4.833	-4.763
15								-5.016	-4.94	-4.87
16									-5.039	-4.972
17										-5.067

The x-axis is Titanium thickness before diffusion by angstrom,the y-axis is diffusion time by hour. The data is in unit of dB.

(4). Conclusion.

The mode closest to the surface where has larger Er concentration has the best overlap: for TE, it is at 700Å, 5 hours; for TM, it is at 900Å, 7 hours.

ii. The simulation of Er gain versus Er intrinsic parameters' variations by OptiSystemstem

In this part, we use Er doped waveguide module in Optisystem to simulate the gain. This module can calculate the gain from input waveguide cross-section refractive

index distribution and Er distribution. Pump and CW Laser parameters are in Table VIII and

Table IX. Er doped waveguide amplifier (EDWA) parameters are listed in APPENDIX B.

Table VIII. Pump laser parameters.

Name	Value	Units	Mode
Frequency	1480	nm	Normal
Power	90	mW	Normal

Table IX. CW laser parameters

Name	Value	Units	Mode
Frequency	1531	nm	Normal
Power	-30	dB	Normal
Linewidth	10	MHz	Normal
Intial phase	0	deg	Normal

(a) Gain vs. Er_D_{eff}

In this part, we swept the Er_D_{eff} (Er effective diffusion depth) from 3 μm to 7 μm to see how sensitive the gain changes with it. Fig. 19 and Table X is the Er ion density distribution setup and Table XI is the result.

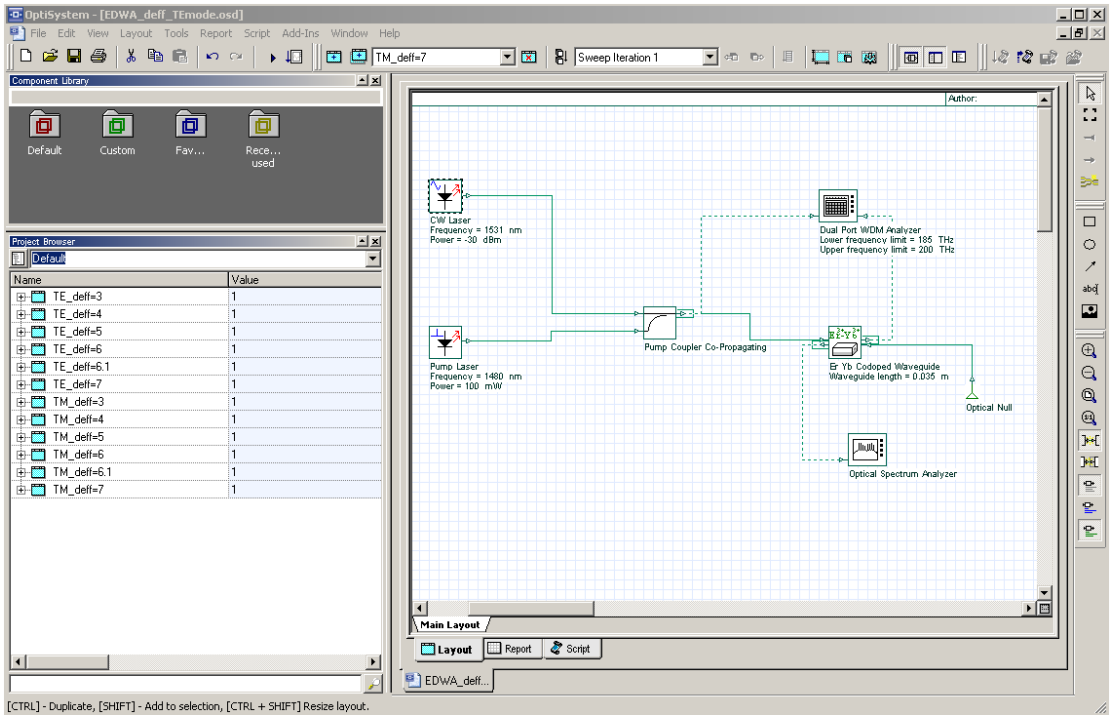

Fig. 19. Optisystem setup: sweeping Er_Deff.

Table X. Er ion density setup

Name	Value	Units	Mode
Er ion density distribution	Er Profiles which have Deff=3~7 μm	No	Normal

Table XI. Gain (dB) versus Er_D_{eff}

Gain(dB)	3	4	5	6	6.1	7
TE	-1.312	-1.262	-1.257	-1.286	-1.291	-1.336
TM	-1.095	-0.806	-0.545	-0.34	-0.323	-0.196

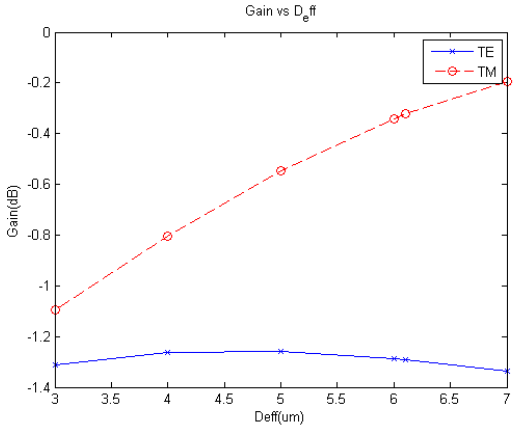

Fig. 20. Gains change with D_eff.

To Conclude, Fig. 20 shows that the gain is sensitive to D_eff for TE modes, but not sensitive for TM modes. This may because that the TM modes are much deeper than TE mode.

(b) Gain vs. Er_strip_width

We usually use planar Er (Fig. 21, but infinite wide) in simulation and in experiment. Now we try strip Er (Fig. 22) instead to see how sensitive the gain changes with the Er strip width.

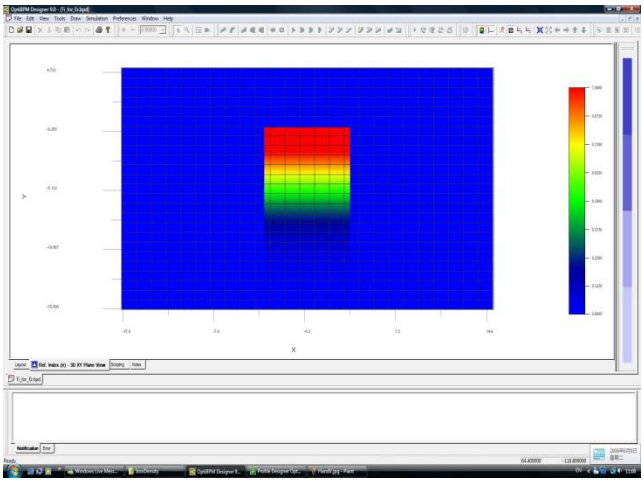

Fig. 21. Planar diffused Er.

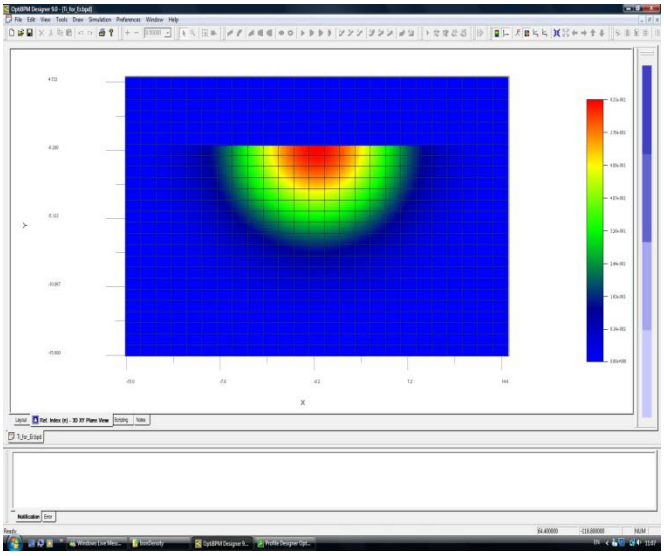

Fig. 22. Strip diffused Er.

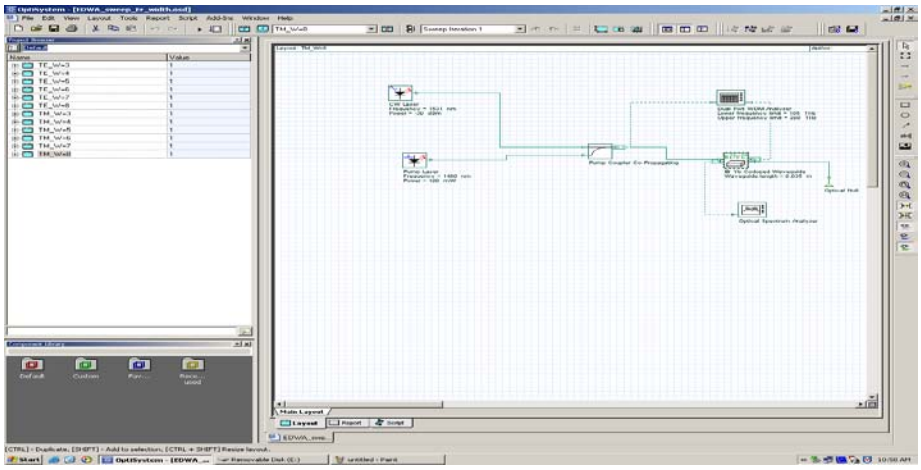

Fig. 23. Optisystem setup: sweeping Er strip width.

Fig. 23 is the setting for Optisystem. Table XII and Fig. 24 are the results.

Table XII. Gain (dB) versus Er strip width.

Er Width	3	4	5	6	7	8
TE	-1.026	-1.031	-1.037	-1.045	-1.054	-1.064
TM	0.9096	0.9051	0.8989	0.891	0.8814	0.8701

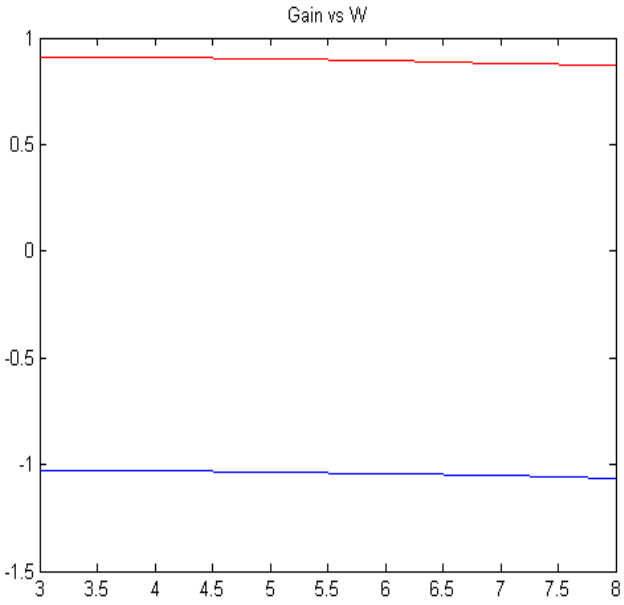

Fig. 24. Gain changes with Er width (TE,blue; TM, red.)

To conclude, the gain is not sensitive to the strip width of Er.

(c) Gain vs. Pp vs. Cup

In this part, we simulated the gain change with pump power and up-conversion coefficient. The up-conversion coefficient represents how many percentage of power has been wasted on radiation to other wavelength.

Table XIII and Table XIV give the setup parameters.

Table XIII. Up_convertion parameters.

Name	Value	Units	Mode
Calculate upconversion effects	Yes		Normal
Cup	5~15e-24	m^3/s	Sweep
C3	100e-24	m^3/s	Normal
C14	70e-24	m^3/s	Normal
C16	70e-24	m^3/s	Normal

Table XIV. Pump parameters setup

Name	Value	Units	Mode
Frequency	1480	nm	Normal
Power	0~100(by 10)	mW	Sweep

Other parameters are the same as Table VIII and Table IX.

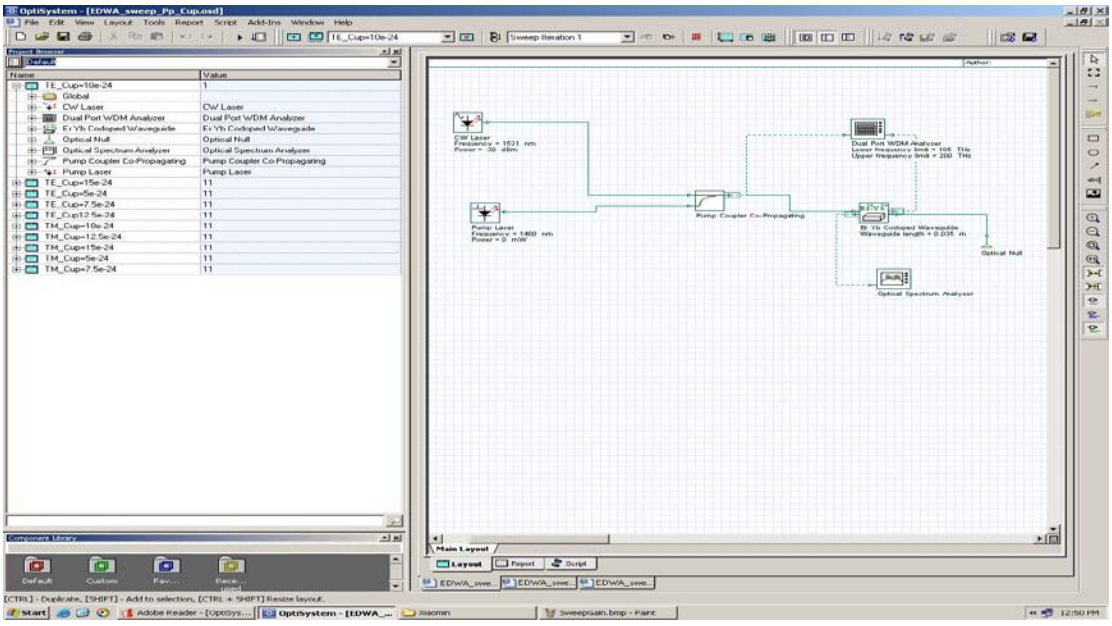

Fig. 25. Optisystem setup: sweeping C_{up}.

Fig. 25 is the setting for Optisystem. The results are in Fig. 26 and Fig. 27.

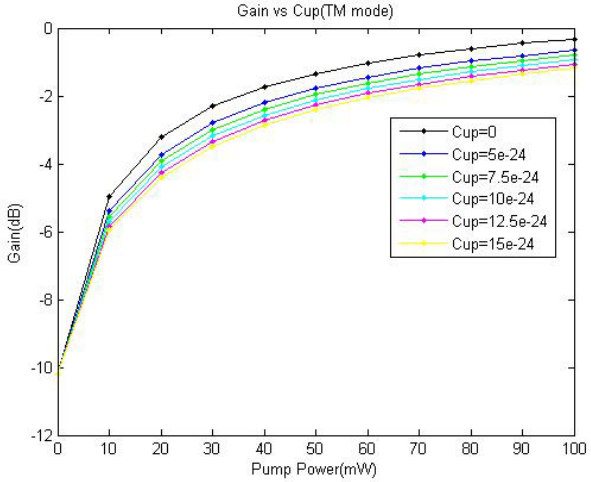

Fig. 26. Gain changes with Pp and C_{up} for TM mode.

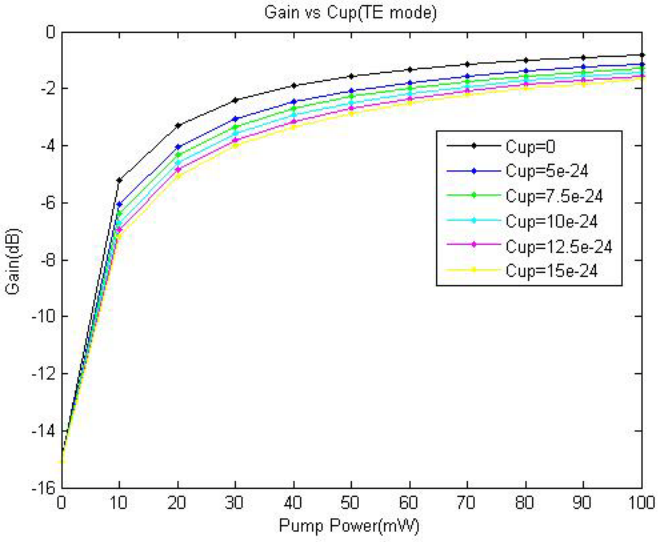

Fig. 27. Gain changes with Pp and C_{up} for TE mode.

The conclusion is that the gain decreases with up conversion coefficient.

(d) Gain vs. ion density & life time

The setup is the same as Fig. 25 but with different parameters sweeping: ion density and Er metastable-lifetime.

Table XV shows the input parameters and Fig. 28 gives the results:

Table XV. Setting for sweeping Er metastable lifetime.

Name	Value	Units	Mode
Er metastable lifetime	1.7~2.7	ms	Sweep

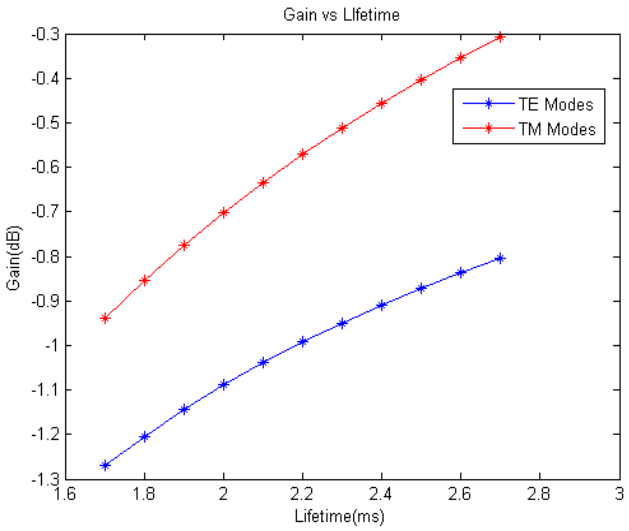

Fig. 28. Gain changes with Er metastable lifetime.

Table XVI sweeps Er ion density and Fig. 29 gives the results.

Table XVI. Setting for sweeping Er ion density.

Name	Value	Units	Mode
Er ion density	1E24~1.6E24	m^{-3}	Sweep

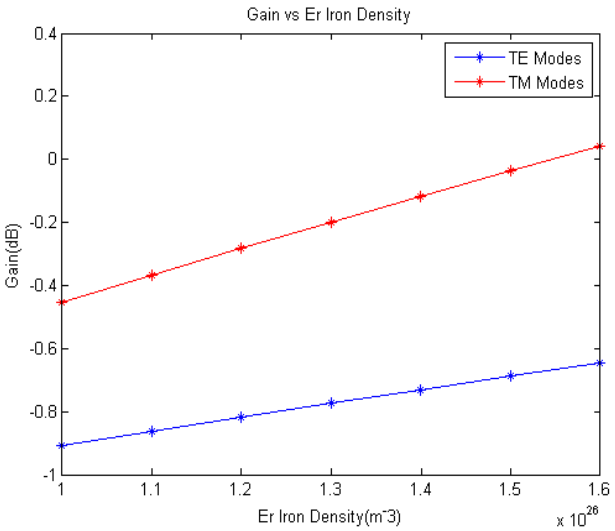

Fig. 29. Gain changes with Er ion density.

The conclusions are: (1) The gain increase with Er meta-stable Lifetime (Fig. 28); (2) The gain is proportional to the Er ion density (Fig. 29).

(e) Gain vs. Er thickness

Equation (2.35) and (2.36) show that the Er profile are proportional to the Er thickness τ when diffusion time is fixed. And the Er ion density is also proportional to

the Er surface concentration. The optisystem simulation Fig1 showed that the Gain is proportional to the Er ion density. So it means the Gain is proportional to the Er thickness τ. Overlap simulation

The ovelap calculation is

$$\Gamma = \int E \cdot I_{Er} ds \tag{3.2}$$

E is the normalized electric field and the I_{Er} is the Er ion density profile which is also proportional to the Er thickness τ. So the overlap simulation agree with that if the Er diffusion time doesn't change, the Gain should be proportional to the Er thickness τ. Measured data in Table XVII are from experiments, and the best results (>-1dB) were chosen.

Table XVII. Propagation gain versus Er thickness

Propagation Gain(dB/cm)		
Er Thickness(nm)	TE	TM
11	0.1	-0.8
11	-0.6	
11	-0.1	
14	0.3	1
17	0.9	1.3
19	1.3	1.2

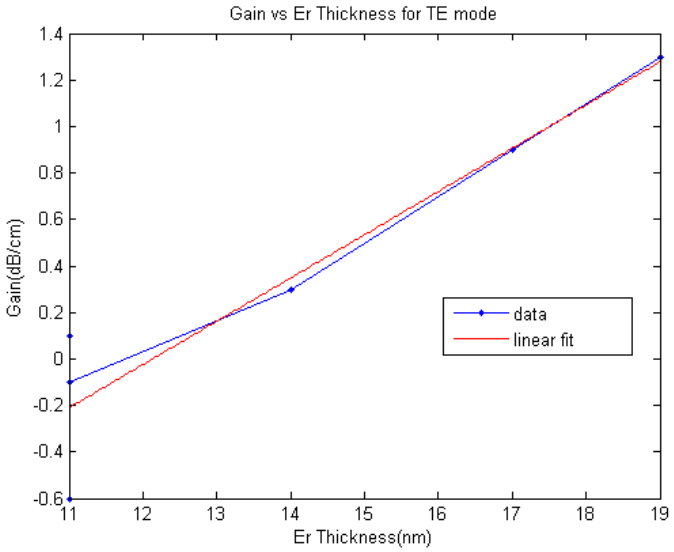

Fig. 30. Gain (dB/cm) changes with Er thickness for TE mode.

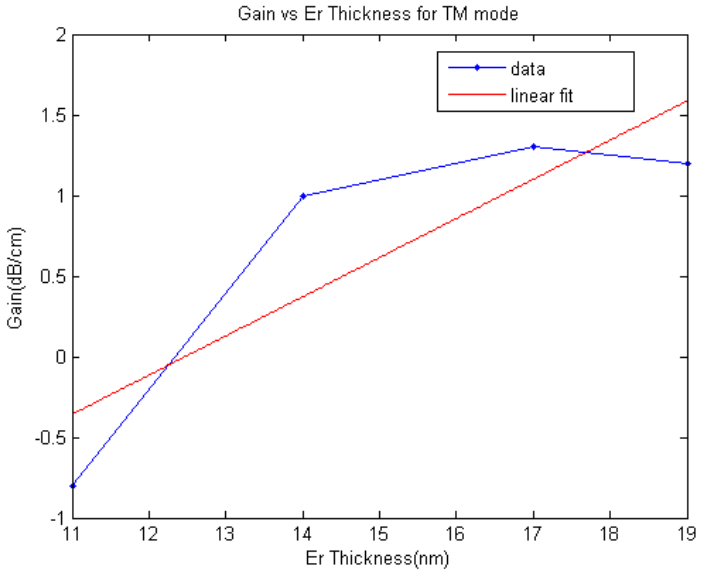

Fig. 31. Gain (dB/cm) changes with Er thickness for TM mode.

The Fig. 30 and Fig. 31 agree with (3.2). If we increase the Er thickness while keeping the depletion time shorter than the diffusion time, we can get more gain.

3.2.2. As_2S_3 waveguides on top of the TiLLiNbO$_3$ waveguides

In the part, we want to introduce As_2S_3 ridge waveguide on top of Ti diffused $LiNbO_3$ waveguide to pull the mode to surface to increase the gain. We used FIMMWAVE, by Photon Design Ltd, which is is capable for solving these kind of mixed waveguides including both diffused and ridge guide to solve the optical modes by film mode matching (FMM) method at 1531 nm for the signal and 1480 nm for the pump. Fig. 32 shows the structure of the vertical integration between an Er:Ti:$LiNbO_3$ and an As_2S_3 waveguides. The device is made on an x-cut y-propagation lithium niobate substrate with planner diffused Er. The titanium diffused waveguide is in the center, while the As_2S_3 waveguide is placed next to it above the surface.

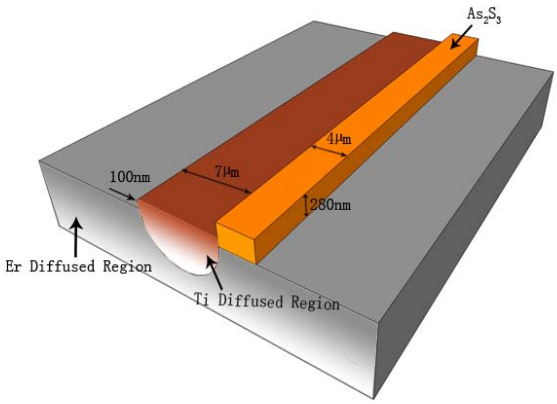

Fig. 32. Schematic picture of our structure.

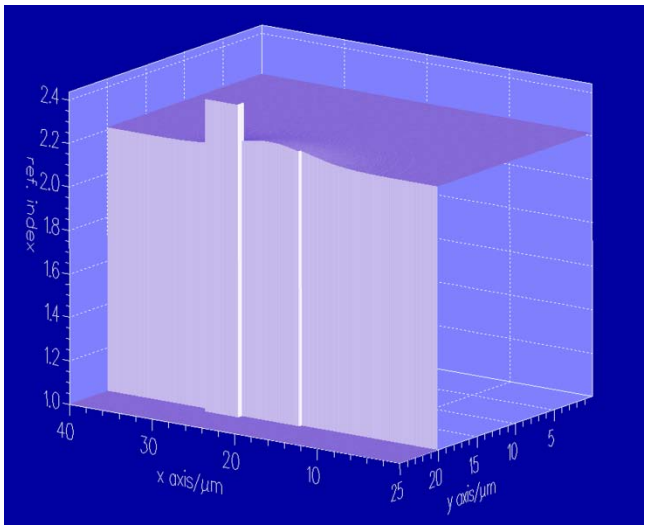

Fig. 33. Refractive index profile for TM mode: Z-axis is refractive index (1.0-2.4); X-axis is waveguide width (0-40 μm); Y-axis is waveguide depth (0-25 μm).

Fig. 33 illustrates the refractive index profile of the waveguide. The index value is shown in z-axis and the waveguide cross section is shown in x-y plane. Corresponding to the structure in Fig. 33, the As_2S_3 waveguide is represented by the protruding pole (n=2.4) with the bump next to it, on which the swelled part is the titanium diffused region in lithium niobate substrate (the bulk part, $n_{TM}=2.21+\Delta n_{Ti\text{-}diffused\text{-}TM}$, $n_{TE}=2.13+\Delta n_{Ti\text{-}diffused\text{-}TE}$). The air cladding (n=1) is at the bottom.

As we swept the dimensions of the As_2S_3 waveguide, we found that the thickness of the As_2S_3 thin film is the most sensitive parameter. The As_2S_3 width must be larger than 2 μm to pull up the mode, but further increasing the width to infinity only changes the overlap by 17%. However, changing the thickness from 0 to 0.5 μm changes the overlap by 230%. So, we set the As_2S_3 width to 4 μm and subsequently swept the thickness.

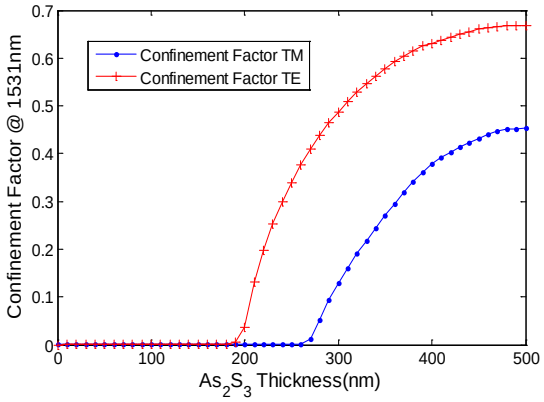

Fig. 34. Confinement factor in As_2S_3 at signal wavelength (1531 nm) for both TM and TE modes.

The resulting confinement factor which is the percentage of optical intensity in As_2S_3 is shown in Fig. 34. It increases with the As_2S_3 waveguide thickness.

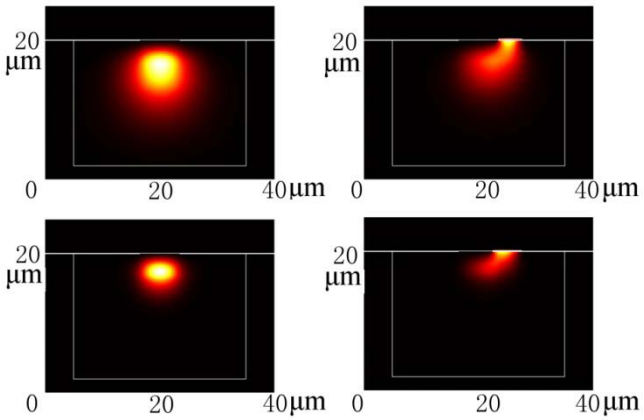

Fig. 35. (1) Top left is the TM mode without As_2S_3. (2) Top right is the TM mode with 0.28 μm thick As_2S_3. (3) Bottom left is the TE mode without As_2S_3. (4) Bottom right is the TE mode with 0.2 μm thick As_2S_3.

The Er profile was measured by Secondary Ion Mass Spectrometry (SIMS). The effective depth is deff = 4.9 μm after fitting for the complementary error function. Using the optical modes and Er profile, the overlap integral Γ between the modes and Er profile expressed by (6) can be simulated. Fig. 35 shows the simulated mode profiles and the mode pulling effect. Having considered the overlap between the mode and Er (Fig. 36), and pump effects (Fig. 37~Fig. 41), the optimum thicknesses for TM and TE are found to be 280 nm and 200 nm respectively.

Fig. 36 shows the overlap of the signal modes and Er profile. We normalized all the overlap data relative to the overlap when the As_2S_3 thickness equals to zero. For TM mode, the overlap starts from 1 and increases slowly at 0-0.2 μm, but changes dramatically at 0.25-0.3 μm. After 0.3 μm, it falls. After 0.5 μm, it falls below 1 since 45% power of mode has spread into the As_2S_3 area and can't be pumped since there is no Er there. The mode is over-pulled. The overlap for the TE mode shows a similar curve, with the peak at 0.21 μm.

The As_2S_3 waveguide not only enhances the modes and Er overlap, but also influences the pump to signal mode mismatch $O_{S\&P}$ and pump to fiber modes coupling OP&F. They are defined in (3.3) and (3.4) and plotted as curves in Fig. 36.

$$O_{S\&P} = \iint_A \Psi_s(x,y)\Psi_P(x,y)dxdy \tag{3.3}$$

$$O_{P\&F} = \iint_A \Psi_p(x,y)\Psi_f(x,y)dxdy \tag{3.4}$$

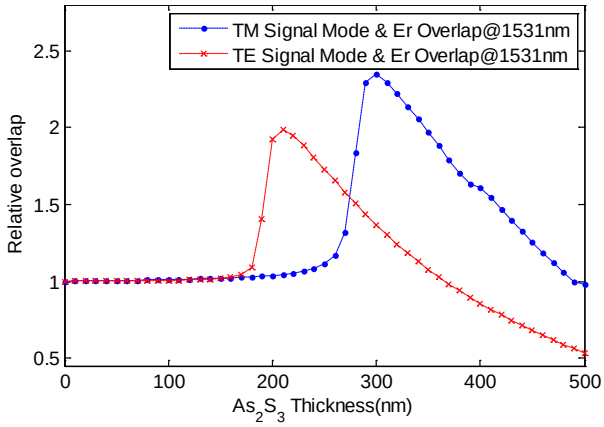

Fig. 36. Overlap data: Signal modes and Er overlap.

Ψ_s, Ψ_p, Ψ_f are the signal, pump and fiber modes. The fiber mode has a mode field diameter (MFD) of 9.9 μm at 1480 nm, measured by the beam profiler.

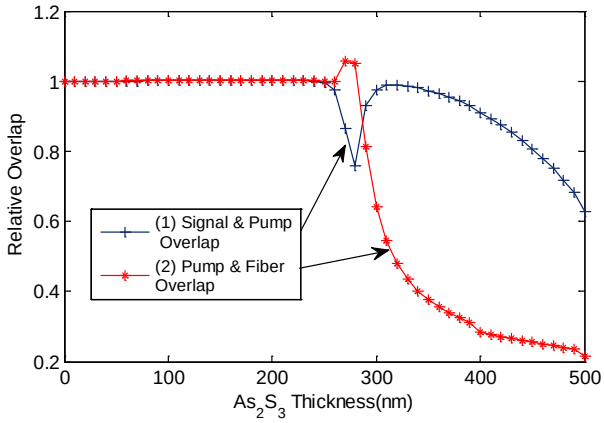

Fig. 37. Pump effects for TM mode: (1) Pump and signal mode overlap; (2) Pump and fiber modes overlap.

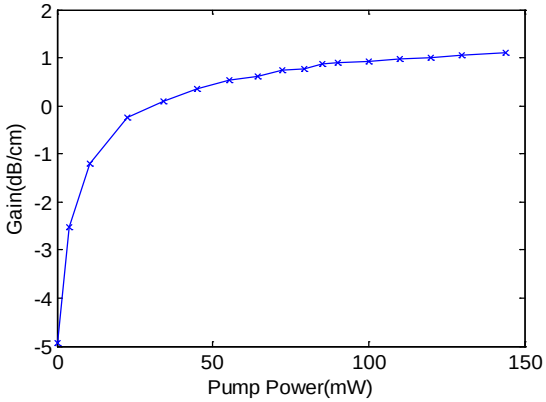

Fig. 38. Propagation gain versus pump power for Er:Ti:$LiNbO_3$ waveguide without As_2S_3 for TM mode.

Sample fabrication parameters are discussed in Chapter IV and the measurement setup is discussed in Chapter V.

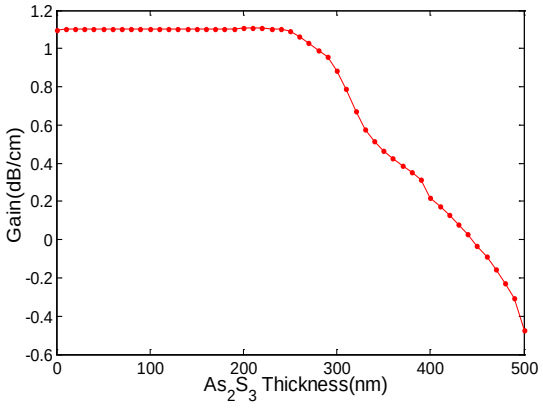

Fig. 39. Effective gain influenced by pump effects for TM mode.

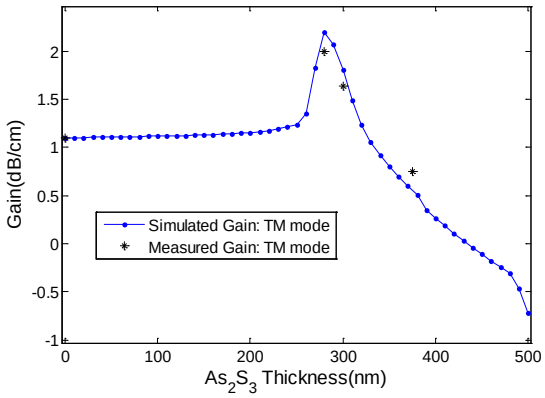

Fig. 40. Propagation gain versus As_2S_3 thickness: Comparing measured and simulated results for TM mode (peak at 280 nm).

These pump-related overlaps change the amount of pump power interacting with Er ions and the signal mode. They impact pump efficiency, and thus are similar to changing the input pump power. We multiply these two overlap values and take the product as the pump efficiency ratio. Experimentally, we measured the gain versus pump power, shown in Fig. 38, for the waveguide without As_2S_3. Therefore, the effective gain in Fig. 39 is computed from the gain versus pump power curve in Fig. 38 while the effective pump power is calculated by multiplying the pump efficiency ratio and pump power (144mW).

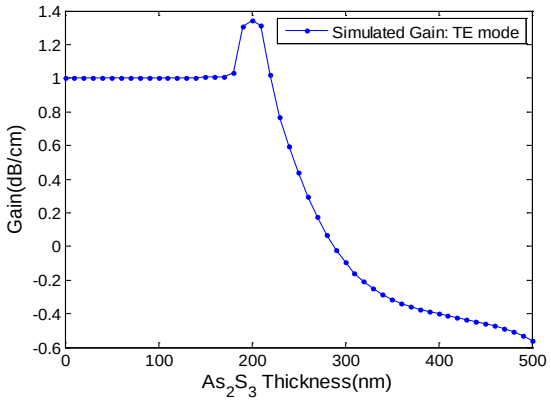

Fig. 41. Propagation gain versus As_2S_3 thickness: Simulated results for TE mode (peak at 200 nm).

Based on (7), this gain should be proportional to the signal mode and Er overlap. As shown in Fig. 40, the final simulated propagation gain versus As_2S_3 thickness is obtained as the product of the curves in Fig. 36 and Fig. 39. From Fig. 37, the optimum thickness for gain is found to be 0.28 μm, which is a -0.2 μm shift from Fig. 36 due to pump effects. Our experimental data for several As_2S_3 thicknesses is also plotted, and it matches well with the simulated curve. The same process can be performed for TE polarization and the final simulated gain is plotted in Fig. 41. The optimum thickness is 0.20 μm, which is a -0.1 μm shift from Fig. 36 due to pump effects.

Coupling losses between the mode and the fiber must be considered since the mode shape is changed. The coupling losses include Fresnel reflections, which are constant, and the mode shape mismatch, which is the overlap between the waveguide mode and fiber mode. The coupling losses of the Ti:Er:$LiNbO_3$ waveguide have been measured at 1531nm for TM mode (0.5dB) and TE mode (0.9dB).

The waveguide modes for varying As_2S_3 thicknesses have been simulated at 1531 nm for both TM and TE polarizations. The fiber mode with Gaussian distribution has a mode field diameter (MFD) of 10.2 μm at 1531 nm, measured by the beam profiler. The relative horizontal and vertical shifts between waveguide and fiber modes were scanned to achieve the best alignment. Fig. 42 shows the calculated coupling overlap data, which is normalized by the overlap without an As_2S_3 waveguide. The coupling overlap for an As_2S_3 thickness of 280 nm with TM polarization is 1.14 (+0.57 dB), normalized to the overlap with no As_2S_3, even better than the overlap without As_2S_3. This is because the TM mode for the 7 μm wide Ti: $LiNbO_3$ waveguide is larger than fiber mode, but the As_2S_3 waveguide reduces the mode size and better matches the fiber mode, reducing coupling loses.

For TE polarization at 200 nm, the normalized coupling overlap is 0.946 (-0.24 dB). It can be overcome by introducing a tapered As_2S_3 waveguide [48]. The waveguide width can increase/decrease gradually from 0.5 μm to 4 μm in 3 mm length at the input/output ports of the waveguide. So the mode profile at the waveguide ends is the same as the normal Ti:$LiNbO_3$ waveguide mode while in the center it is the pulled-up by the As_2S_3 waveguide.

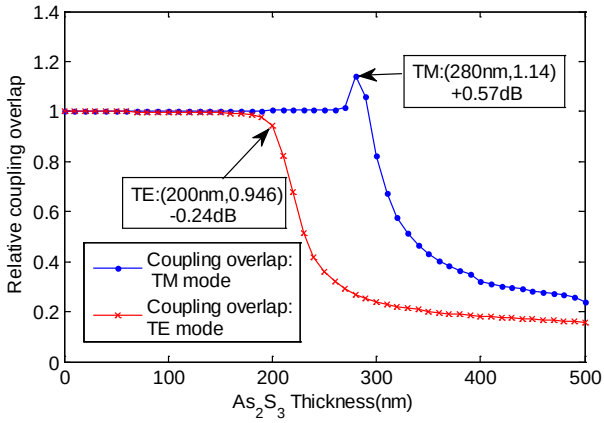

Fig. 42. Coupling overlap (coupling loss) for TM and TE modes.

3.3. Electro-optical devices

3.3.1. As_2S_3 waveguide assisted EO phase shifter

In this section, the optimum As_2S_3 overlay with varying width and height to produce the smallest required EO tuning voltage has been explored.

The EO solver in FIMMWAVE can solve the situation when the electrical field is perpendicular to the waveguide. The device is the phase shifter. The As_2S_3 waveguide is side coupled to the Ti waveguide, and thickness and width have been swept.

To determine the sweet spot of EO effect under various values of the As_2S_3 width, thickness and electrode gaps, EO effect simulations are required. To test the EO effect on the sample, the waveguide must be designed to a MZI pattern as shown in Fig. 43, the top and bottom arm are identical for titanium waveguide and electrodes. The top arm has an extra As_2S_3.

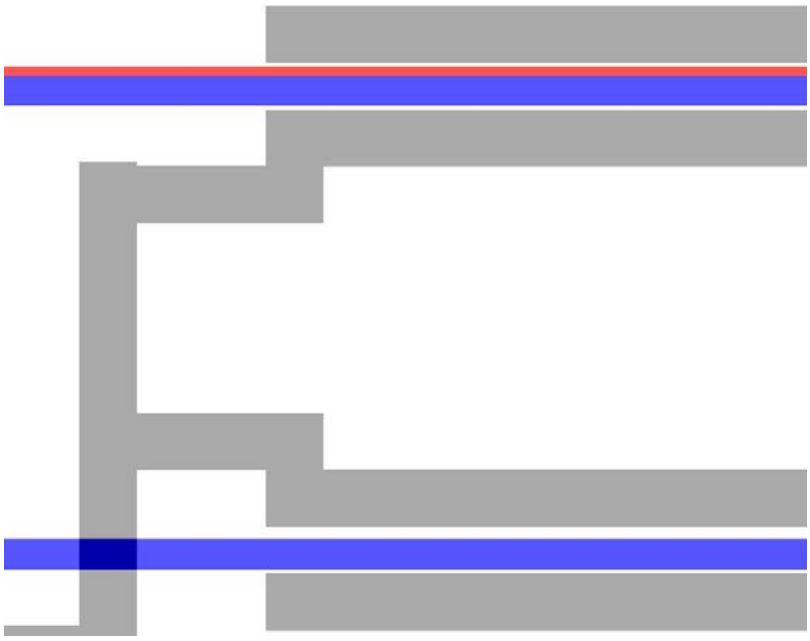

Fig. 43. MZI pattern with 1μm gap between Ti (or As_2S_3) and electrodes (The gap is the distance between Ti (or As_2S_3) and electrodes).

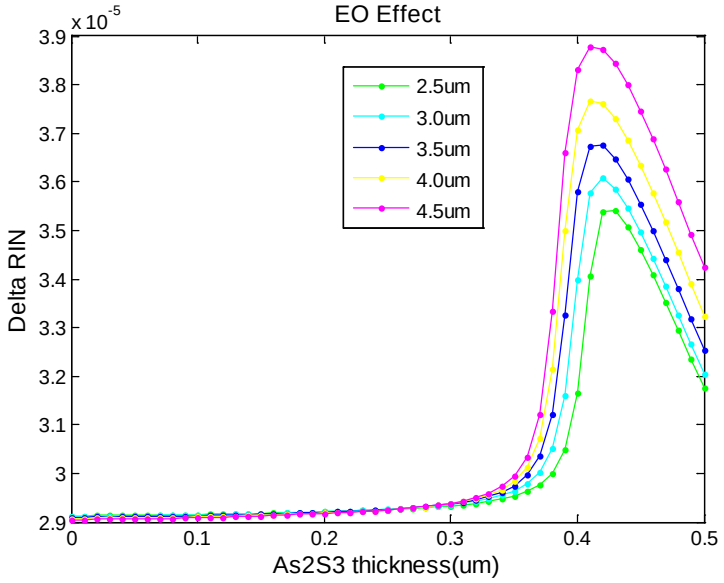

Fig. 44. EO effect simulation for TM modes.

(Electrodes gap=17 μm, As_2S_3 width are swept from 2.5~4.5 μm).

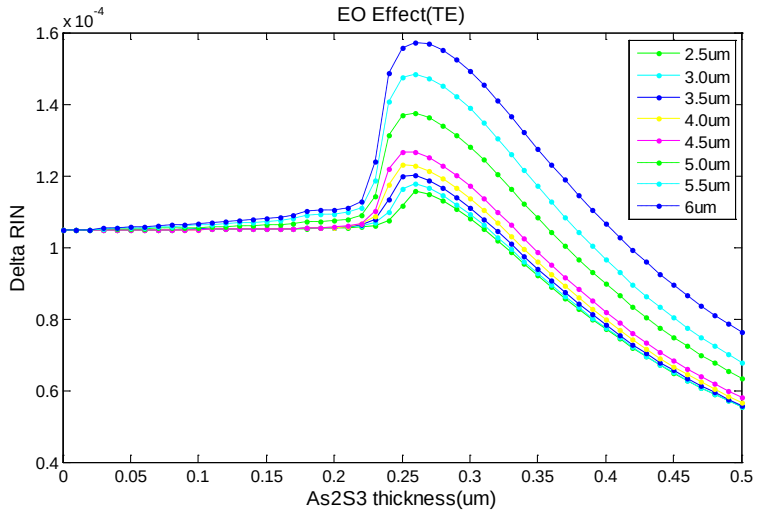

Fig. 45. EO effect simulation for TE modes.

(Electrodes gap=17 μm, As_2S_3 width are swept from 2.5~6 μm).

From Fig. 44, the best thickness for EO enhance is at 0.42 μm for TM modes, independent of As_2S_3 width. Also, for TE modes from Fig. 45, it is at 0.26 μm.

Simulations to find best electrodes position have been performed.

TM Modes: As_2S_3 thickness is 0.42μm (from Fig. 44), width is 0~5μm. V=25V.

Electrodes are attached to the edge of As_2S_3 (top) and Ti (bottom) when Gap=0 μm. The gap is the distance between As_2S_3 and electrodes. The results are in Table XVIII.

Table XVIII. EO effects for TM modes: Varying As_2S_3 width and electrodes gap

(e^{-5})	As_2S_3 width (um)	0	1	1.5	2	2.5	3	3.5	4	4.5	5
Gaps=	With As_2S_3	3.77095	3.88716	4.10105	5.34425	6.13155	6.04078	5.80826	5.559965	5.3224	5.10276
0um	No As_2S_3	3.77095	3.68684	3.63793	3.58593	3.53163	3.47564	3.41833	3.35992	3.30037	3.23914
Gaps=	With As_2S_3	3.70088	3.72848	3.89317	4.7914	5.24321	5.12513	4.93693	4.74837	4.5715	4.40668
0.5um	No As_2S_3	3.70088	3.61085	3.56057	3.50794	3.45352	3.39774	3.34078	3.28264	3.22277	3.15712
Gaps=	With As_2S_3	3.62263	3.63031	3.76431	4.48609	4.80122	4.68236	4.51878	4.35856	4.20742	4.05466
1um	No As_2S_3	3.62263	3.52878	3.47782	3.42503	3.3708	3.31535	3.325866	3.20022	3.13604	3.0401

TE Modes: As_2S_3 thickness is 0.26μm (from Fig. 45), width is 0~5μm. 25V.

Table XIX. EO effects for TE modes: Varying As_2S_3 width and electrodes gap.

(e^{-5})	As_2S_3 width (um)	0	1	1.5	2	2.5	3	3.5	4	4.5	5
Gaps= 0um	With As_2S_3	17.0154	16.7105	16.8993	19.1223	20.3321	19.7845	18.9339	18.0744	17.2704	16.5334
	No As_2S_3	17.0154	16.1571	15.7295	15.314	14.9143	14.5321	14.1672	13.8184	13.4832	13.1575
Gaps= 0.5	With As_2S_3	16.2046	15.5068	15.5452	16.8452	17.3549	16.8288	16.1675	15.5258	14.9298	14.377
um	No As_2S_3	16.2046	15.3791	14.9791	14.5838	14.2249	13.8723	13.535	13.2108	12.8956	12.5729
Gaps= 1um	With As_2S_3	15.406	14.7197	14.6867	15.58	15.8295	15.3431	14.7799	14.2409	13.7358	13.2285
	No As_2S_3	15.406	14.6261	14.2547	13.8988	13.5584	13.2325	12.9191	12.6143	12.3022	11.889

The TE simulation results are in Table XIX. From Table XVIII and Table XIX, the best As_2S_3 widths can be found at 2.5 μm for both TE and TM modes. So the best dimensions are 2.5 μm wide and 0.42 μm thick for TM mode and 2.5μm wide and 0.26μm thick for TE mode.

EO effect is proportional to the overlap of optical mode in LN and the e-field. (It is calculated in x and y direction separately in FIMMWAVE and summed up later.) So if the peak of the mode overlaps with the peak of the e-field (Fig. 46 and Fig. 47), then it is suppose to get good EO effect. As_2S_3 pulls the mode up, so if the e-field is higher there, it will increase the EO effect. But over-pulling will make the mode out of LN region and get EO effect down. Increase the width has two effects: (1) Pull the mode towards As_2S_3. (2) As_2S_3 gets wider and the mode gets closer to the electrodes. Increase the thickness has only one effect: pulling the mode toward As_2S_3.

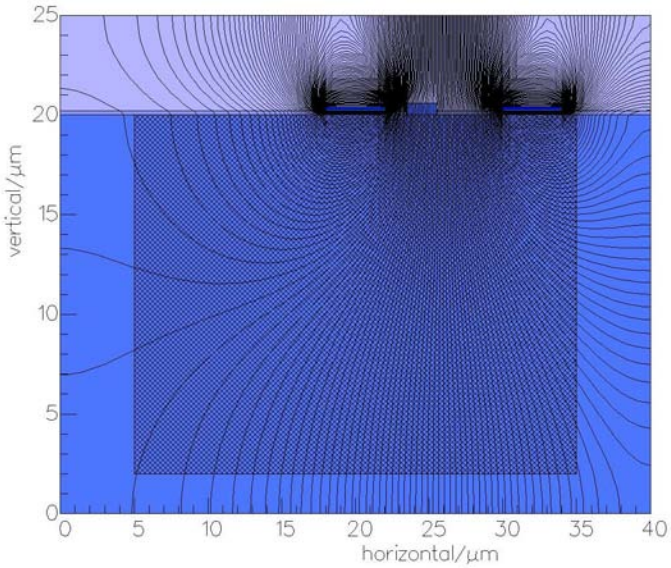

Fig. 46. Potential of the asymmetrical electrodes.

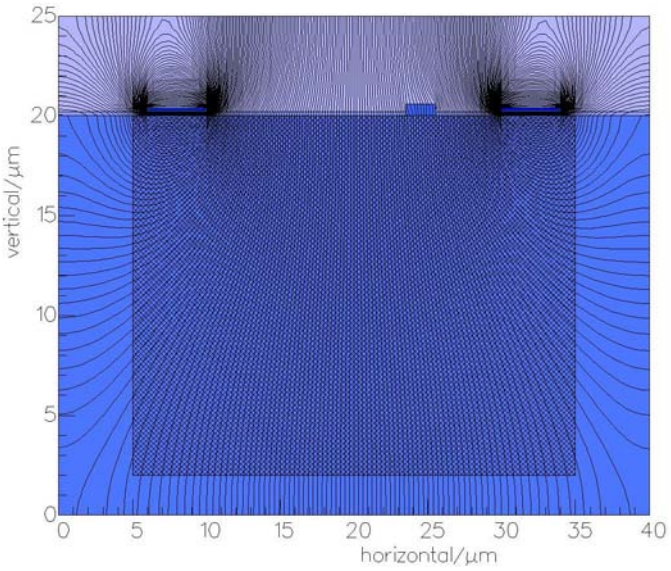

Fig. 47. Potential of the symmetrical electrodes.

3.3.2. Nano-slot EO phase shifter

Nano slot is a novel structure which brings large EO effect [49]. Simulation setup by FIMMWAVE is shown as Fig. 48. The two rectangular Si waveguides are 100nm wide and 480nm high. The slot is 15nm wide. The bottom substrate is x-cut $LiNbO_3$ and the top cladding is air.

The benefit of this structure is to use Si waveguide to confine the light inside but let LN below (when slot is filled with air) or in between (when the slot is filled with $LiNbO_3$). Since the Si is doped so it can be electrode too. Then the electrical field and optical field can be overlapped pretty well. And due to the high refractive index of Si is very high, the optical field is well confined in this small area and the optical desity is very high. All of these benefits will lead to a high electro-optical effect.

Complex FMM solver is required for this job since the Si waveguide is both optical and electrical lossy. λ is at 1550nm.

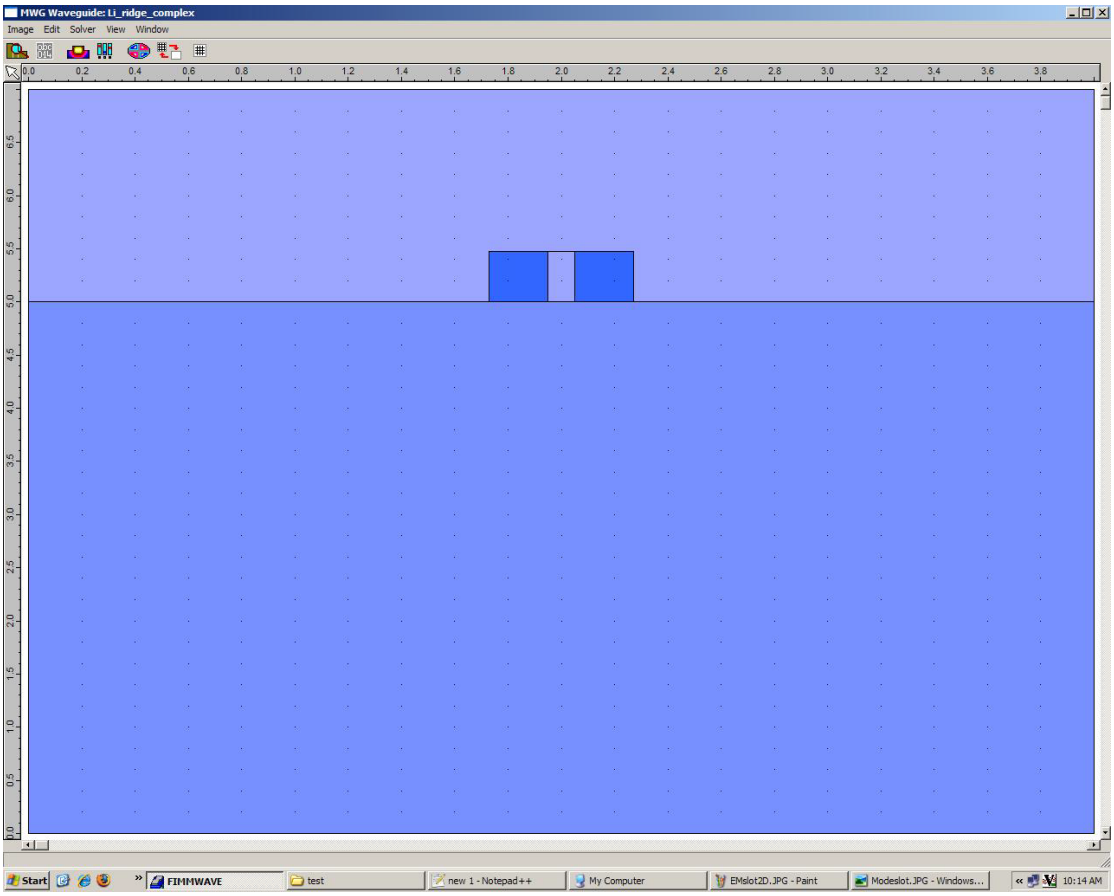

Fig. 48. EO_nano_slot FIMMWAVE setup.

After the optical mode solving, use EO solver and apply voltage on the two Si electrodes to get the electrical field distribution. The simulated results are shown in Fig. 49 for 2D electrical field and in Fig. 50 for 3D electrical field.

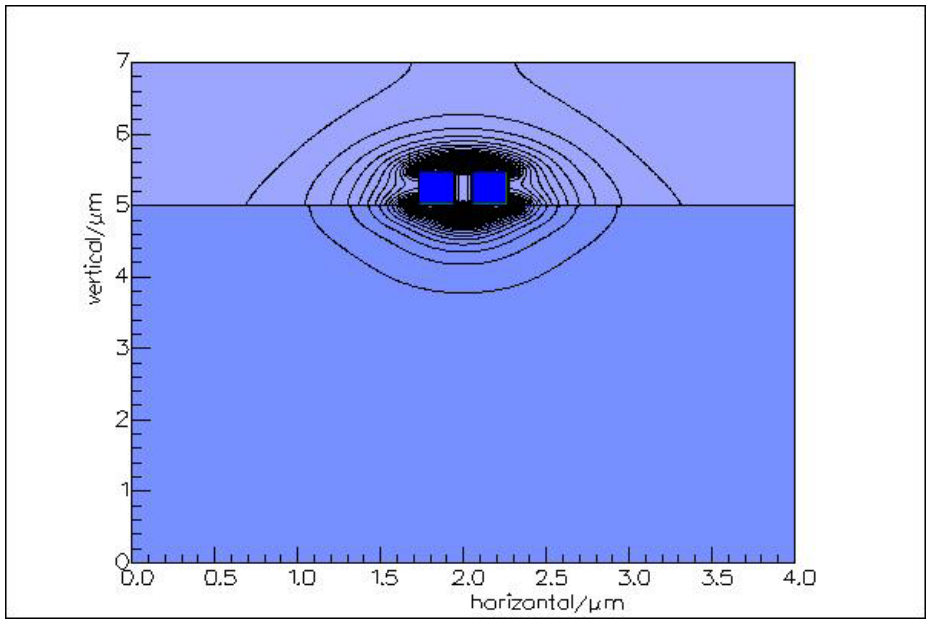

Fig. 49. 2D Ex field of nano slot from complex solver (TE mode).

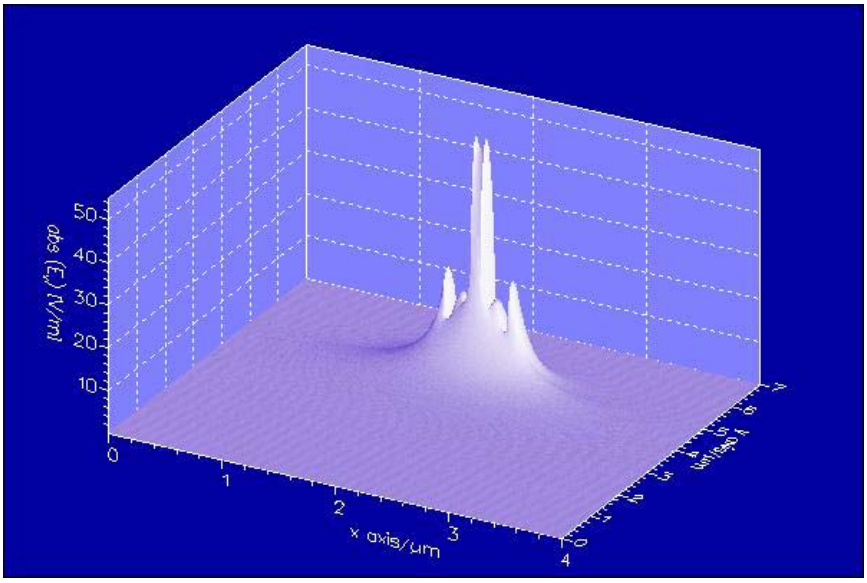

Fig. 50. 3D E_x field of nano-slot from the complex solver (TE mode).

The equations calculate the EO effect in (3.5) and (3.6) [49].

$$\Gamma = \frac{d}{V} \frac{\iint_s E_{opt}^2 E_x dxdy}{\iint_s E_{opt}^2 dxdy} \tag{3.5}$$

where d is the width of the slot, V is the voltage. E_{opt} is the optical field, E_x is the electrical field (in this situation, E field is x- component).

$$V_\pi L = \frac{\lambda}{n^3 r_{33}} \frac{d}{\Gamma} \tag{3.6}$$

After the mode and electrical field solving, load these two profiles into matlab and do the calculation in (3.5) which is the equation calculates the overlap of the electrical field and the optical field. It is similar to overlap between Mode and Er profile. V_π then can be calculated in (3.6).

Window size also needs to be appropriate. When window size: 4 μm*7 μm, resolution 500*500, the results are shown in Table XX.

Table XX. EO results when window size= 4 μm*7 μm, slot filled with air.

	FIMMWAVE	RSOFT [49]
Γ	0.0848	0.062
$V_\pi L$ (V.cm)	0.60	0.82

Then shrink window size to 2 μm*3 μm, resolution 500*500. The slot area is 100nm*480nm (25*120 points). Relative error=2/25=8%.

(1).Nano slot filled with air:

Table XXI. EO results when window size= 2 μm*3 μm, slot filled with air.

	FIMMWAVE	RSOFT [49]
Γ	0.0624	0.062
$V_\pi L$ (V.cm)	0.8147	0.82

(2).Slot filled with LN:

Table XXII. EO results when window size= 2 μm*3 μm, slot filled with $LiNbO_3$.

	FIMMWAVE	RSOFT [49]
Γ	0.3251	0.252
$V_\pi L$ (V.cm)	0.1564	0.2

After shirking window size and using complex solver, the simulated results by FIMMWAVE are very close to the data in [49] in Table XXI and Table XXII. Since these simulation results are repeatable, we can use this method to simulate other structures and consider the loss in the same time to optimize the modulator design.

3.4. Multilayer and Bragg reflectors

3.4.1. Multilayer reflectors

The high, low and substrate index are 2.4, 1.45 and 2.1 respectively for As_2S_3, SiO_2 and LiNbO3 (n_o). The simulations are based on the multilayer equations in Chapter II.

(a) Reflectance change with high & low index pairs

Fig. 51 shows the intensity reflectance and phase reflectance at center wavelength change with the number of high, low index pairs.

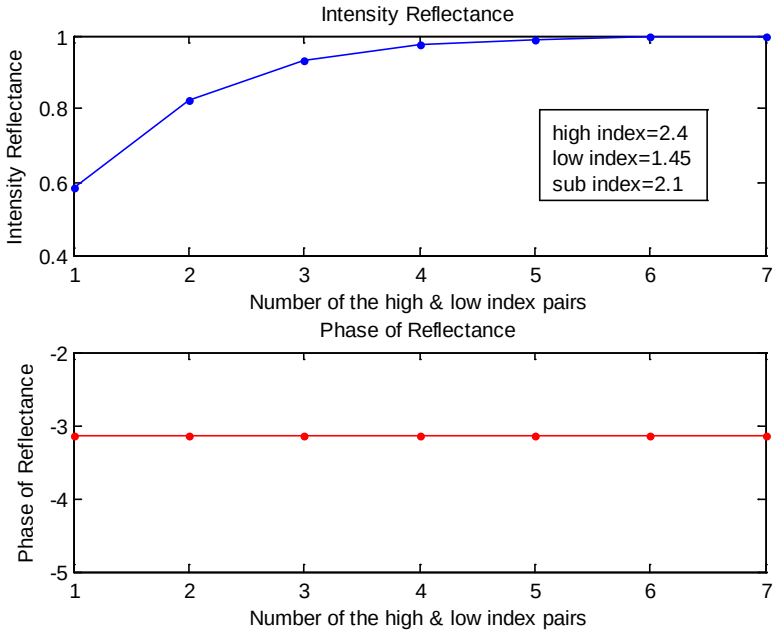

Fig. 51. Intensity and phase reflectance at center wavelength (1531nm).

(b) Reflectance change with wavelength

The Fig. 52 and Fig. 53 showed the reflectance change with wavelength. Refractive Indices are constants with wavelength change.

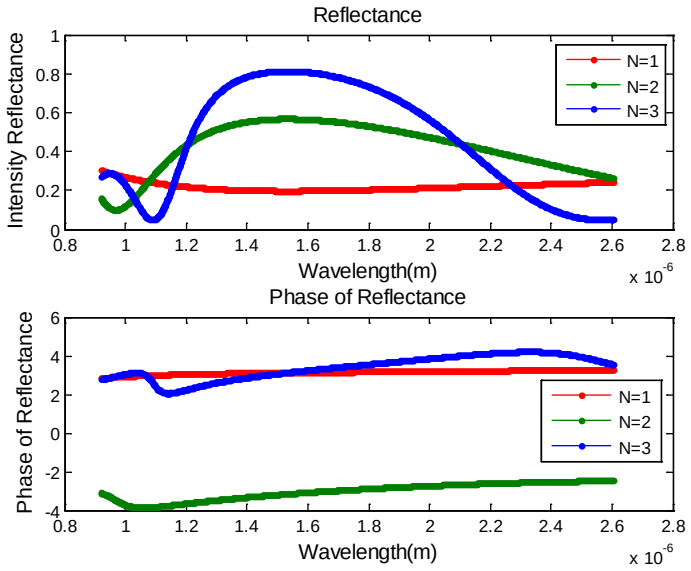

Fig. 52. Reflectance when number of the high & low pairs N=1,2,3.

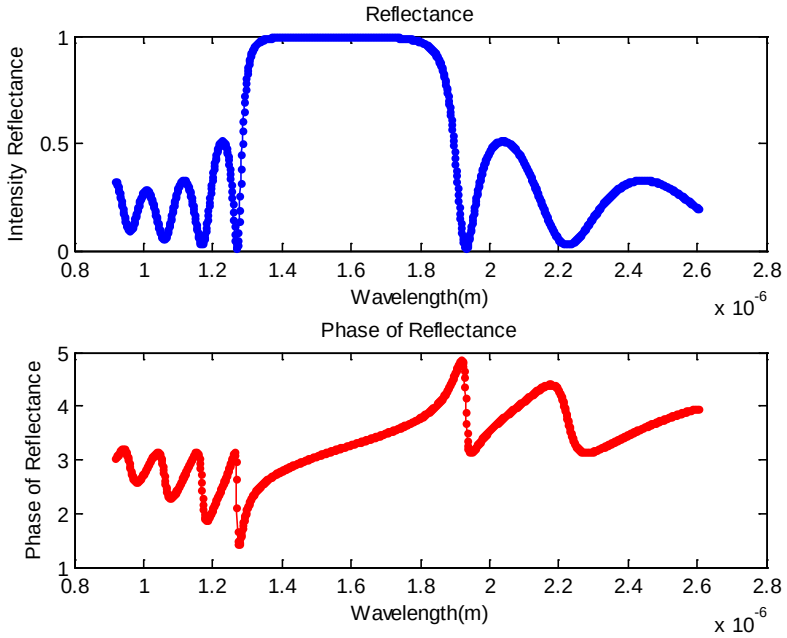

Fig. 53. Reflectance when number of the high & low pairs N=7.

3.4.2. Bragg grating reflectors

We want to simulate the reflection spectrum of the Bragg gratings and design it to fulfill our requirements for partial reflector: reflection peak at 1531nm at reflection zone width about 10nm. The reflectivity can be adjusted by changing the length of the grating.

(a) Si overlay simulation

Bragg gratings in Fig. 54 have been achieved by Si etch on Ti:$LiNbO_3$ [50].

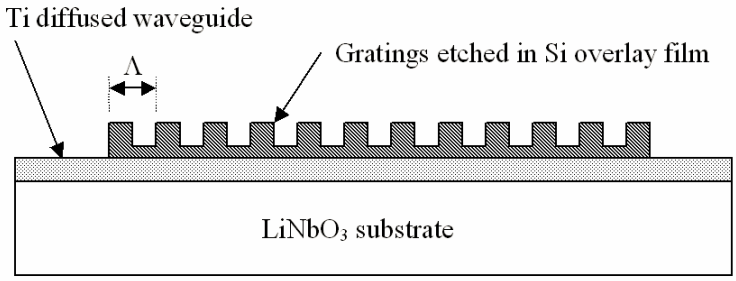

Fig. 54. Schematic illustration of the waveguide with Bragg gratings.

The parameters are listed in Table XXIII and the reflection spectrum is shown in Fig. 55.

Table XXIII. Parameters of Bragg grating (TE polarization, *thickness: etched).

film	Λ	Thickness*	length	Etch gas	Wavelength	Bandwidth
Si-a	350nm	10/105nm	2 mm	C4F8/O2	1542.7	0.05nm

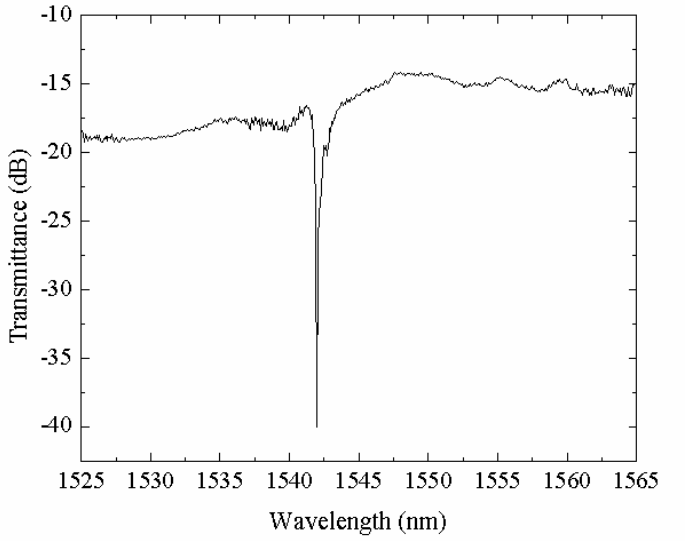

Fig. 55. Broadband transmittance spectrum for TE input polarization [50].

The simulation was performed by FIMMProp, and the simulation setting is shown below. The substrate is 7 μm wide Ti:$LiNbO_3$ with 95nm titanium diffused by 9hours. The number of high/low pairs (periods) is $N=10^6$.

The high refractive index sections have 1nm Si overlay on top. The simulated effective index n1=2.140993166, length L1=1.531/4/n1. The low refractive index sections have no Si overlay on top. The simulated effective index n2=2.140991681, length L2=1.531/4/n2;

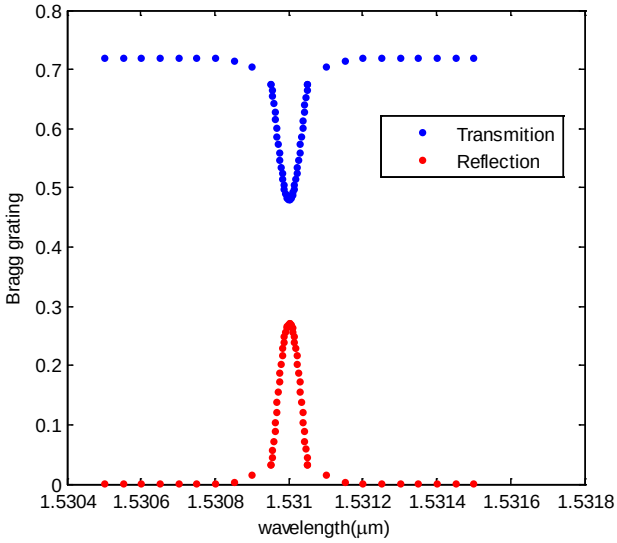

Fig. 56. Transmittance and reflectance simulation for Si overlay Bragg grating (TE mode, 10e6 periods).

The simulated transmition and relfection spectrum is shsow in Fig. 56. The center wavelength is exactly at 1531nm. We can see that even the number of the periods reaches up to 10^6, the reflection was still very low <0.3.

(b) As_2S_3 waveguide simulation

First design (in Fig. 57) is two-section design.

The simulation setup and result are listed below. The substrate is x-cut LN, no Ti diffused WG for faster simulation. TM modes were simulated. The high refractive index sections of As_2S_3 WG have thickness 0.47 μm, width 3.5 μm, index n1=2.22806000; Low refractive index sections have As_2S_3 WG thickness 0.47 μm, width 2.7 μm, index n2=2.223421981. Both high and low index sections keep single mode. The average index (n1+n2)/2=2.2257409905. The lengths of every section are calculated as taking

average of the high and low refractive index: L1=L2=1.531/4/[(n1+n2)/2]=0.1720 μm. The L_{period}=L1+L2=0.3439 μm. The number of periods N=5000 and the length of grating=1.72 mm

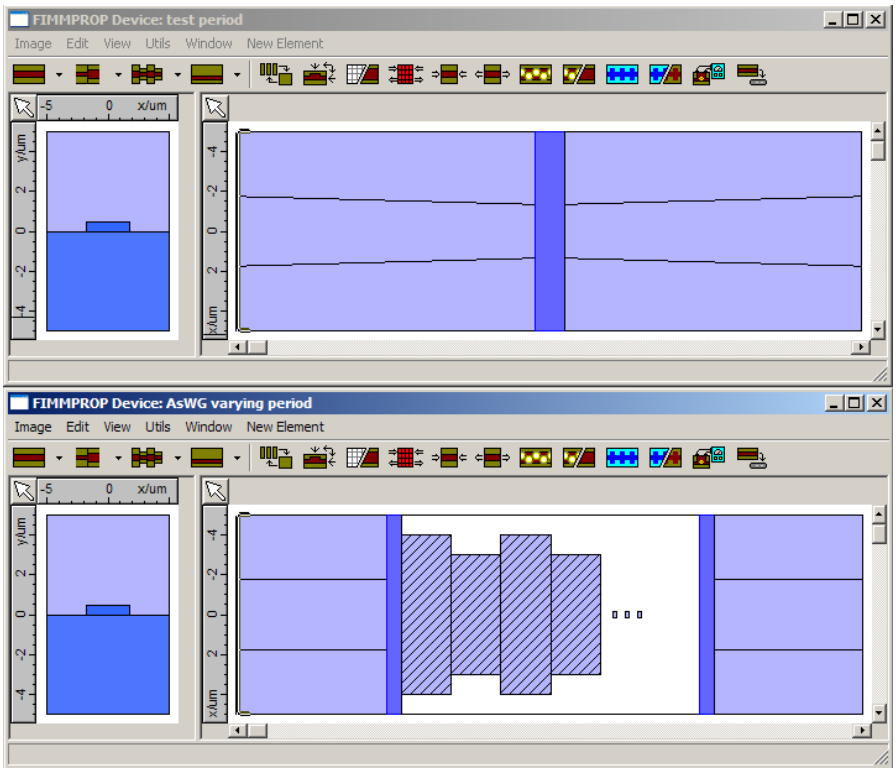

Fig. 57. Taper teeth structure FimmProp simulation setup.

Since the reflection depends on the refractive index difference, we have to make width difference big enough: (3.5-2.7=0.8 μm). Fig. 58 shows the reflection and transmission spectrum. It fulfilled our requirements.

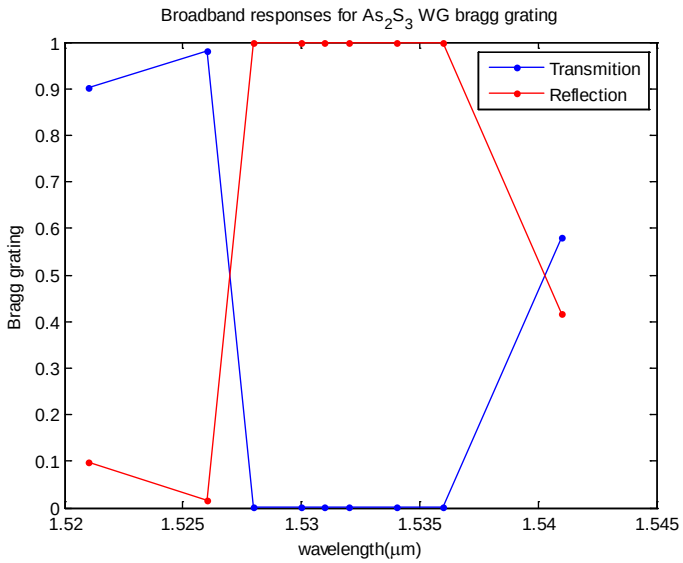

Fig. 58. Broadband transmittance and reflection simulation for As_2S_3 WG Bragg grating (TM mode, 5000 periods, length=1.72 mm).

In the first design, although it can work on simulation, but the “tooth tips” are too sharp for the real fabrication. Then the second design which is the four-section design which changes the teeth of the grating from the triangular shape into the trapezium shape. The real fabrication is based on this design and the etched As_2S_3 patterns are shown in Chapter V.

Second design is shown in Fig. 59, Fig. 60, Fig. 61 and the parameters are listed below.

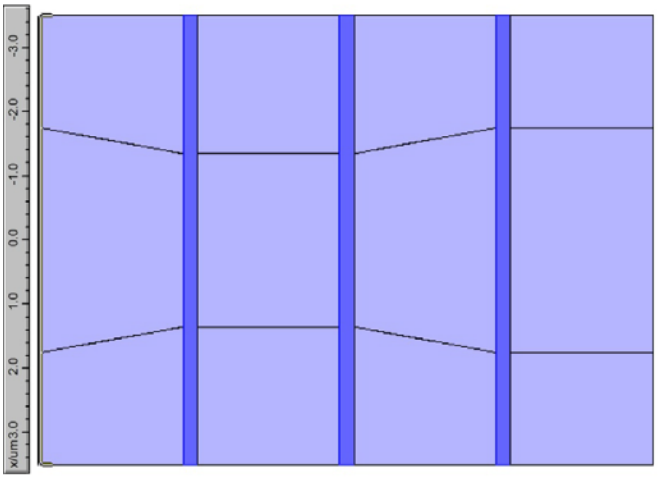

Fig. 59. Single unit period of the four-section design of Bragg grating.

For As_2S_3 on Ti:$LiNbO_3$ structure, wl=wavelength=1.531nm, width1=3.5 μm; width2=2.7 μm. The simulated refractive index data is listed: n1=2.232942088, n2=2.231268554, n3=(n1+n2)/2=2.232105321,n4=(n1+n2)/2=2.232105321. The lengths for every section are calculated:

L1=wl/8/n3=0.085737441777282 μm ;

L2=wl/8/n2=0.085769594904621 μm;

L3=wl/8/n3=0.085737441777282 μm;

L4=wl/8/n1=0.085705312747905 μm;

The length of one period is L0=L1+L2+L3+L4=0.342949791207091 μm. The full length for the gating area is L_full=L0*5000=1714.748956035456 μm. The taper length is L_taper=500 μm. The taper tip length L_end=1 (required in FIMM Prop). The

whole length of this structure is L=L_end*2+L_taper*2+L0*5000=2716.748956035456 μm.

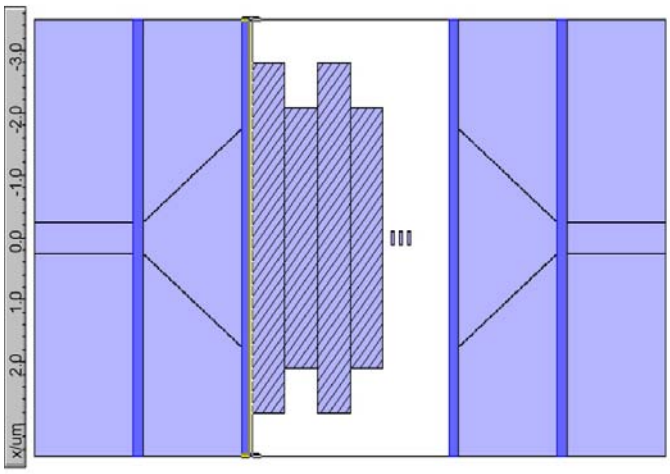

Fig. 60. Whole length of the four-section design of Bragg grating.

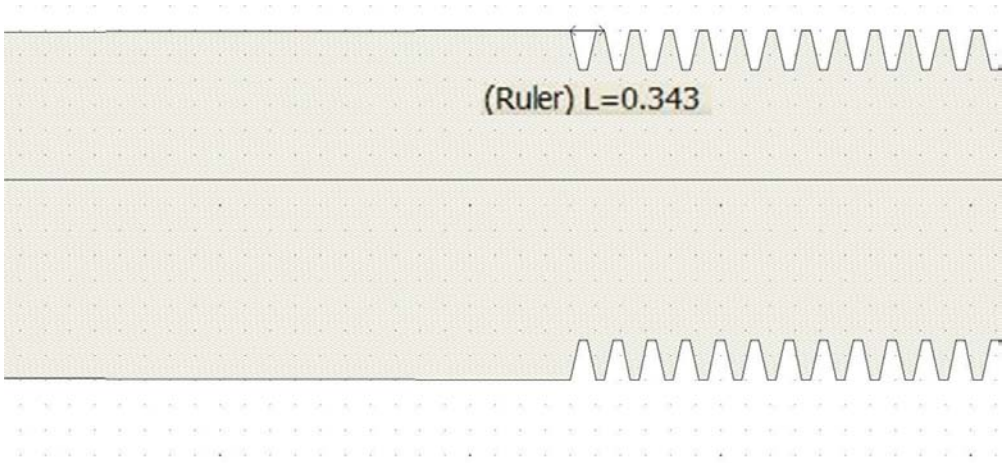

Fig. 61. Generated GDS file of the Bragg grating. (Taper + teeth).

CHAPTER IV

FABRICATION AND PROCESS DEVELOPMENT*

4.1. As_2S_3 waveguide assisted Er: Ti: $LiNbO_3$

A 13 nm-thick Er layer was sputtered onto a 3cm long x-cut, y-propagating $LiNbO_3$ substrate and diffused at 1100°C for 120 hours. The resulting Er profile measured by Secondary Ion Mass Spectrometry (SIMS) is shown in Fig. 62. Then, a 95 nm titanium film was sputtered, patterned, and diffused for 9.5 hr in wet breathing air ambient. The end facets of the waveguide chip were then polished to optical quality, and the Er:Ti:$LiNbO_3$ waveguide tested by butt-coupling single-mode fibers. The mode profiles were shown in Fig. 35. The mode field diameter (MFD) is defined as the full width at 1/e2 for mode intensity profile. They are measured for TM mode (vertical: 10.7 μm, horizontal: 13.9 μm) and TE mode (vertical: 5.6 μm, horizontal: 8.6 μm). After that, a thin film of As_2S_3 (refractive index: 2.4) was deposited using RF magnetron sputtering at varying thicknesses (0 nm, 280 nm, 300 nm and 375 nm) with a constant 4 μm width. The top view in Fig. 63 shows that the As_2S_3 waveguide is placed next to the bump of the titanium diffused waveguide, so as to keep the As_2S_3 waveguide away from the rough surface of the bump.

---

* Part of this chapter is reprinted with permission from "Gain improvement of Er-Ti:LiNbO3 waveguide amplifier by an As2S3 overlay waveguide" by Xiaomin Song, Wee Chong Tan, William Timothy Snider, Xin Xia, and Christi K. Madsen, IEEE Photon. J., 3, 686-695, 2011, copyright 2011 by IEEE.

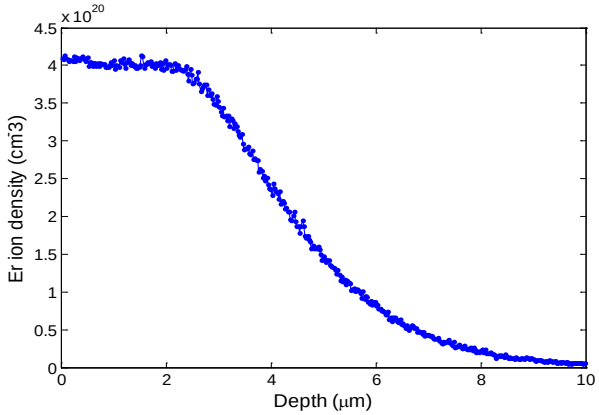

Fig. 62. The Er concentration profile measured by Secondary Ion Mass Spectrometry (SIMS)

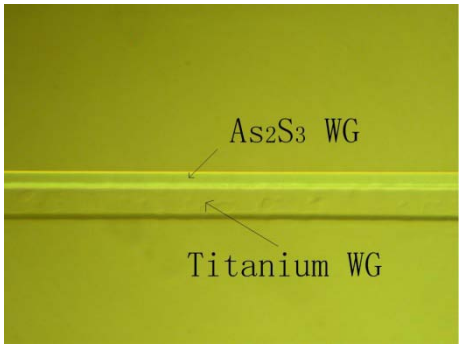

Fig. 63. Top-view photomicrograph of Ti:$LiNbO_3$ and As_2S_3 waveguides.

4.2. As_2S_3 ring on Er: Ti: $LiNbO_3$

4.2.1. Image reversal

The recipe in Fig. 64 and Table XXIV was tested for best performance.

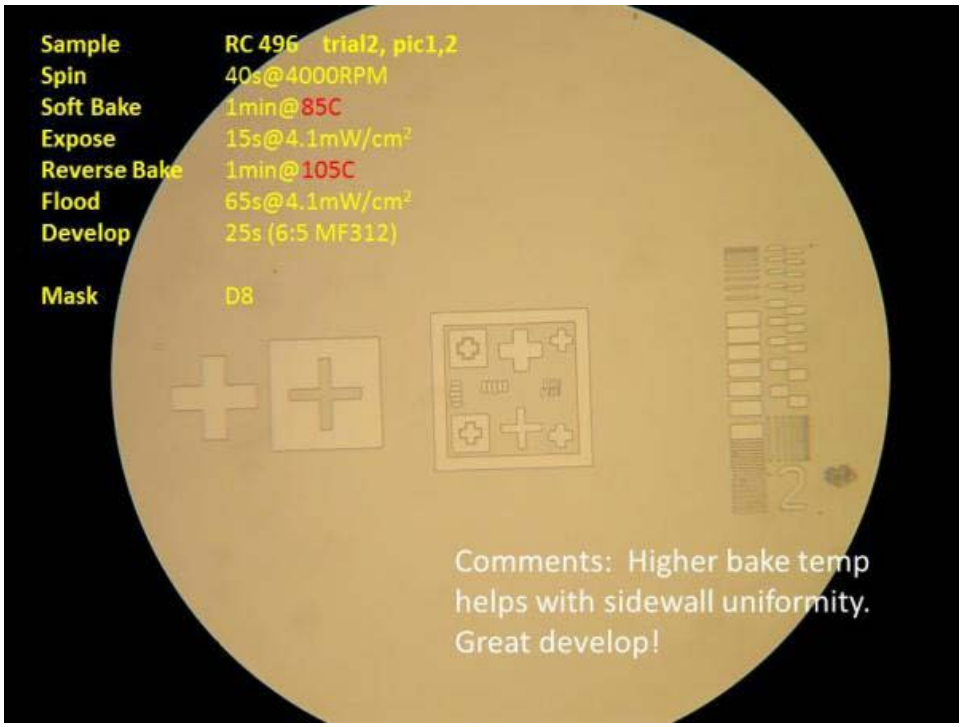

Fig. 64. Photograph of an ideal development. (Alignment markers have square corners and have are completely clear in intended regions.)

Table XXIV. Image reversal recipe.

Sample	Spin	Soft Bake	Expose	Reverse Bake	Flood	Develop	Mask
RC 496 trial2, pic3	40s@4000RPM	1min@85C	15s@4.1mW/cm^2	1min@105C	65s@4.1mW/cm^2	25s (6:5 MF312)	D8

4.2.2. Lift-off

After image reversal or negative patterning, here comes the lift-off process.

It is 3 min in acetone then put the beaker into ultrasonic until Er layer totally lifted off (about 2-3min).

During the ultrasonic lift-off process, I used two sharp-end tweezers to hold the samples (Fig. 65). This made the samples face down and avoid the re-deposition of the Erbium (or other film) pieces.

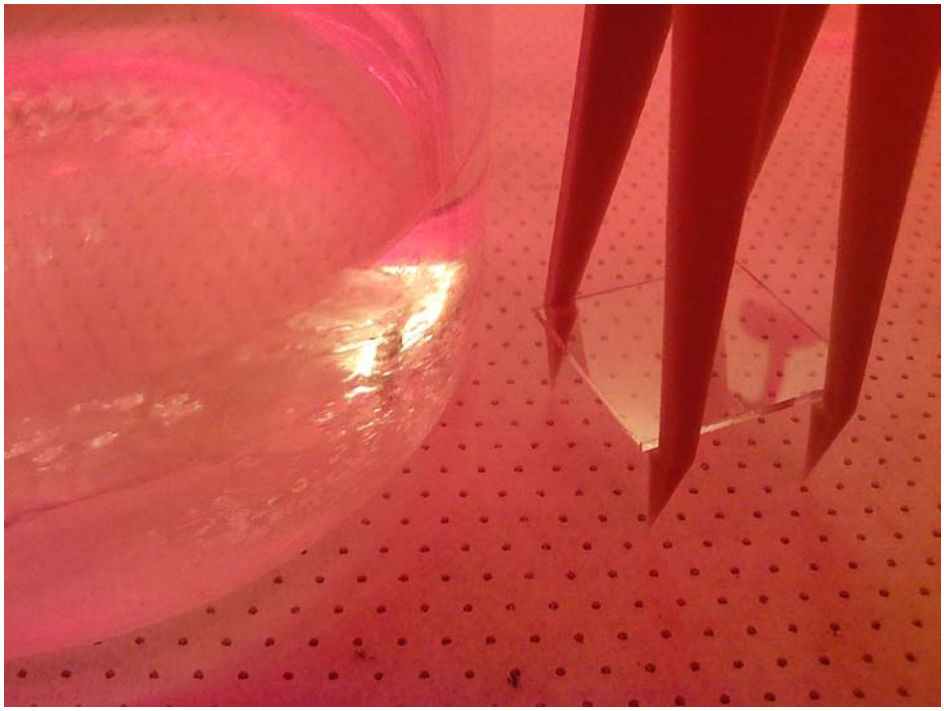

Fig. 65. Samples were set face down during the lift-off.

4.3. Er doped Ti: $LiNbO_3$ cavity

4.3.1. Multilayer deposition

Multilayer films have been deposited on the polished sides of the $LiNbO_3$ samples. As_2S_3 and SiO_2 stacks are shown in Fig. 66. It has three As_2S_3 and two SiO_2 layers. The intensity reflectivity is 0.8233 theoretically.

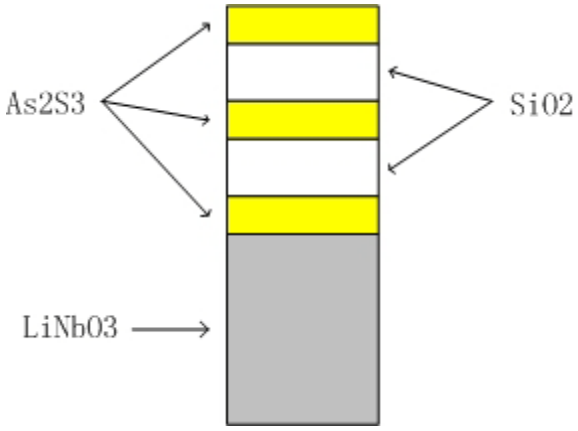

Fig. 66. Multilayer films.

Table XXV. Multilayer index and thicknesses.

λ=1531nm	As_2S_3	SiO_2
Refractive Index: n	2.438	1.444
Thickness(nm)	156.99	265.06

The thicknesses for every layer have been calculated: $thickness = \frac{\lambda}{4n}$ in Table XXV. The films are deposited on the right edges of the samples as Fig. 67 shows.

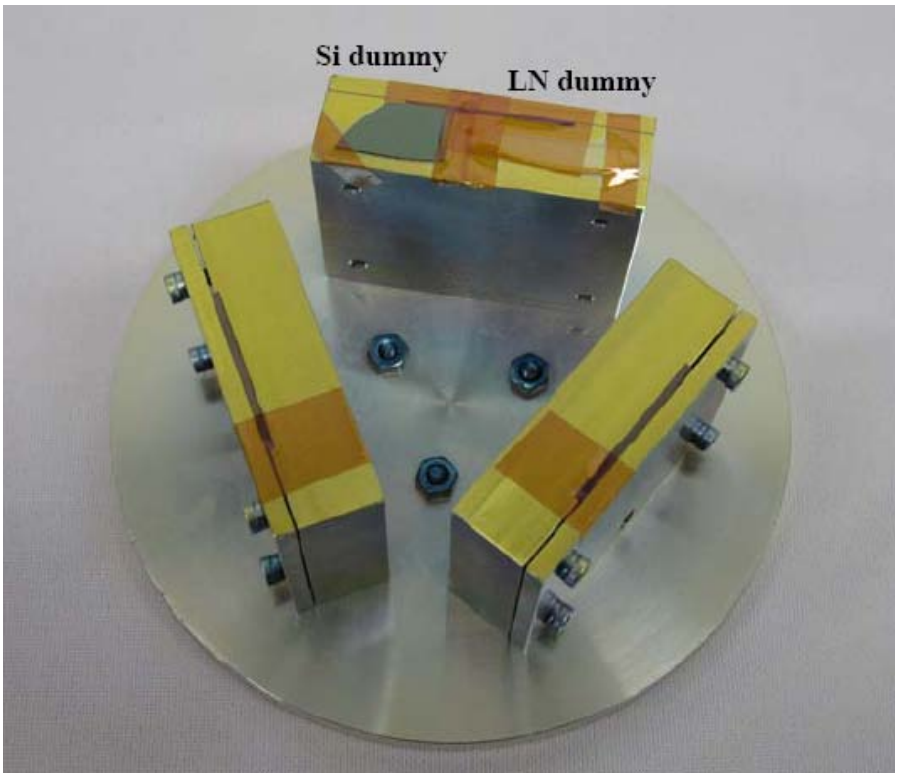

Fig. 67. AJA facet deposition mount.

4.3.2. E-beam lithography for Bragg grating

UT AustinE-beam lithography training; Process:

a) Loading wafers (+pumping).
b) Transfer of wafers;
c) Calibration and exposure;

The sample loading was done in room 1 (Fig. 68). Then transferring wafers and exposure were done in room 2 (Fig. 69). The sample loading should be very careful or the load lock could be damaged (Fig. 70). Transferring wafer should be done when the lights in Fig. 71 are all green. Then the calibration and exposure could be done by following the lab manuals.

Fig. 68. E-gun chamber in room 1 (with load lock)

Fig. 69. Main console in room 2.

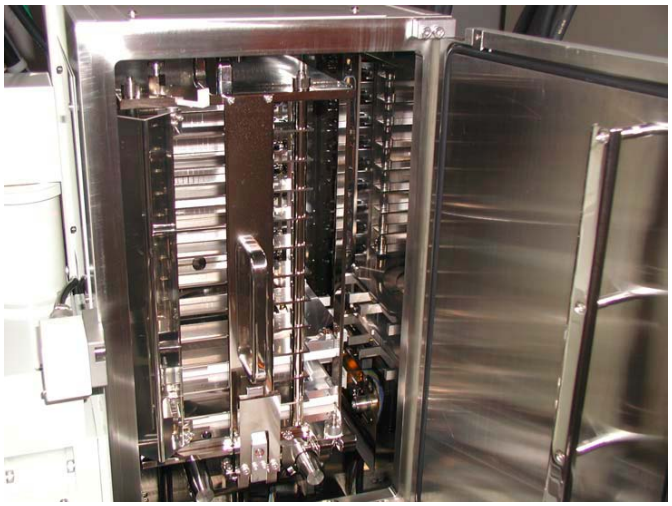

Fig. 70. Cassette holder lock.

Fig. 71. Auto loader (wafer transfer) control.

The whole processes of making As_2S_3 Bragg gratings include: E-beam lithography, RIE etch, O2 ashing, HF.

Recipes:

(a) E-beam lithography

(1) **Positive** Resist: **ZEP 520A**

Spin parameter: 500rpm 5sec 100rpm ramp； 6000rpm 35sec 1000 ramp.

(P.R thickness 350nm)

Soft (pre) bake: 150 ^{o}C hotplate 2.5min (was 180 ^{o}C, too high for As_2S_3)

Exposure time: about 20 sec for area 3.5×344 μm^2.

Dose (Unit: uC/cm^2): 117, 108, 99, 90, 81.

Develop: Amyl Acetate Developer, 1’30” develop, 1’ rinse in IPA.

(2) **Negative** resist: **NEB 31A3**

Spin parameter: 500rpm 5sec 100rpm ramp; 3000rpm 60sec 1000 ramp.

Soft (pre) bake: 110 ^{o}C hotplate 2min.

Exposure time: about 3 sec for area 3.5×344 μm^2.

Dose (Unit: uC/cm^2): 14, 13, 12, 11, 10

Reverse bake: 95 ^{o}C hotplate 45sec (critical).

Develop: AZ 300 MIF, 30 sec.

(Photo resist remover: Remover PG: N. Methypyrrolidinone (NMP). It can be replaced by RIE O_2 ashing.)

(b) RIE

Same recipe as Ti/ As_2S_3 etching.

RC620, NEB: 3’30”+30” +30” +30”. Stop until yellow color gone (Fig. 72).

RC607, ZEP: 4’30”. Photo-resist gone, surface looks like titanium film (Fig. 73).

Fig. 72. RC620, NEB 3’30” in the etching process.

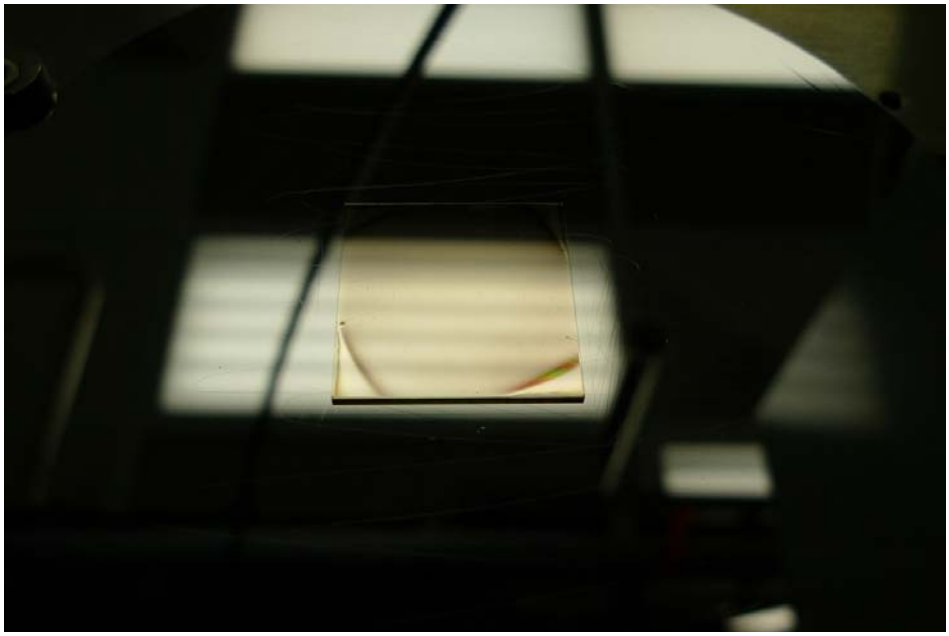

Fig. 73. RC607, ZEP: after 4’30” RIE etching.

(c) O_2 ashing

It is the same recipe as As_2S_3 O_2 ashing.

RC 607, ZEP: 2’20”. No change (Photo resist was gone already)

RC620, NEB: 2’20”+8’20”+30”, until the surface of the As_2S_3 strip looks smooth.

(d) HF

RC607 and RC620: 1min in diluted HF (HF:H2O =1:20).

Then the samples are ready for optical testing or SEM imaging. The SEM pictures of Bragg gratings are shown in Chpater V.

After E-beam E-beam lithography recipe discussion, the E-beam pattern design for cavities can be performed. Top and left boundaries need rough polishing (1st pad) before photolithography to get better control of the positions of the align marks. Also it may require marks for the positions of the tapes.

E-beam advantage: “Self alignment”, using one-time patterning to make W align-mark (Fig. 74) and Ti (Or P.E.) waveguides (WGs) which needs Teflon tape to do selective deposition (Fig. 75).

E-beam As_2S_3 ring can be designed for both TE and TM modes, tip width can be narrower (~0.5 μm) for TE mode. Proton exchange and Ti patterns are both designed.

Calibration for the Tungsten etch rate and comparison to the Ti and SiO_2 etch rate: W etch, 3’30” for 1500 Å; Ti etch: 4’ for 950Å. Tungsten area can be over etched because it doesn’t need high quality waveguide. So the final W thickness is about 2000Å along with 950Å titanium.

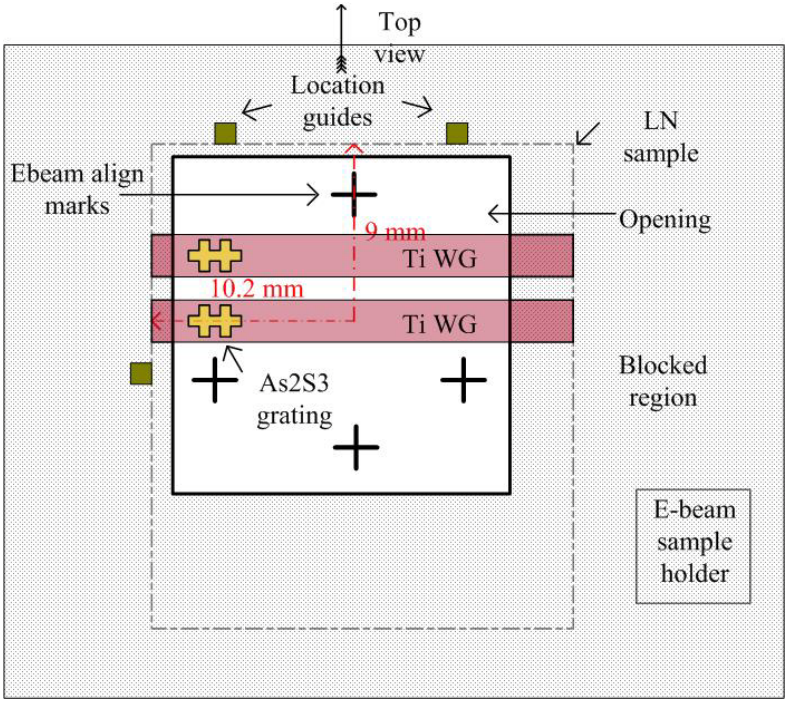

Fig. 74. Design diagram of As_2S_3 grating by E-beam lithography.

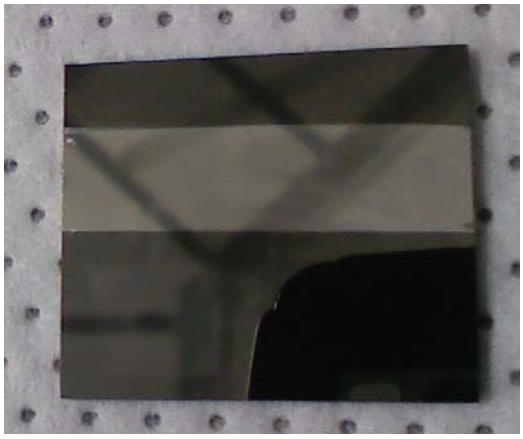

Fig. 75. Selective deposited sample. Top and bottom areas are tungsten, central area is titanium.

CHAPTER V

MEASUREMENT AND RESULTS*

5.1. As_2S_3 waveguide assisted Er: Ti: $LiNbO_3$

A schematic of the measurement setup for the optical gain is detailed in Fig. 76. We use the LUNA optical vector analyzer (OVA) which has a built-in wavelength swept source (left port) and detector (right port). It can scan the loss (or gain) of the device under test (DUT) over a wavelength range 1520-1608 nm for both TM and TE polarizations.

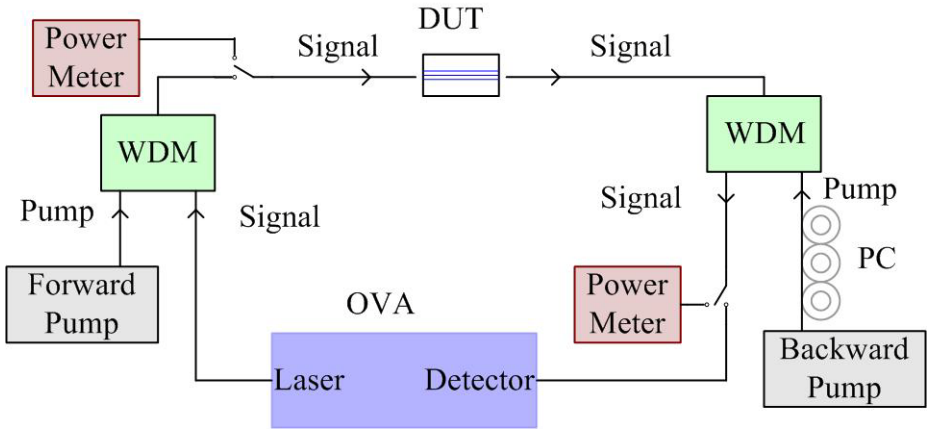

Fig. 76. Schematic of the propagation gain measurement.

* Part of this chapter is reprinted with permission from "Gain improvement of Er-Ti:LiNbO3 waveguide amplifier by an As2S3 overlay waveguide" by Xiaomin Song, Wee Chong Tan, William Timothy Snider, Xin Xia, and Christi K. Madsen, IEEE Photon. J., 3, 686-695, 2011, copyright 2011 by IEEE.

The forward pump laser power is 59mW and the backward pump laser power is 85mW before being launched into the waveguide and the pump wavelength is 1480 nm. The backward pump was TM polarized to increase the overlap with the signal mode. Signal and pump are combined by two WDM couplers. Two power meters are used to separately optimize fiber-to-device alignment and pump polarization.

There is only a small difference for measured insertion losses with the pump on and off for wavelengths longer than 1590 nm. Thus, the pump has little effect for this wavelength range, and we use the average value for the pump on and off conditions as the absolute reference for the propagation gain calculation. Note, our Ti:$LiNbO_3$ waveguide loss has negligible wavelength dependence (~0.1 dB variation over 1520-1605 nm). The propagation gain is extracted directly from the spectral data of the waveguide itself, avoiding uncertainties in estimating the fiber-to-waveguide coupling loss in the gain calculation.

First, we measured the Er:Ti:$LiNbO_3$ waveguide without an As_2S_3 layer. Then, we fabricated an As_2S_3 waveguide on top. The best gain was found with an As_2S_3 thickness of 280 nm (see Fig. 40). The propagation gain was enhanced by 0.9 dB/cm from 1.1 to 2 dB/cm (see Fig. 77). The peak amplification wavelength is at 1531 nm. Compared to the case without the As_2S_3 waveguide, the propagation gain in the Er:Ti:$LiNbO_3$ waveguide with the As_2S_3 waveguide has been improved substantially for the same launched pump power conditions, as predicted by simulation. Taking into account propagation loss (0.4dB/cm for TM mode) and coupling losses, the net gain for this 3cm long sample has been improved from 1.1dB to 3.5dB.

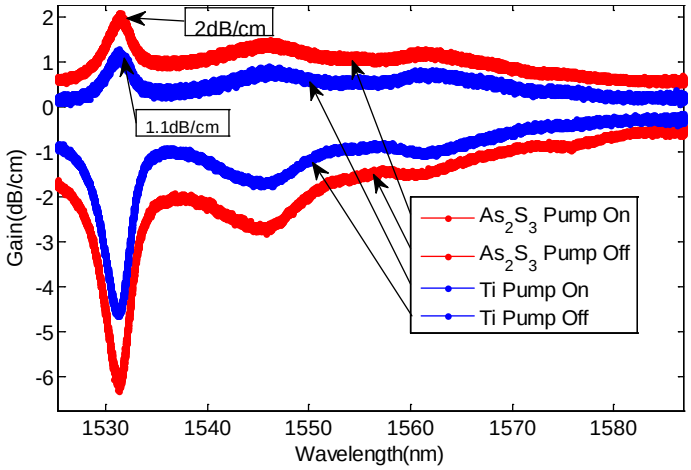

Fig. 77. Propagation gain spectrum with and without As_2S_3 on $LiNbO_3$ for TM mode (As_2S_3 thickness=280 nm).

Our approach provides the opportunity for enhanced device functionality. As one example, the As_2S_3 channel waveguides can become part of a vertically-integrated ring resonator, enabling the signal to be amplified and potentially compensate the ring's roundtrip loss. Thus, ideal all pass filters may be realized in the future as well as hi-Q, gain-tuned rings.

5.2. As_2S_3 ring on Er: Ti: $LiNbO_3$

We did our first test sample to see if the gain in the feedback loop can compensate the roundtrip loss. The mask design is shown in Fig. 78. The blue straight line is Ti:$LiNbO_3$; the pink racetrack is As_2S_3 ring and the green area is the Er doped region. We used selective doped Er because we don't want to induce excess loss in the ring where has no pump power since un-pumped Erbium ion can absorb signal power.

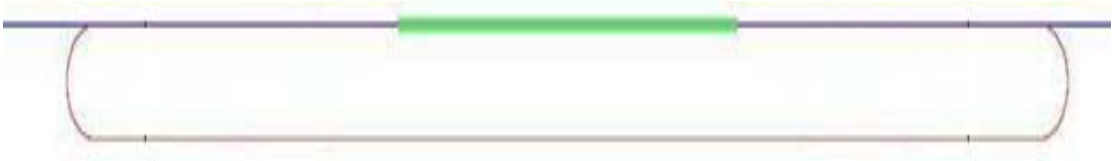

Fig. 78. Erbium area, As_2S_3 ring and titanium WG on the mask design.

Table XXVI. Er ring parameters.

Ring Parameters	Ring length	Ring Radius	Ring Round Trip	Measured FSR	FSR 3.4815	Er region length
RC436 WG9	12mm	0.4mm	26.5mm	0.03651nm	4.77 GHz	0.5 cm

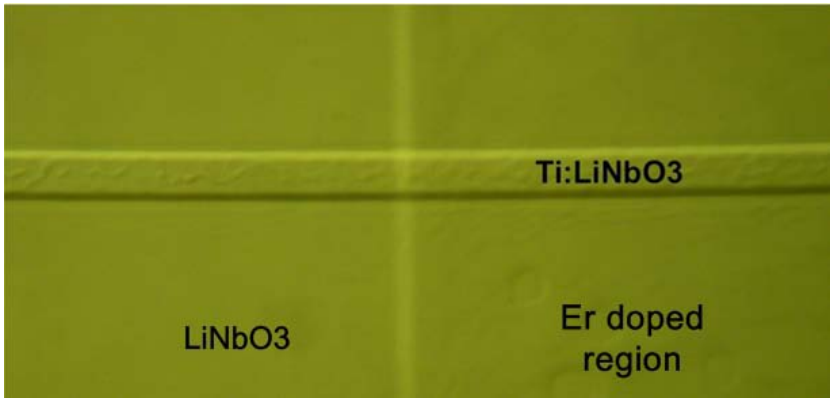

Fig. 79. Picutre of Er and Ti diffused areas.

Fabrication processes are the same as 5.1 except the Er patterning. The Er area is opened by image reversal. Then deposit 13nm Er on the sample. After deposition, lift-off was performed to remove Er in other area (Fig. 79). The Er doped area has 60nm height bump.

The detailed parameters are listed in Table XXVI. The test setup is the same as chapter 5.1. We test the sample before and after the fabrication of the As_2S_3 ring.

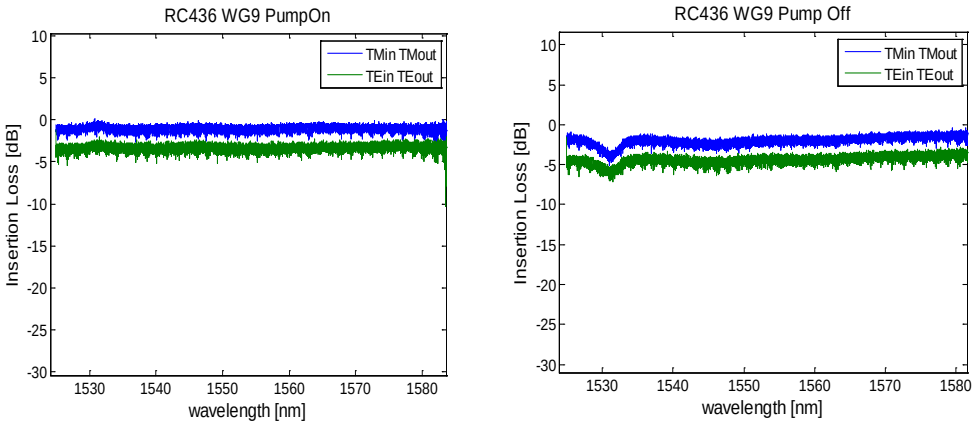

Fig. 80. Gain measurement without As_2S_3 ring.

Left: Pump on; Right: Pump off.

In Fig. 80, the left picture shows the gain curve when pump is on, the right one shows the absorption curve when pump is off. They are measured before As_2S_3 ring fabrication.

In Fig. 81, the left picture shows the gain curve when pump is on, the right one shows the absorption curve when pump is off. They are measured after As_2S_3 ring fabrication. Compare Fig. 80 and Fig. 81, the TE modes doesn't change much because it can't be coupled into the ring. But the TM modes changed a lot because they can couple into the ring and show the ring response.

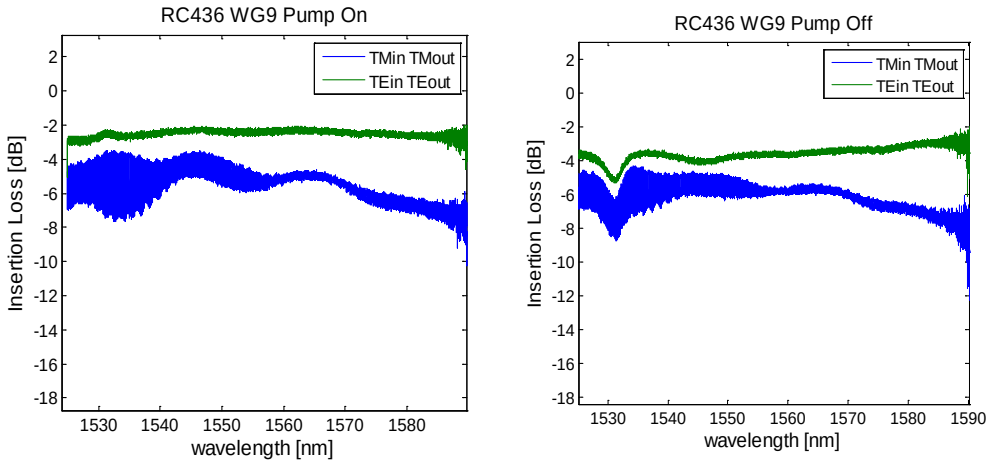

Fig. 81. Gain measurement with As_2S_3 ring.

Left: Pump on; Right: Pump off.

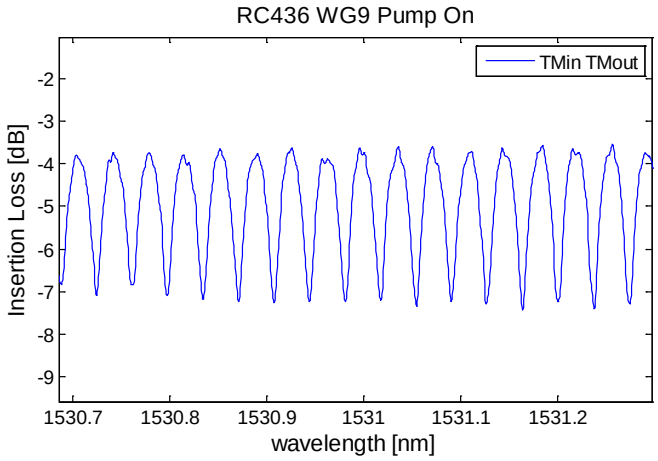

Fig. 82. Ring response (RC436, zoom in, pump on).

The zoom-in ring response is in Fig. 82. Fitted with ideal ring function, we can get the round trip loss and coulping ratio.

Table XXVII. RC 436 fitted round trip loss and coupling ratio.

RC436 WG9	Pump On		Pump Off	
Fit@1531nm	R Loss(dB)	K	R Loss(dB)	K
	12	53%	14	42%

As Table XXVII shows, the round trip loss with pump on is 12 dB, and the round trip loss with pump off is 14 dB. The round trip losses are high. The difference of the round trip losses are from the Er gain and absorption. The typical ring round trip without Er is 5-7dB, the higher loss here may come from the Er bump which ring comes across it which is shown in Fig. 79.

The results have been improved by using stepper aligner in Penny State University (PSU). The ring responses are shown in Fig. 83 when pump is on and Fig. 84 when pump is off.

Table XXVIII. RC543 ring parameters.

Ring Parameters	Ring Round Trip (cm)	Measured FSR (wavelength, nm)	FSR (frequency, GHz)	Er region length (mm)	Forward Pump (mW)	Backward Pump (mW)	SiO_2 Thickness (nm)	Q-factor ($\Delta f/f_0$@1547.9nm) Δf =0.03GHz f_0= 1.9366e14Hz
RC 543 WG6	2.65	0.03651	4.77	5	59	85	0	6.53×10^6

Ring parameters are listed in Table XXVIII. The fitted magnitude and phase responses are plotted in Fig. 85.

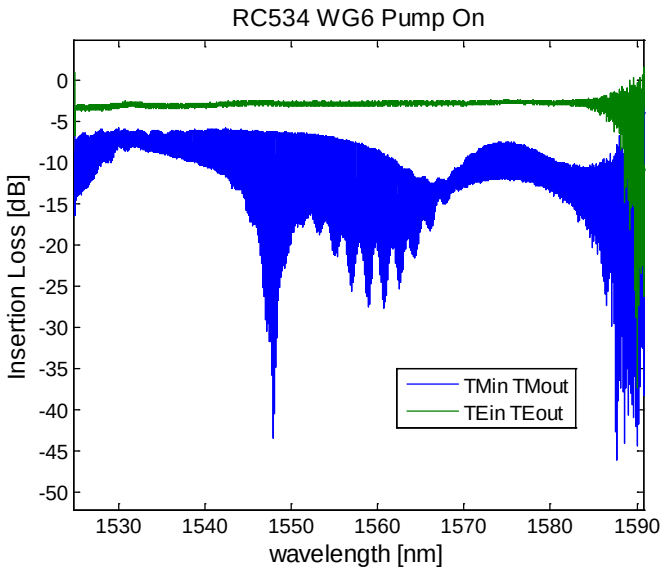

Fig. 83. Ring response when pump on (RC534, air cladding).

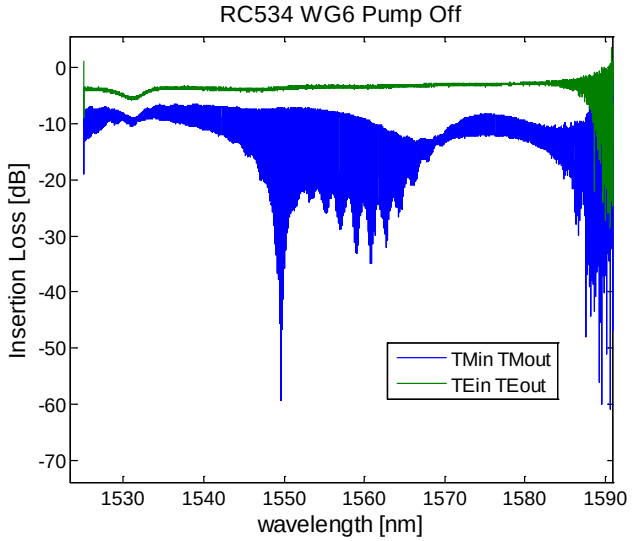

Fig. 84. Ring response when pump off (RC534, air cladding).

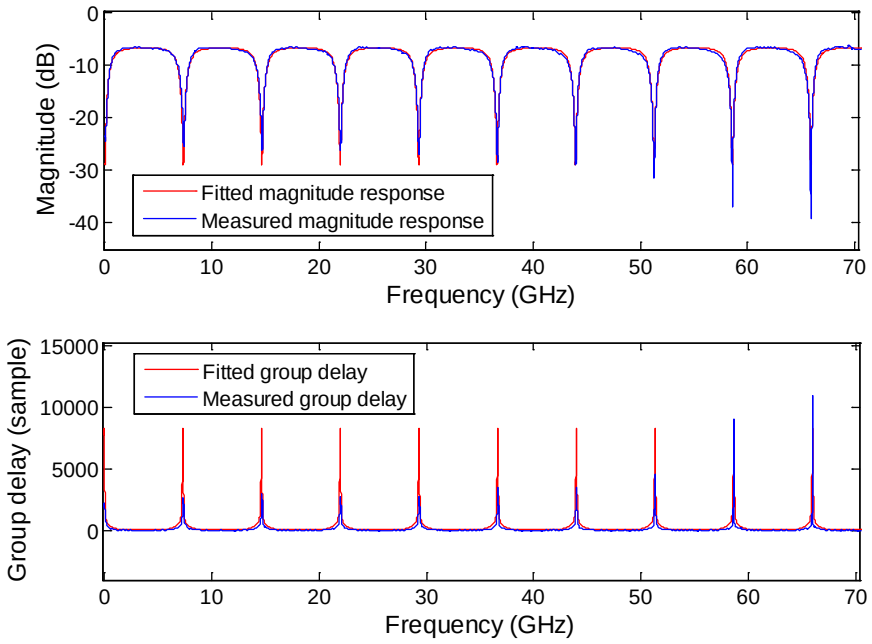

Fig. 85. Fitted magnitude and group delay (at wavelength=1547.9 nm, pump on).

Table XXIX. RC543 fitted results.

Wavelength (nm)	Pump On/Off	Round Trip Loss (dB)	Propagation Loss (dB/cm)	Coupling Ratio	Pole	Zero
1547.9	On	-4.9851	1.88	0.4398	0.5833	1.0413
	Off	-8.0475	3.04	0.4310	0.5044	0.8866
1550	On	-4.4245	1.67	0.5004	0.5666	1.1340
	Off	-5.8492	2.21	0.4861	0.5351	1.0413

The Table XXIX listed the fitted results include ring round trip loss and coupling ratio calculated by poles and zeros.

From Table XXIX, the ring round trip loss at 1550nm is 4.42dB. The Erbium bump induced loss is not as large as we thought. I will keep measuring it with different thicknesses of SiO_2 cladding to see if the ring response can shift to 1531nm.

Other observations during the measurement are list below:

(1) The Er fluorescent (green light):

In the Er region when pumped, the area at the center of the coupling region is darker (Fig. 86) than the sides even when it has only backward pump. I think it means that the pump light can also coupled into the ring.

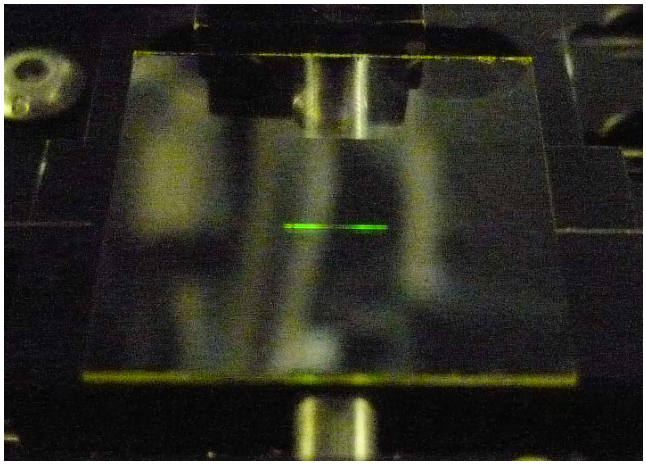

Fig. 86. Er luminescence with backward pump on: Darker in the center.

(2) Gain and absorption loss.

I can estimate the expected absorption for the length (0.5cm) and wavelength (1550nm) from some of your prior results.

From my previous results, the gain/absorption≈1:3 for every wavelength. So the gain=1/4 (RL_{pump_on}-RL_{pump_off}) and absorption=3/4 (RL_{pump_on}-RL_{pump_off}).

RT=round trip loss

For Table XXIX, the fitted ring result for air cladding, the gain at 1550nm would be:

$$\text{Gain} = \frac{1}{4}(5.8492 - 4.4245) = 0.3562\text{dB}$$

$$\text{Gain/dB} = 0.3562\text{dB}/0.5\text{cm}=0.71\text{dB/cm}$$

$$\text{Absorption} = \frac{3}{4}(5.8492 - 4.4245) = 1.068\text{dB}$$

(3).The resonance shift between pump on and off are possiblely due to the temperature drift.

I think the temperature drift will give the wavelength a tiny shift although it is very small since I measured the sample with pump on/off consecutively. It requires the temperature control it.

(4). The As_2S_3 ring has about 1μm overlap with the Ti bump which is observed by the microscope.

5.3. Er doped Ti: $LiNbO_3$ cavity

5.3.1. Multilayer measurement

Since the gain in As_2S_3 ring is hard to compensate the loss for now, another Gires Tournois structure has been carried out.

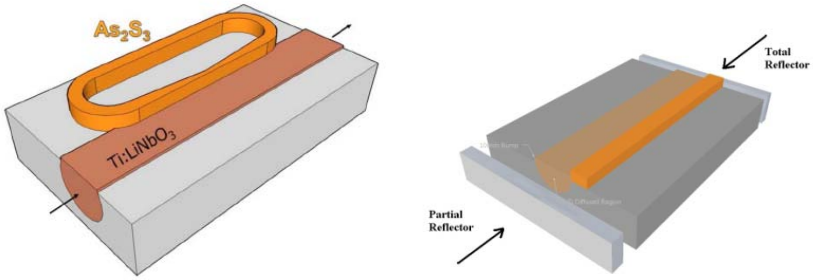

Fig. 87. Ring and GT structure.

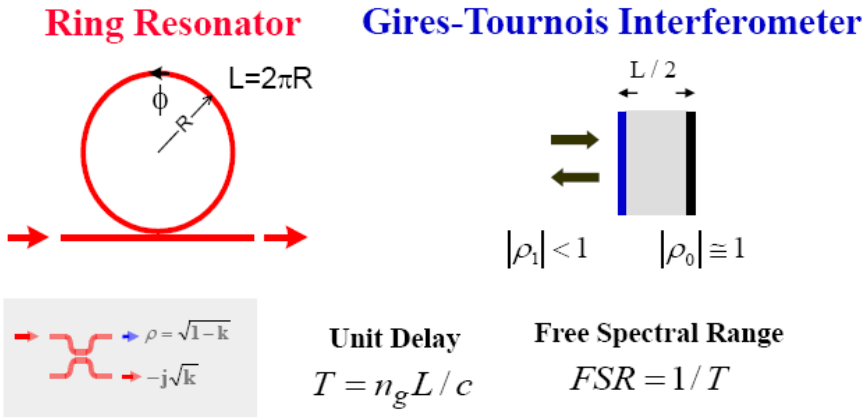

Fig. 88. Ring and GT structure comparison.

In Fig. 87 and Fig. 88, the right side is so called “Gires-Tournois” structure. It includes partial reflector on the left side and a total reflector on the right of the cavity. It has the same feedback structure the ring. The partial reflector works as the coupler to divide light to two paths. The difference is we already can get good gain the feedback loop in the cavity. So if we can make good reflectors on both side of the polished edge of the sample, we can achieve the ideal lossless feedback filter response.

To achieve this, we have to make a reflection at the edge of the samples. Measurement steps are shown in Fig. 89:

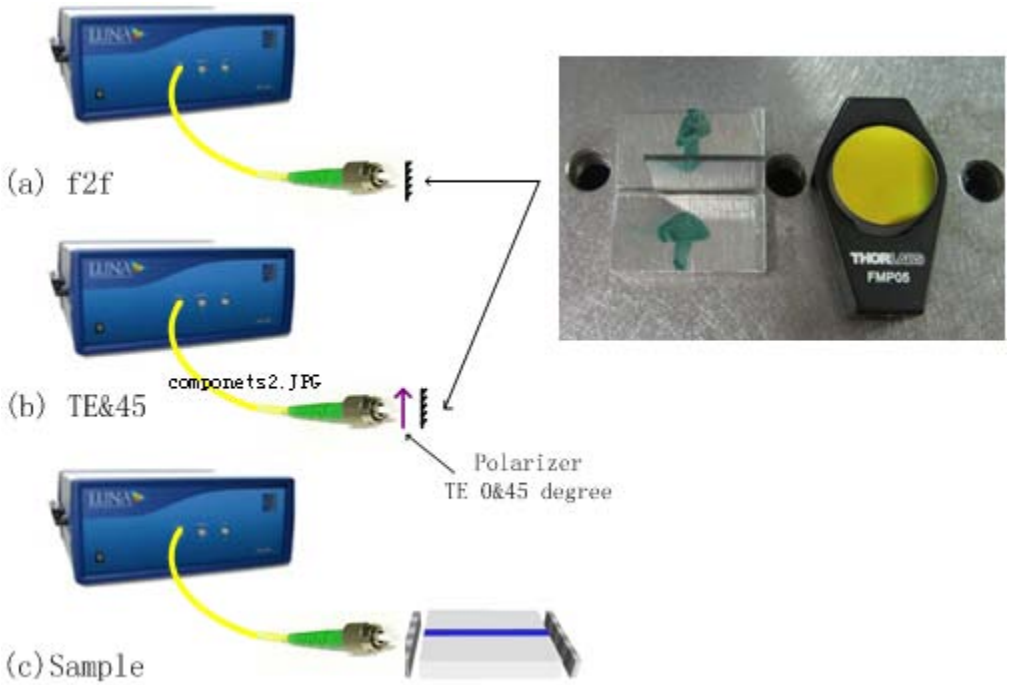

Fig. 89. Reflection measurement steps.

The reflection measurement for Multilayer cavity samples must add in a time domain filtering for the polarizer's references. Because the reflected from the first surface of the polarizer has no polarization information and it is the noise. The unfiltered references will bring in noise in the data (Fig. 90, Fig. 91 and Fig. 92)

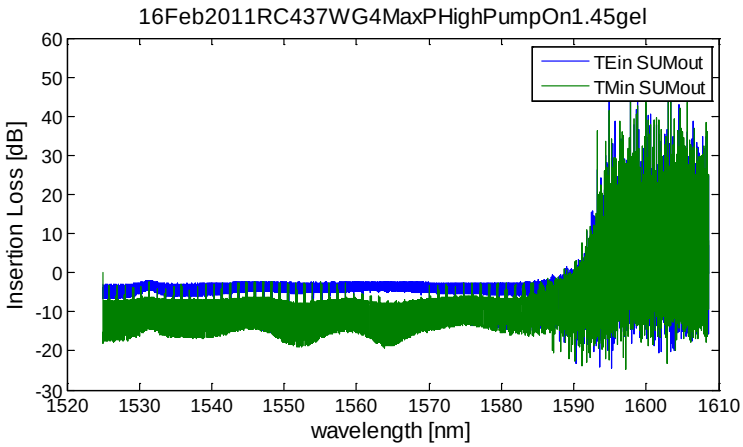

Fig. 90. TE and TM SUM out unfiltered insertion loss.

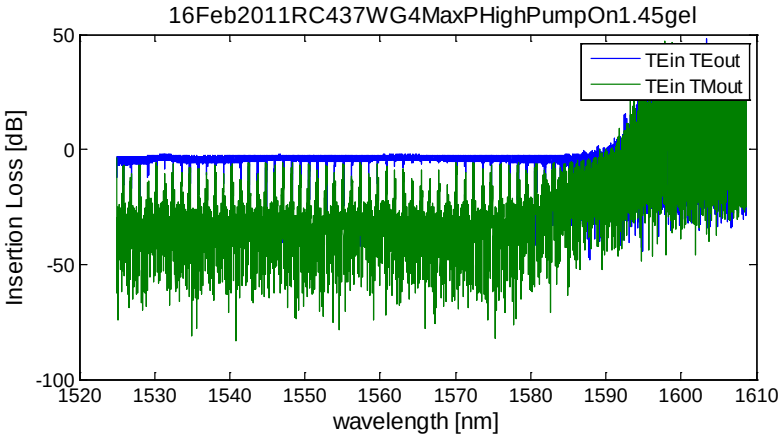

Fig. 91. TE to TE unfiltered insertion loss.

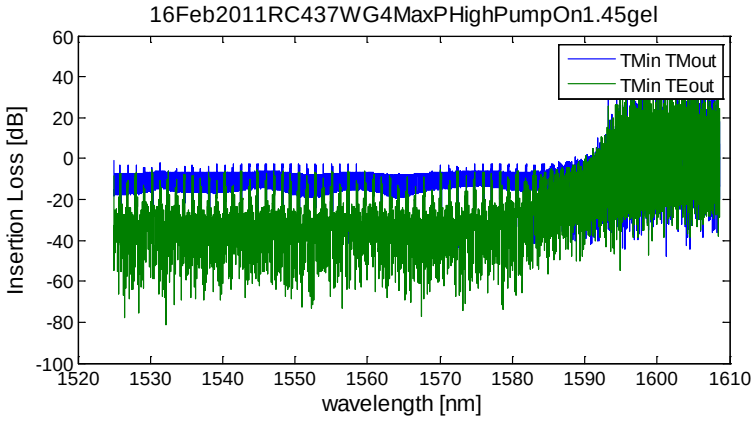

Fig. 92. TM to TM unfiltered insertion loss.

Then the polarizer's data have been filtered in time domain by matlab code (Appendix A) to remove the first peak reflected which was reflected from the first surface of the polarizer (Fig. 93). Then the filtered references without noise in the data are shown in Fig. 94, Fig. 95 and Fig. 96.

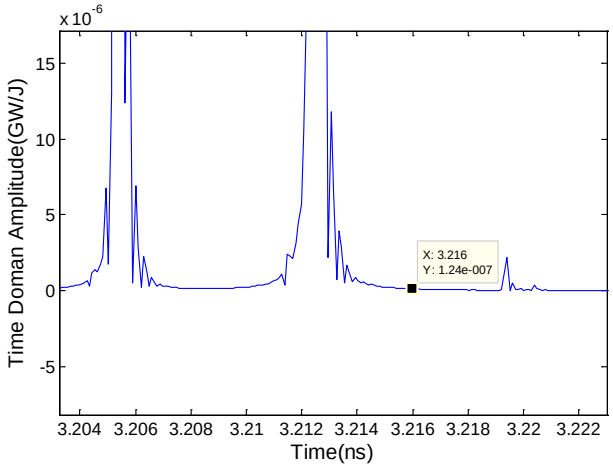

Fig. 93. Time Domain filtering.

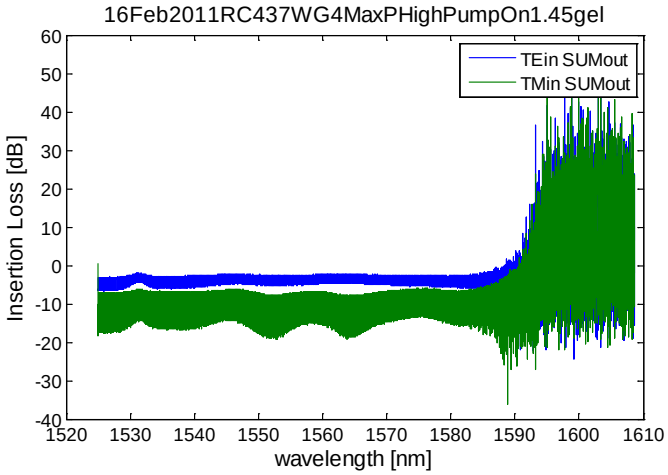

Fig. 94. TE and TM SUM out filtered insertion loss.

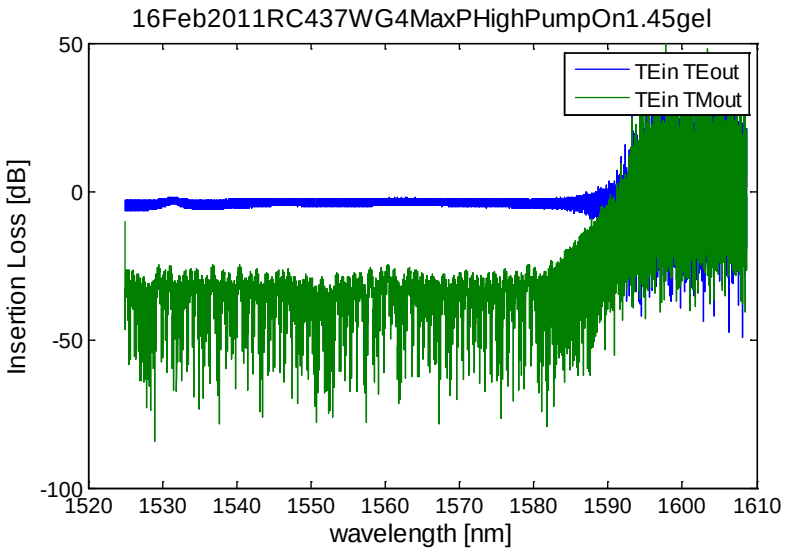

Fig. 95. TE to TE filtered insertion loss.

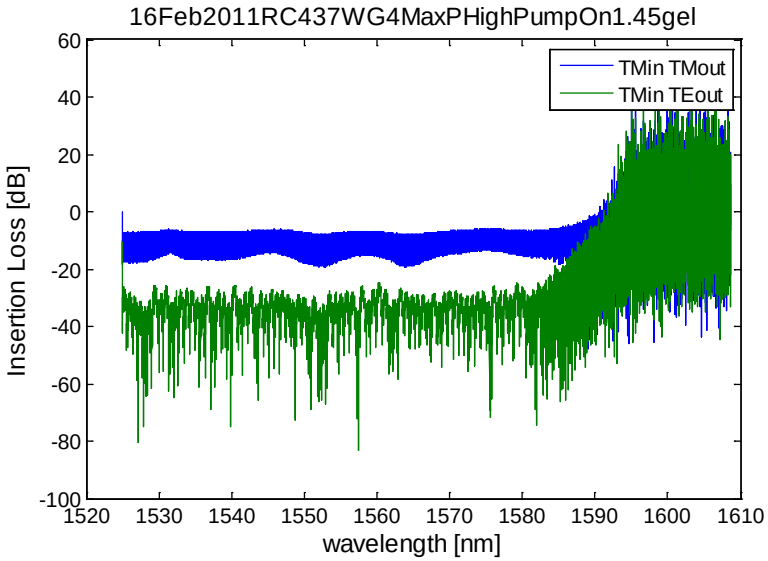

Fig. 96. TM to TM filtered insertion loss.

From the Figures above, the filtering can effectively remove the noise in the polarization references. And these references can be used to get the round trip loss.

RC283 is a planar diffused Er sample with multilayer deposited on the edge, H+L+H+L+H on the right edge, H on the left edge (H=As_2S_3, L= SiO_2, $\lambda/4$ thicknesses). It was measurement when pump on and off (Fig. 97). The pump power is 85mW. The ring responses with pump on and off are shown in Fig. 98 and Fig. 99. The fitted resonant response is fitted as shown in Fig. 100 and Table XXX.

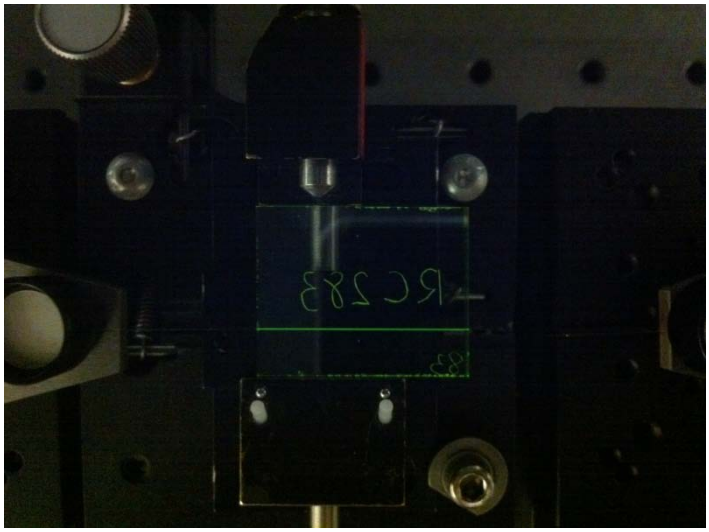

Fig. 97. Photo of RC283 at multilayer cavity measurement.

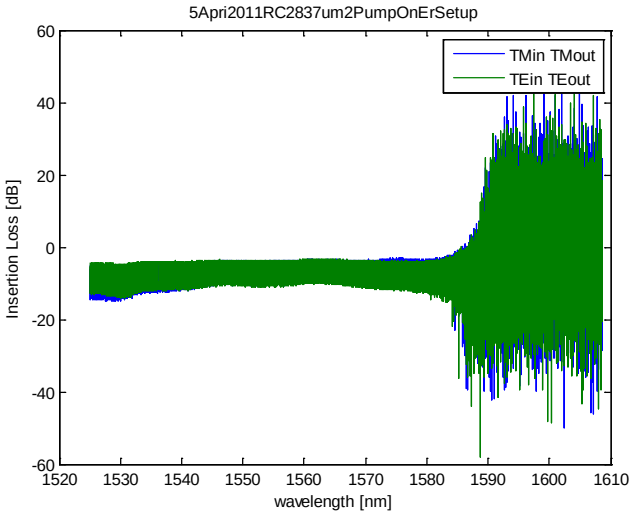

Fig. 98. RC283 multilayer result when pump on.

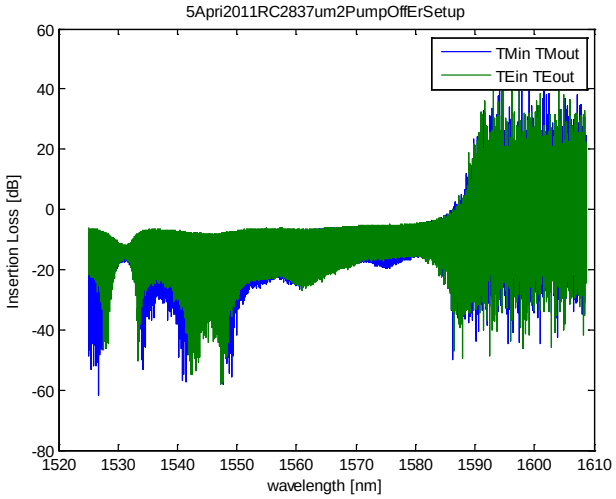

Fig. 99. RC283 multilayer result when pump off.

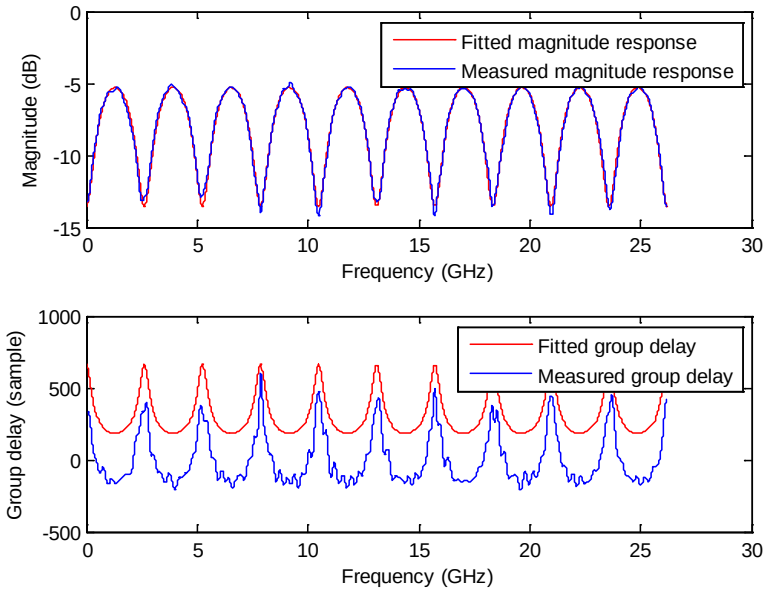

Fig. 100. Fitted Data at wavelength=1531 nm (f=1.9581e14Hz, TM, pump on).

Table XXX. RC283 cavity fitted results.

Wavelength (nm)	Pump On/Off	Round Trip Loss (dB)	Coupling Ratio	Pole	Zero
1531_TM	On	-18.0992	0.9581	0.0828	1.9771
	Off	-25.1165	0.9877	0.0316	2.5707

5.3.2. E-beam lithography results

SEM photoes are listed below from positive resist sample and negative resist sample. The single pattern is 344 μm long (0.344 μm X 1000 periods). The width is 3.5 μm at the widest part and 2.7 μm at the narrowest part on the mask.

(a) Positive resist: ZEP 520A

The SEM photos of ZEP 520A photo resist are Fig. 101, Fig. 102, Fig. 103 and Fig. 104.

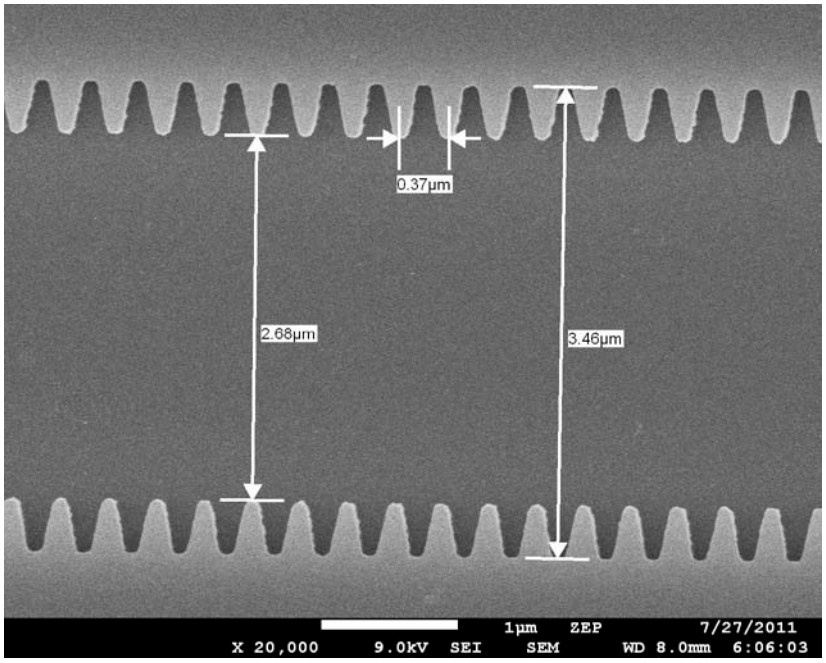

Fig. 101. SEM photo: ZEP, dose 99 μC/cm^2, lower amplification.

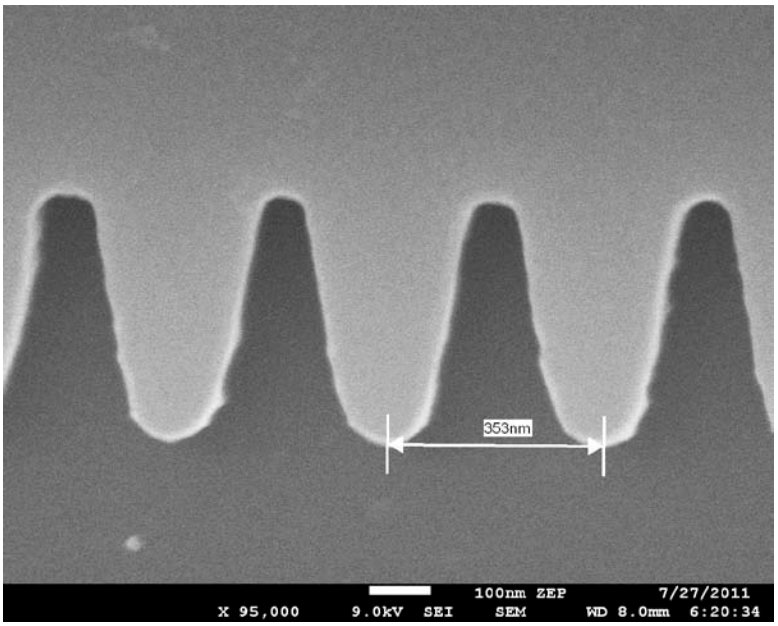

Fig. 102. SEM photo: ZEP, dose 81μC/cm^2.

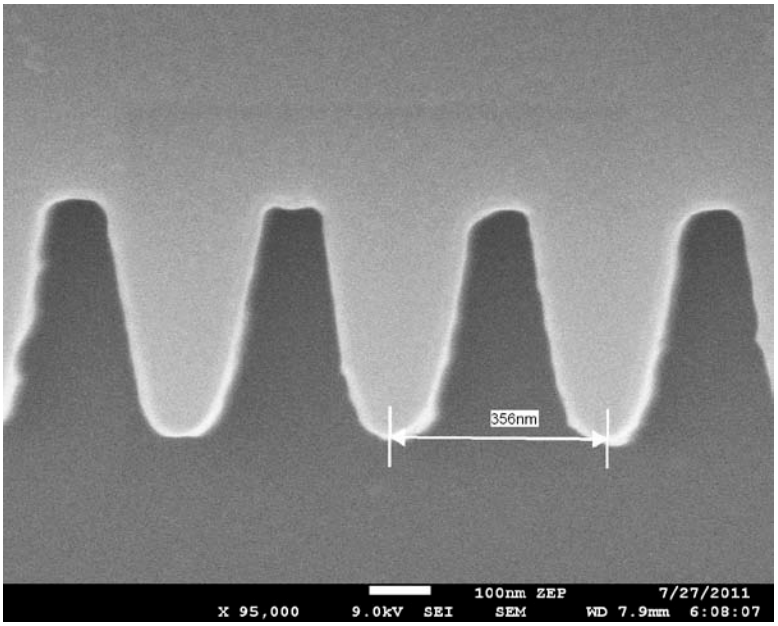

Fig. 103. SEM photo: ZEP, dose 99 μC/cm^2.

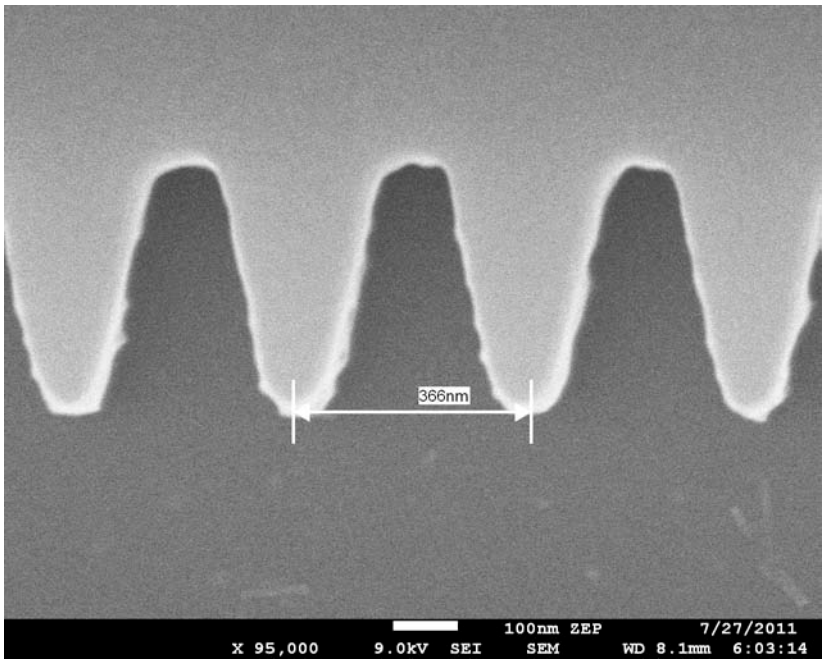

Fig. 104. SEM photo: ZEP, dose 117 μC/cm^2.

Compare Fig. 102~Fig. 104, the dose 117 μC/cm^2 has the best shape: the etched and remained teeth have the same width: 50% to 50%, duty Cycle=0.5.

(b) Negative resist: NEB 31A3

The SEM photos of NEB 31A3 photo resist are Fig. 105, Fig. 106, Fig. 107 and Fig. 108.

For NEB (negative resist) photos (Fig. 106~Fig. 108), all of them have blurred edges. These could be the thinner edges which are over etched. It may come from the under exposure. To conclude, dose 14 μC/cm^2 has the best pattern.

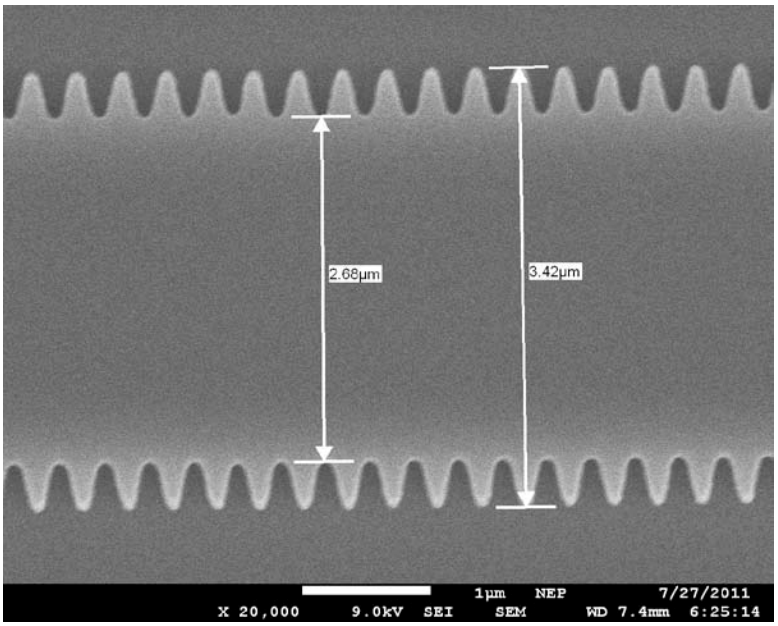

Fig. 105. SEM photo: NEB, dose 14 µC/cm^2, lower amplification.

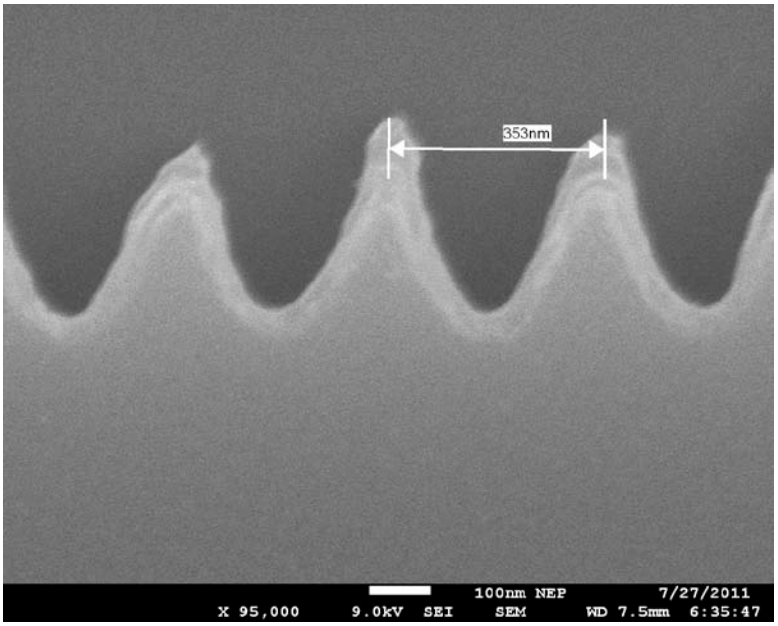

Fig. 106. SEM photo: NEB, dose 10 µC/cm^2.

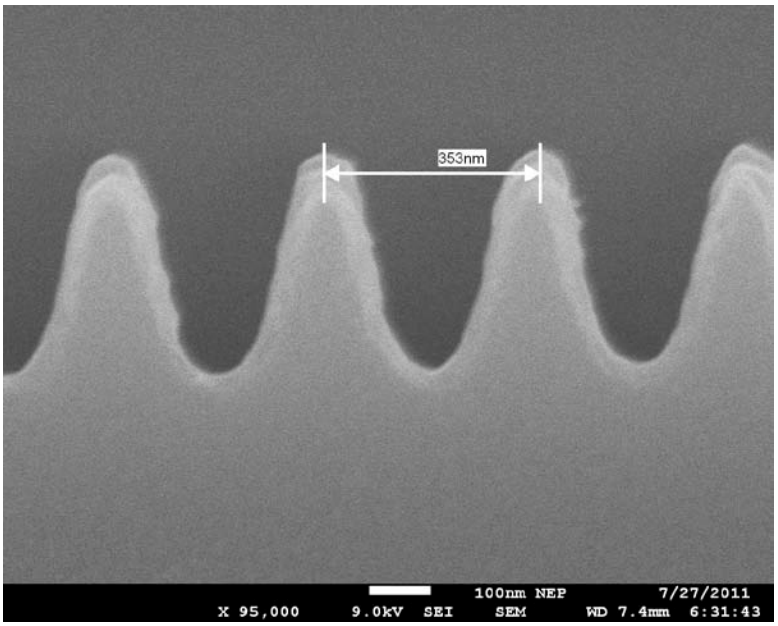

Fig. 107. SEM photo: NEB, dose 12μC/cm^2.

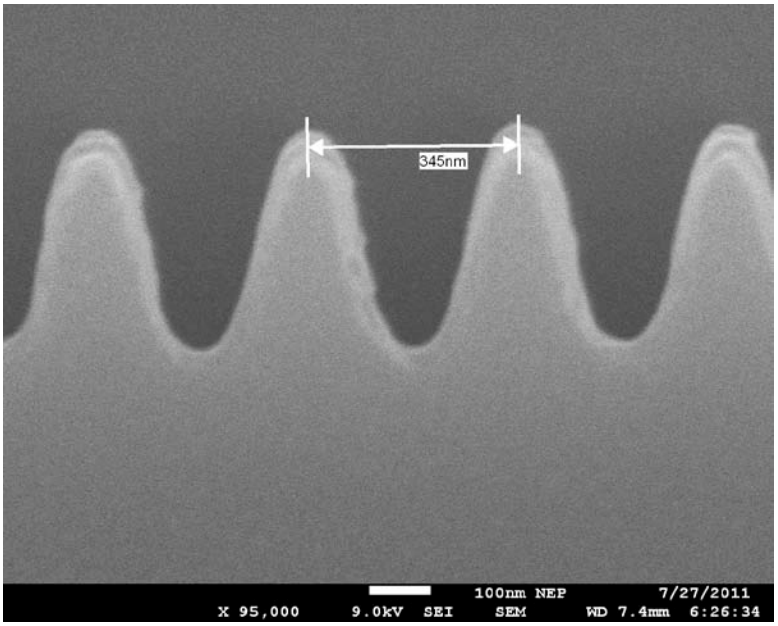

Fig. 108. SEM photo: NEB, dose 14μC/cm^2.

CHAPTER VI

CONCLUSION

To conclude, hybrid integrated waveguide devices have been simulated, analyzed and fabricated for the gain improvement through their propagation paths. The combination of the As_2S_3 waveguides and Er doped Ti:$LiNbO_3$ waveguides have been detailed studied.

We analyzed the gain improvement for various straight overlay geometries by relating the optical mode and Er overlap to the optical propagation gain. The optimal overlay thickness was found and confirmed by experiment. The propagation gain improved from 1.1 to 2 dB/cm at 1531 nm for the TM mode. This approach is compatible with vertical integration of high-index waveguides, with application to ring resonator-based filters where the roundtrip losses may be compensated with gain.

As second hybrid device, an As_2S_3 racetrack ring resonator on top of an x-cut y-propagation Er:Ti:$LiNbO_3$ waveguide has been designed and fabricated. The ring was side-coupled with the Ti:$LiNbO_3$ waveguide and the optical gain was achieved 0.72dB/cm when the Er doped coupling region was pumped by 144mW pump laser. The free spectral range (FSR) of the measured ring response for TM mode is 0.0587nm (7.33GHz) at 1550nm. The roundtrip loss are 4.4dB when pump on and 5.8dB when pump off.

The Er doped cavity has also been studied. The back mirror was fabricated by multilayer dielectric films consists of three As_2S_3 layers and two SiO_2 layers, with

reflectivity 82% at 1531m by simulation. The front partial reflector was designed to be a double-side Bragg grating using As_2S_3. The period was designed at 344 nm to make the central frequency of the reflection spectrum is at 1531nm. The fabrication of As2S3 grating was achieved by E-beam lithography due to its tiny structures. The align mark design and mask making which allows the alignment between As_2S_3 gratings and Ti diffused waveguides have been finished and the samples' testing results are coming out soon.

REFERENCES

[1] C. K. Madsen and G. Lenz, "Optical all-pass filters for phase response design with applications for dispersion compensation," *IEEE Photon. Technol. Lett.*, vol. 10, pp. 994-996, 1998.

[2] G. Lenz and C. K. Madsen, "General optical all-pass filter structures for dispersion control in wdm systems," *J. Lightwave Technol.*, vol. 17, pp. 1248-1254, 1999.

[3] C. K. Madsen, G. Lenz, A. J. Bruce, M. A. Cappuzzo, L. T. Gomez, and R. E. Scotti, "Integrated all-pass filters for tunable dispersion and dispersion slope compensation," *IEEE Photon. Technol. Lett.*, vol. 11, pp. 1623-1625, 1999.

[4] C. K. Madsen, J. A. Walker, J. E. Ford, K. W. Goossen, T. N. Nielsen, and G. Lenz, "A tunable dispersion compensating mems all-pass filter," *IEEE Photon. Technol. Lett.*, vol. 12, pp. 651-653, 2000.

[5] C. K. Madsen, "Subband all-pass filter architectures with applications to dispersion and dispersion-slope compensation and continuously variable delay lines," *J. Lightwave Technol.*, vol. 21, pp. 2412-2420, 2003.

[6] G. Lenz, B. J. Eggleton, C. K. Madsen, and R. E. Slusher, "Optical delay lines based on optical filters," *IEEE J. Quantum Electron.*, vol. 37, pp. 525-532, 2001.

[7] V. Ta'eed, N. J. Baker, L. Fu, K. Finsterbusch, and M. R. E. Lamont, "Ultrafast all-optical chalcogenide glass photonic circuits," *Opt. Exp.*, pp. 9205-9221, 2007.

[8] Wikipedia. "As2s3," In *Wikipedia*. Available: http://en.wikipedia.org/wiki/As2S3, Accessed in Sept., 2011.

[9] Wikipedia. "Linbo3," In *Wikipedia*. Available: http://en.wikipedia.org/wiki/LiNbO3, Accessed in Sept., 2011.

[10] M.N.Armenise, "Fabrication techniques of lithium niobate waveguides," *Optoelectronics, IEE Proceedings J* vol. 135, pp. 85-91, 1988.

[11] W.K.Burns, P.H.Klein, and E.J.West, "Ti diffusion in ti:Linbo3 planar and channel optical waveguides," *J.Appl. Phys.*, vol. 50, pp. 6175 - 6182 1979.

[12] Wikipedia. "Erbium," In *Wikipedia*. Available: http://en.wikipedia.org/wiki/Erbium, Accessed in Sept., 2011.

[13] R. Brinkmann, I. Baumann, M. Dinand, W. Sohler, and H. Suche, "Erbium-doped single and double pass ti:Linbo3 waveguide amplifiers," *IEEE J. Quantum Electron.,* vol. 30, pp. 2356-2360, 1994.

[14] P. Becker, R. Brinkmann, M. Dinand, W. Sohler, and H. Suche, "Er diffused ti:Linbo3 waveguide laser of 1563 and 1576 nm emission wavelengths," *Appl. Phys. Lett.,* vol. 61, pp. 1257-1259, 1992.

[15] M. Dinand and W. Sohler, "Theoretical modeling of optical amplification in er-doped ti:Linbo3 waveguides," *IEEE J. Quantum Electron.,* vol. 30, pp. 1267-1276, 1994.

[16] W. Sohler, B. Das, D. Dey, S. Reza, H. Suche, and R. Ricken, "Erbium-doped lithium niobate waveguide lasers," *IEICE Transactions Electron E,* vol. 88-C, pp. 990-997, 2005.

[17] K. Kishioka, T. Kishimoto, and K. Kume, "Improvement of the optical gain in the er-doped lithium niobate waveguide optical amplifiers," *IEICE TRANS. ELECTRON.,* vol. 88-C, pp. 1041-1052, 2005.

[18] M. E. Solmaz, D. B. Adams, W. C. Tan, W. T. Snider, and C. K. Madsen, "Vertically integrated as2s3 ring resonator on linbo3," *IEEE Opt. Lett.,* vol. 34, pp. 1735-1737, 2009.

[19] Y. Zhou, X. Xia, W. T. Snider, J. H. Kim, Q. Chen, W. C. Tan, and C. K. Madsen, "Two-stage taper enhanced ultra-high q -as2s3 ring resonator on linbo3," *IEEE Photonic Technol.,* vol. 23, pp. 1195-1197, 2011.

[20] Q. Xu, B. Schmidt, S. Pradhan, and M. Lipson, "Micrometer-scale silicon electro-optic modulator," *Nature,* vol. 435, pp. 325-327, 2005.

[21] B. E. Little, J. S. Foresi, G. Steinmeyer, E. R. Thoen, S. T. Chu, H. A. Haus, E. P. Ippen, L. C. Kimerling, and W. Greene, "Ultra-compact si–sio microring resonator optical channel dropping filters," *IEEE Photon. Technol. Lett.,* vol. 10, pp. 549-551, 1998.

[22] P. A. Regalia, S.K.Mitra, and P.P.Vaidyanathan, "The digital all-pass filter: A versatile signal processing building block," *Proceedings of the IEEE* vol. 76, pp. 19-37, 1988.

[23] B. E. Little, S. T. Chu, H. A. Haus, J. Foresi, and J.-P. Laine, "Microring resonator channel dropping filters," *J. Lightwave Technol.,* vol. 15, pp. 998-1005, 1997.

[24] M. Jablonski, Y. Takushima, K. Kikuchi, Y. Tanaka, K. Furuki, K. Sato, and N. Higashi, "Layered optical thin-film allpass dispersion equaliser for compensation of dispersion slope of optical fibres," *Electron. Lett.,* vol. 36, pp. 1139-1141, 2000.

[25] F. Melia, *Electrodynamics,* 1st ed. Chicago: The University of Chicago Press, 2001.

[26] A. S. Sudbo, "Improved formulation of the film mode matching method for mode field calculations in dielectric waveguides," *Pure Appl. Opt.,* vol. 381-388, 1994.

[27] C. Vassallo and J. M. v. d. Keur, "Comparison of a few transparent boundary conditions for finite-difference optical mode-solvers," *Journal of Lightwave Technology,* vol. 15, pp. 397-402, 1997.

[28] Strake, G. P. Bava, and I. Montrosset, "Guided modes of ti: Linbo3 channel waveguides. A novel quasi-analytical technique in comparison with the scalar finite-element method channel," *J. Lightwave T.,* vol. 6, pp. 1126-1135, 1998.

[29] M. V. Hobden and J. Warner, "The temperature dependence of the refractive indices of pure lithium niobate," *Phys. Lett.,* vol. 22, pp. 243- 244, 1966.

[30] G. J. EDWARDS and M. LAWRENCE, "A temperature-dependent dispersion equation for congruently grown lithium niobate," *Optical and Quantum Electronics,* vol. 16, pp. 373-375, 1984.

[31] D. H. Jundt, "Temperature-dependent sellmeier equation for the index of refraction, ne, in congruent lithium niobate," *OPTICS Lett.,* vol. 22, pp. 1553-1555, 1997.

[32] V. V. Atuchin, T. I. Grigorieva, I. E. Kalabin, V. G. Kesler, L. D. Pokrovsky, and D. I. Shevtsov, "Comparative analysis of electronic structure of ti: Linbo3 and linbo3 surfaces," *Journal of Crystal Growth,* vol. 275, pp. e1603-e1607, 2004.

[33] F. Caccavale, F. Segato, Mansour, I. Mansour, J. M. Almeida, and A. P. Leite, "Secondary ion mass spectrometry study of erbium diffusion in lithium niobate crystals," *Journal of Materials Research,* vol. 13, pp. 1672-1678, 1998.

[34] S. A. Campbell, *The Science and Engineering of Microelectronic Fabrication*, 2nd ed. New York: Oxford University Press, 2001.

[35] F. Caccavale, F. Segato, I. Mansour, J. M. Almeida, and A. P. Leite, "Secondary ion mass spectrometry study of erbium diffusion in lithium niobate crystals," *J. Mater. Res.,* vol. 13, pp. 1672-1678, 1998.

[36] A. A. M. Saleh, R. M. Jopson, and J. D. E. a. J. Aspell, "Modeling of gain in erbium-doped fiber amplifiers," *IEEE Photonic Technol. Lett.,* vol. 2, pp. 714-717, 1990.

[37] Y. Sun, J. L. Zyskind, and A. K. Srivastava, "Average inversion level, modeling, and physics of erbium-doped fiber amplifiers," *IEEE J. Sel. Top. Quantum Electron.* , vol. 3, pp. 991-1006, 1997.

[38] H. A.Macleod, *Thin-film Optical Filters*, 4th ed. Boca Raton, FL: CRC Press/Taylor & Francis, 2010.

[39] K. O. Hill, Y. Fujii, D. C. Johnson, and B. S. Kawasaki, "Photosensitivity in optical fiber waveguides: Application to reflection filter fabrication," *Appl. Phys. Lett.,* vol. 32, pp. 647-649, 1978.

[40] B. S. Kawasaki, K. O. Hill, D. C. Johnson, and Y. Fujii, "Narrow-band bragg reflectors in optical fibers," *Opt. Lett.,* vol. 3, pp. 66-68, 1978.

[41] H. Kogelnick, "Filter response of nonuniform almost-periodic gratings," *Bell Syst. Tech. J.,* vol. 55, pp. 109-126, 1976.

[42] L. A. Weller-Brophy and D. G. Hall, "Analysis of waveguide gratings: Application of rouard's method," *J. Opt. Soc. Amer. A,* vol. 2, pp. 863-871, 1985.

[43] M. Yamada and K. Sakuda, "Analysis of almost-periodic distributed feedback slab waveguides via a fundamental matrix approach," *Appl. Opt.,* vol. 26, pp. 3474-3478, 1987.

[44] V. Mizrahi and J. E. Sipe, "Optical properties of photosensitive fiber phase gratings," *J. Lightwave Technol.*, vol. 11, pp. 1513-1517, 1993.

[45] A.Yariv, "Coupled-mode theory for guided-wave optics," *IEEE J. Quantum Electron.*, vol. 9, pp. 919-933, 1973.

[46] R. Salas-Montiel, M. E. Solmaz, W. C. Tan, X. Song, W. T. Snider, and C. K. Madsen, "Selective co-doped erbium ti:Linbo3 waveguide amplifiers," *Proc. SPIE* vol. 7605, pp. 76050L-1～76050L-8, 2010.

[47] X. Song, W. Tan, W. T. Snider, X. Xia, and C. K. Madsen, "Gain improvement of er-ti:Linbo3 waveguide amplifier by an as2s3 overlay waveguide," *IEEE Photon. J.*, vol. 3, pp. 686-695, 2011.

[48] X. Xia, Y. Zhou, and C. K. Madsen, "Analysis of as2s3-ti: Linbo3 taper couplers using supermode theory," *J. of Lightwave Technol.*, 2011.

[49] J. Chen and C. Cox, "High efficient silicon-on-lithium niobate modulator," USA Patent US 2009/0067771 A1, 2009.

[50] R.-H. Kim, J. Zhang, O. Eknoyan, H. F. Taylor, and T. L. Smith, "Narrowband bragg reflectors in ti:Linbo3 optical waveguides," *Appl. Lett.*, vol. 45, pp. 4927-4932, 2006.

APPENDIX A

MATLAB CODES FOR TITANIUM DIFFUSION PARAMETER CALCULATION AND TIME DOMAIN FILTERING

Matlab code for titanium diffusion parameter calculation:

```
%% delta RIN (Refractive Index change)
clear;
%%%% Input parameters: %%%%%%%%%%%%
t_h=9.5;     % diffusion time by hours
tal=0.095;   % Ti strip thickness: um->cm%

w=7;         % Ti strip(waveguide) width: um
T=1298.15;   % diffusion temperature=1025 degree
lamda=1.55;  % um
%%%%% End of Input parameters %%%%%

%%%%%%% Constants %%%%%%%%%%%%%%%
T0=30300;
t=t_h*3600;

DoV_cm=0.0199; %% Diffusivity: cm^2/s => m^2/s %%
DoH_cm=0.0289;
DoV=DoV_cm*1e-4;
DoH=DoH_cm*1e-4;

do=0.67*lamda^2/(lamda^2-0.13);
de=0.839*lamda^2/(lamda^2-0.0645);
Fo=1.3e-25; %% Fo,Fe: cm^3
Fe=1.2e-23;
gmo=0.55;
gme=1;
%%%% End of Constants %%%%%%%%%%
%%%%%Diffusion Length: um %%%%%%
Dh=2*sqrt(t*DoH*exp(-T0/T))*1e6
Dv=2*sqrt(t*DoV*exp(-T0/T))*1e6

%%%%%%%%% Delta RIN  %%%%%%%%%%%
Cm=5.67e22;   % cm^-3
c0=tal*Cm/(sqrt(pi)*Dv);
c=c0*2*erf(w/2/Dh);
```

```
delneXX=de*(Fe*c)^gme*1.7
delnoYY=do*(Fo*c)^gmo*1.49
delnoZZ=delnoYY
```

Matlab code for Time domain filtering:

```
%Input filter function to filter Jpol
plot(time,abs(Jpol(1,:)).^2+abs(Jpol(2,:)).^2+abs(Jpol(3,:)).^2+abs(Jpol(4,:)).^2);
temp=input('pick two points and press enter');
n1=p1.DataIndex;
n2=p2.DataIndex;
%filter window:
window1_1=zeros(1,n1);
window1_2=ones(1,n2-n1);
window1_3=zeros(1,m+1-n2);
window1={window1_1 window1_2 window1_3};
window1=cell2mat(window1);
for n=1:4
 Jpol(n,:)=Jpol(n,:).*window1;
end
```

APPENDIX B

OPTI-SYSTEM PARAMETERS

The EDWA parameters are listed below:

Table A-1 EDWA parameters setting

Name	Value	Units	Mode
Waveguide Length	0.035	m	Normal
Signal background loss	40	dB/m	Normal
Pump background loss	15	dB/m	Normal
Refractive index data file	950A Ti,9 hrs diffusion		Normal
Er ion density distribution	Er Profile which has Deff=6um		Normal
Wavelength to calculate the mode	1531	nm	Normal
Polarization for signal mode calculation	TE or TM		Normal
Number of modes at pump wavelength	1		Normal
Polarization for pump mode calculation	TE or TM		Normal
Power ratio for each pump mode	1		Normal
Er ion density	100e24	m^-3	Normal
Er metastable life time	2.4	ms	Normal
Er signal excess loss	0	dB/m	Normal
Er pump excess loss	0	dB/m	Normal
Yb ion density	1e0	m^-3	Normal

Table A-1 Continued

ESA cross section value at	55e-027	m^2	Normal
Number of ASE modes	2		Normal
A32	1e9	1/s	Normal
A43	1e9	1/s	Normal
Fraction of ion in pair	0		Normal
Fast nonradiative upconverion lifetime	5e-6	s	Normal
Calculate upconversion effects	No		Normal
Cup	10e-24	m^3/s	Normal
C3	100e-24	m^3/s	Normal
C14	70e-24	m^3/s	Normal
C16	70e-24	m^3/s	Normal
Relative error	0.5e-6		Normal
Longitudinal steps	130		Normal
Calculate graphs	Yes		Normal
Longitudinal power garph	Yes		Normal
Normalized population density	Yes		Normal
Simulation Enabled	Yes		Normal
Noise center frequency	193.4	THZ	Normal
Noise bandwidth	13	THz	Normal
Noise bins spacing	125	GHz	Normal
Noise threshold	-100	dB	Normal
Noise dynamic	3	dB	Normal
Convert noise bins			Normal
Generate random seed	Yes		Normal
Random seed index			Normal

VITA

Xiaomin Song was born in Hefei, China in 1980. He received his Bachelor of Science degree in electrical engineering from Tsinghua University, Beijing, China in 2003 and Master of Science degree in electrical engineering from Tsinghua University, Beijing, China in 2006. He received his Ph.D. degree in electrical and computer engineering from Texas A&M University in 2011. His research interest involves integrated optical filter and amplifier design and fabrication.

Dr. Song may be reached at Texas A&M University, Electrical and Computer Engineering Department, College Station, TX, 77843-3128. His email is songxm99@neo.tamu.edu.